We are IntechOpen,
the world's leading publisher of
Open Access books
Built by scientists, for scientists

6,300
Open access books available

171,000
International authors and editors

190M
Downloads

154
Countries delivered to

Our authors are among the

TOP 1%
most cited scientists

12.2%
Contributors from top 500 universities

BOOK CITATION INDEX
CLARIVATE ANALYTICS
INDEXED

WEB OF SCIENCE™

Selection of our books indexed in the Book Citation Index
in Web of Science™ Core Collection (BKCI)

Interested in publishing with us?
Contact book.department@intechopen.com

Chapter

Introductory Chapter: Large Eddy Simulation for Turbulence Modeling

Aamir Shahzad, Muhammad Kashif and Fazeelat Hanif

1. Introduction

Laminar and non-laminar are two major types of flows and are discussed mainly in fluid mechanics. Streamline and turbulent flows are examples of laminar and non-laminar flows; however, a laminar flow can be transformed into non-laminar by applying some kind of perturbations (such as temperature, pressure, force field, etc.) and/or by employing some gradient. This type of conversion process from laminar to non-laminar flow produces new patterns in between the two states, and these patterns are unstable, and it generates the flow instabilities in the fluid. Only large eddies (large-scale motions) are directly computed in large eddy simulation (LES); therefore, to create the three-dimensional (3D) unsteady governing equations for large-scale motions, a low-pass spatial filter is used for the instantaneous conservation equations. LES has wide range of applications for compressible flows, turbulent combustion, aeroacoustics, turbulent/transitional flows, and atmospheric sciences. In comparison to LES for cases involving incompressible flows, much less work has been performed on LES for compressible flows, and there are numerous difficulties/problems in this field. Extra work/requirements are needed for supersonic flows with shock waves in order to accurately and steadily capture the shock while also providing the spatial accuracy necessary to simulate a number of fine-scale turbulence structures. Low-order techniques are typically used to address shock waves, frequently using upwind schemes that are not particularly suitable for LES. Favre filtering is typically used in compressible flows to prevent the entry of sub-grid scale (SGS) terms into the continuity equation; therefore, knowledge and expertise obtained in incompressible flows may not be applicable. SGS modeling for compressible flows is significantly more difficult as a result of the additional equations that must be solved, such as the energy equation for the compressible case, and the necessity to represent additional SGS terms, such as the SGS heat flux [1].

With applications in a variety of combustion issues, LES of turbulent combustion first emerged in the 1990s and has grown significantly in the last 10 years. The majority of combustion chemistry takes place in SGS; therefore, models must be created because chemical reactions typically take place on sizes much smaller than those of LES meshes. However, even with very straightforward SGS combustion models, LES has showed considerable potential in this field and clearly outperformed the Reynolds-averaged Navier-Stokes (RANS) approach. However, due to the complexity of turbulent combustion, which includes chemical reactions, turbulence/chemistry interactions, liquid fuel atomization, liquid fuel injection, droplet breakup and evaporation, small-scale

molecular fuel air mixing, large-scale turbulent fuel air mixing, and chemical reactions in aircraft engines, there are significant challenges in this area. Many of these processes take place at various ranges of length and time [1]. LES also has wide range of applications in gas turbine. Reduced life cycle costs for the operator and decreased environmental effect during engine production and operation are crucial factors for gas turbine manufacturers. Many gas turbine components use a stable RANS approach; however, when it comes to the rotor-stator interaction in turbomachinery, we frequently use an unsteady RANS (URANS) approach where the governing flow equations are phase averaged assuming a constant rate of rotation [2]. LES-related techniques are being used more frequently as a result of the inability of RANS models to produce accurate off-design aerodynamics forecasts, noise source information, and predictive capability for the control of drag, noise, and mixing processes in general. The huge advances in accessible computing power over the past few years have provided additional encouragement for the usage of LES [3].

1.1 LES for aeroacoustics

A major amount of the noise that is produced by air and land transportation, such as fan noise, jet noise, high-speed train noise, and airframe noise, is a growing environmental concern. Turbulence is a prominent source of aerodynamic noise. Because LES directly computes large scale fluctuations, which are known to add the most to the noise generated in many issues, LES is a very helpful technique in aeroacoustics. Applications of LES for foretelling aerodynamic noise likely began in the 1990s and have since grown to be a very active area of research. LES shows considerable promise for aeroacoustics computations, from improving source modeling for acoustic analogies to practical prediction and designing of engineering systems in the near future. It also advances fundamental understanding of noise creation. LES algorithms should be able to reliably mimic the flow physics that captures the transfer of energy from turbulent to acoustic modes if properly built and validated. The proper SGS modeling, numerical issues such as high-order accuracy and careful usage of the boundary conditions, and practical engineering configurations where flow Reynolds numbers are typically very high make it impractical to use LES for both noise source capturing and its propagation and are all still significant challenges. Additionally, standard validation study against approved experimental databases can be carried out for relatively basic LES applications. Since intricate statistics such as two-point space-time correlations are essential to flow-generated sound, more attention should be given while validating LES applications in aeroacoustics, according to the theory. As a result, the validation may begin with the most basic facts before moving on to more intricate and acoustically important statistics [1].

1.2 LES for turbulent/transitional flows

Turbulence has an important property, which is scale invariance. Certain characteristics of the flow are said to be scale invariant if they hold true across various motion scales. Such symmetry can be explained as an especially straightforward relation between small and large scales, making it a crucial component in turbulence models [4]. LES, a different strategy, was first suggested by Smagorinsky in 1963. The traditional RANS approach, which requires solving additional modeled transport equations to determine the so-called Reynolds stresses as a result of the averaging procedure, is not used by LES. When compared with direct numerical simulation (DNS), the computational cost of LES is significantly lower since only small-scale SGS

motions are represented and the large-scale motions of turbulent flow are computed directly. LES is more perfect than the RANS approach as the large eddies contain most of the turbulent energy and are accountable for most of the turbulent mixing and momentum transfer, and these eddies are captured directly by LES in full detail where they are modeled in the RANS approach. Moreover, the small scales tend to be more homogeneous and isotropic than the large ones, and thus, the SGS motions modeling should be easier than all scales modeling within a single model such as in the RANS approach [1]. There are two main types of SGS models for LES of turbulent flows. The models that yield expressions for SGS terminology such as a heat flux or stress tensor and typically include eddy viscosity notions fall under one group. The SGS stresses are secondary values, which are directly computed from the definitions in the other category, which describes the unresolved primitive variables such as velocity or temperature [5]. For most meteorological applications, large eddies, which hold the majority of the turbulent kinetic energy (TKE) also referred as energy-containing eddies, are the most significant scales for atmospheric planetary boundary layer (PBL) turbulence, as an example, and are in charge of most turbulent transport concerned. It is a simulation that specifically determines (or eliminates) large eddies when LES roughly reflects the effects of smaller ones. As LES's grid resolution increases, less are present, a greater spectrum of turbulent eddies is resolved, and LES-generated flows are parameterized, and they become more representative throughout the flow field. Thus, now LES is the most promising/feasible numerical mean for realistic turbulent/ transitional flows simulation [6]. LES inlet conditions were also generated on the basis of implementation of digital filter generator (DFG). The test case was the LES of a channel flow with a continuously repeated constriction. The DFG was used to construct three-time series that would be used as LES inlet conditions in the future. Along with entering the first and second moments of the velocity field over the inlet plane from the periodic boundary condition (PBC) simulation in the first, the DFG's input turbulence scales were set to be spatially homogeneous with values determined using a channel inlet height-weighted area average. The turbulence scales were allowed to change in the second and third time series. Their variation is again inferred from the PBC simulation and is related to wall normal direction. Then, LES's inlet boundary conditions were created using these distinct time series. These changing turbulent scales have increased the simulation accuracy, which has significant uses [7].

1.3 LES for atmospheric science

Prior LES research mostly concentrated on a turbulent PBL with flat terrain and no clouds. Due to the enormous thermal plumes present and the lack of other flow conditions, this flow regime is best suited to LES without involving complex physical phenomena (such as latent heating and radiation). However, in recent years, LES has been broadened to study more challenging and complicated PBL regimes, which are pertinent to forecasts for severe weather and climate, or more recent applications for wind energy [6].

2. History, current state, and future challenges of LES

2.1 History

Smagorinsky first proposed LES in 1963 for forecasting air flow, and early uses likewise fell under this category. Deardoff and Schumann introduced LES to

engineering-related flow for the first time in 1970 and 1975, respectively. From the 1960s to roughly the middle of the 1980s, LES took a while to develop, and the applications primarily consisted of straightforward, building-block flows, such as homogeneous turbulence, plane channel flows, mixing layers, and so on. However, as computing power increased, a very fast development and sharp increase in LES applications began around the middle of the 1980s, particularly after the 1990s with substantial growth of the LES community and a wide range of LES applications shifting from simple flows to complex flows, including multi-phase flow, heat transfer, and fluid dynamics, aeroacoustics, transmission, combustion, etc. In addition to the rise in computing power, it is now evident that RANS approaches naturally have limitations and can't deal with certain categories of sophisticated turbulent flow issues, and LES has developed quickly and has a wide range of applications [1].

2.2 Current state

As was indicated in the preceding section, the LES was initially applied successfully to examine the specifics of flow problems with low Reynolds numbers and generally simple geometry, such as homogeneous turbulence, mixing layers, and flat channel flows. Despite the fact that LES is used in such academic or essential setups still exists today, primarily for model validation and a basic comprehension of flow physics, etc. When the RANS technique has failed, emphasis has changed to more intricate arrangements with flow characteristics. Particularly, corporate interest in applying LES to complicated engineering flows has been stimulated by decades of advancement in LES and the advent of cheap workstation clusters and massively parallel computers. Nevertheless, the RANS technique has not been substituted by LES, and it seems unlikely that it will be for some time due to two key factors, computational analytical tool for real-world engineering challenges firstly, notwithstanding the present computing ability for practical purposes, performing LES routinely still costs far too much in terms of computing; secondly, LES is not yet mature enough for users without sufficient results can be achieved with the level of solution accuracy that can be anticipated using experience and knowledge. Currently, LES has wide range of applications in turbulent flows, gas turbine, jet noise, aeroacoustics, and atmospheric science [1].

2.3 Future challenges

In the future, LES will be properly used for a wider series of flow problems and for more difficult problems with more multi-disciplinary uses. Nevertheless, numerous major issues/challenges related with LES and its applications such as wall layer modeling, SGS modeling, LES of turbulent combustion, generation methods for inflow boundary conditions, etc., are still existing. Before LES can become a trustworthy, strong engineering analysis tool that can be utilized as a substitute for RANS, there are still important problems that need to be overcome. It is extremely improbable that LES will entirely overtake RANS and become a design tool for the foreseeable future, without considerable years of LES experience [1].

Actually, the PBL is more complex as compared with LES for simulation of systems; however, this complexity is generated due to heterogeneous nature of the considering surface. For instance, the earth land surface is described by spatially varying elements, urban expansion, and undulating grounds, which can merge circulations and therefore alter the turbulence dynamics. These complex surfaces may

significantly affect turbulence transport in many climate applications, for example, vegetation development, pollution, cloud formation, and storm formation. In summary, the LES is more employed than realistic PBL for multi-dimensional environmental flows.

Abbreviations

large eddy simulation	LES
Sub-grid scale	SGS
Reynolds-averaged Navier-Stokes	RANS
Direct numerical simulation	DNS
Turbulent kinetic energy	TKE
Planetary boundary layer	PBL
Digital filter generator	DFG
Periodic boundary condition	PBC

Author details

Aamir Shahzad*, Muhammad Kashif and Fazeelat Hanif
Modeling and Simulation Laboratory, Department of Physics, Government College University Faisalabad (GCUF), Faisalabad, Pakistan

*Address all correspondence to: aamirshahzad_8@hotmail.com

IntechOpen

References

[1] Zhiyin Y. Large-eddy simulation: Past, present and the future. Chinese Journal of Aeronautics. 2015;**28**(1):11-24

[2] Menzies. Large eddy simulation applications in gas turbines. Philosophical Transactions of the Royal Society A. 2009;**367**:2827-2838

[3] Tucker P. The LES model's role in jet noise. Progress in Aerospace Sciences. 2008;**44**(6):427-436

[4] Meneveau C, Katz J. Scale-invariance and turbulence models for large-eddy simulation. Annual Review of Fluid Mechanics. 2000;**32**(1):1-32

[5] Domaradzki JA, Adams NA. Direct modelling of subgrid scales of turbulence in large eddy simulations. Journal of Turbulence. 2002;**3**(1):024

[6] Moeng CH, Sullivan PP. Large-eddy simulation. Encyclopedia of Atmospheric Sciences. 2015;**2**:232-240

[7] Veloudis I, Yang Z, McGuirk JJ, Page GJ, Spencer A. Novel implementation and assessment of a digital filter based approach for the generation of LES inlet conditions. Flow, Turbulence and Combustion. 2007;**79**(1):1-24

We are IntechOpen,
the world's leading publisher of Open Access books
Built by scientists, for scientists

6,300
Open access books available

171,000
International authors and editors

190M
Downloads

154
Countries delivered to

Our authors are among the

TOP 1%
most cited scientists

12.2%
Contributors from top 500 universities

BOOK CITATION INDEX
CLARIVATE ANALYTICS
INDEXED

WEB OF SCIENCE™

Selection of our books indexed in the Book Citation Index
in Web of Science™ Core Collection (BKCI)

Interested in publishing with us?
Contact book.department@intechopen.com

Chapter

An Effective $\mathcal{H}^2$-LU Preconditioner for Iterative Solution of MQS Integral-Based Formulation Problems

Salvatore Ventre, Bruno Carpentieri, Gaspare Giovinco,
Antonello Tamburrino, Fabio Villone and Guglielmo Rubinacci

Abstract

We present iterative solution strategies for solving efficiently Magneto-Quasi-Static (MQS) problems expressed in terms of an integral formulation based on the electric vector potential. Integral formulations give rise to discrete models characterized by linear systems with dense coefficient matrices. Iterative Krylov subspace methods combined with fast compression techniques for the matrix-vector product operation are the only viable approach for treating large scale problems, such as those considered in this study. We propose a fully algebraic preconditioning technique built upon the theory of $\mathcal{H}^2$-matrix representation that can be applied to different integral operators and to changes in the geometry, only by tuning a few parameters. Numerical experiments show that the proposed methodology performs much better than the existing one in terms of ability to reduce the number of iterations of a Krylov subspace method, especially for fast transient analysis.

Keywords: $\mathcal{H}^2$-matrix, LU decomposition, MQS volume integral formulation, time domain, preconditioning, eddy currents, controlled thermonuclear fusion

1. Introduction

In this work, we consider the numerical solution of the Magneto-Quasi-Static (MQS) problem expressed in terms of an integral formulation based on the electric vector potential [1–3]. Integral formulations give rise to discrete models characterized by linear systems with dense coefficient matrices. Iterative Krylov subspace methods combined with fast compression techniques for the matrix-vector product operation are the only viable approach for treating large scale problems, such as those considered in this work. In this framework, a key role is played by the choice of the preconditioner, which has to be (i) robust enough to reduce significantly the number of iterations required to converge toward an accurate numerical solution, and (ii) efficient to reduce the overall computational and memory costs for the iterative

solution. In this work, we focus on this critical computational aspect for the MQS problem. We propose a fully algebraic preconditioning technique built upon the theory of $\mathcal{H}^2$-matrix representation, which can be applied to different integral operators and to changes in the geometry only by tuning a few parameters.

Many algebraic preconditioning methods for solving dense linear systems arising from the discretization of integral operators are computed from a sparse approximation of the stiffness matrix, which retains the near-field mesh interactions giving rise to the most relevant contributions to the singular integrals of the model and is easy to be factorized or inverted [4–6]. However, our past experience in using such methods on our MQS problem, e.g., multilevel incomplete LU factorizations [7], sparse approximate inverses [8], and preconditioners computed from the sparse resistance matrix of the discrete system of equations (see Eq. 5 below) was not completely satisfactory. We found that the lack of global information due to the compact support of the sparse near-field matrix often results in slow convergence. For instance, in the CARIDDI code that implements the electric vector potential formulation of our problem [1, 9], a preconditioner based on the sparsity pattern arising from local interactions among neighboring basis functions is used to accelerate the iterative solution (see [10]). The aforementioned limitations are clearly shown in our numerical experiments, suggesting the need to develop global preconditioners that can incorporate contributions from the "far-field" interactions for this class of problems. In our model, far-field interactions can be included by taking into account the vector potential.

Prompted by these considerations, in this paper, we propose a class of preconditioners based on the so-called Hierarchical or $\mathcal{H}$-matrices [11], which provide a general mathematical framework for a highly compact and kernel independent accurate representation of integral equations with almost linear complexity [12]; see [13] for an example of application. $\mathcal{H}$ -matrices can be used to define global preconditioners built by means of the decomposition of small rank blocks at a moderate memory requirement. In previous works by other authors, highly efficient approximate LU-factorization and multilevel sparse approximate inverses preconditioners of boundary element matrices requiring an almost linear computational cost have been developed (see [14]) by means of the fast arithmetic of $\mathcal{H}$ -matrices. The novelty of this work is to use the latest development of $\mathcal{H}$ -matrices, that is, $\mathcal{H}^2$ -matrix theory [15, 16].

The paper is organized as follows. In Section 2, we present the MQS volume integral formulation used in our study and its numerical implementation. In Section 3, we establish the need for an effective preconditioner for our problem. In Section 4, we outline some fundamental properties of $\mathcal{H}^2$-matrix theory, and in Section 5, we describe the computational steps of a matrix factorization that has $\mathcal{O}(N \cdot \log{(N)})$ complexity, N being the number of DoFs (Degrees of Freedom) and is applied for the design of our preconditioner. We assess the effectiveness of the proposed method for eddy current computations in fusion devices simulations by numerical experiments in Section 6, also against other algebraic preconditioning strategies. Finally, in Section 7, we draw some concluding remarks arising from the study and some perspective for future work.

2. The volume integral numerical formulation

Here we recall the main assumptions at the basis of a Magneto-Quasi-Static volume integral formulation and of its numerical implementation. We refer to a conducting

region V_C, without any topological constraint, characterized by the ohmic constitutive equation $\mathbf{J} = \sigma\mathbf{E}$, where $\mathbf{J}$ is the current density, σ is the material conductivity, and $\mathbf{E}$ is the electric field induced in the conductor by a set of time-varying external sources distributed with assigned current density $\mathbf{J}_S$.

The relevant equations in the magneto-quasi-stationary limit are

$$\mathbf{E} = -\frac{\partial\mathbf{A}}{\partial t} - \nabla\varphi \tag{1}$$

$$\nabla \times \mathbf{A} = \mathbf{B} \tag{2}$$

where

$$\mathbf{A}(\mathbf{r}, t) = \frac{\mu_0}{4\pi}\int_{V_c}\frac{\mathbf{J}(\mathbf{r}', t)}{|\mathbf{r} - \mathbf{r}'|}dV' + \mathbf{A}_s(\mathbf{r}, t) \tag{3}$$

and

$$\mathbf{A}_s(\mathbf{r}, t) = \frac{\mu_0}{4\pi}\int_{\mathbb{R}^3 - V_c}\frac{\mathbf{J}_s(\mathbf{r}', t)}{|\mathbf{r} - \mathbf{r}'|}dV'. \tag{4}$$

By imposing the Ohm law in weak form, we have

$$\int_{V_c}\mathbf{W} \cdot \left\{\sigma^{-1}\mathbf{J} + \frac{\partial}{\partial t}\left[\frac{\mu_0}{4\pi}\int_{V_c}\frac{\mathbf{J}(\mathbf{r}', t)}{|\mathbf{r} - \mathbf{r}'|}dV'\right] + \frac{\partial\mathbf{A}_s}{\partial t}\right\}dV = 0 \tag{5}$$

for any $\mathbf{W} \in S$ and with $\mathbf{J} \in S$, S being the set of solenoidal vector functions with continuous normal component across V_C and zero normal component on the boundary of V_C.

The numerical model implemented in the CARIDDI code [1, 9] is obtained by applying the Galerkin method to Eq. (5), having expanded the unknown currents $\mathbf{J}$ as $\mathbf{J}(\mathbf{r}, t) = \sum_k I_k(t)\nabla \times \mathbf{N}_k(\mathbf{r})$, where $\mathbf{N}_k$ is the set of edge element basis functions whose uniqueness is assured by the tree-cotree gauge [17]. Upon discretization, we obtain the following linear dynamical system:

$$\begin{cases} \mathbf{L}\dfrac{d\mathbf{I}}{dt} + \mathbf{R}\mathbf{I} = -\dfrac{d\mathbf{V}_0}{dt}, & t \geq 0 \\ \mathbf{I}(0) = \mathbf{i}_0 \end{cases}, \tag{6}$$

where $\mathbf{I}(t) = [I_i(t)], \mathbf{R} = [R_{ij}], \mathbf{L} = [L_{ij}], \mathbf{V}_0(t) = [V_{0,i}(t)]$ and

$$R_{ij} = \int_{V_c}\nabla \times \mathbf{N}_i(\mathbf{r}) \cdot \sigma^{-1}\nabla \times \mathbf{N}_j(\mathbf{r})dV, \tag{7}$$

$$L_{ij} = \frac{\mu_0}{4\pi}\int_{V_c}\int_{V_c}\frac{\nabla \times \mathbf{N}_i(\mathbf{r}) \cdot \nabla \times \mathbf{N}_j(\mathbf{r}')}{|\mathbf{r} - \mathbf{r}'|}dVdV', \tag{8}$$

$$V_{0,k}(t) = \int_{V_c}\nabla \times \mathbf{N}_k(\mathbf{r}) \cdot \mathbf{A}_s(\mathbf{r}, t)dV. \tag{9}$$

The quantity $\mathbf{i}_0$ in (6) denotes the prescribed initial condition. The vector potential $\mathbf{A}_s(\mathbf{r}, t)$ is produced by a known source current density $\mathbf{J}_s(\mathbf{r}, t)$, and it can be computed by means of the Biot-Savart law. For the sake of simplicity, we assume that the source current density $\mathbf{J}_s$ is due to the current $i_s(t)$ flowing in a given coil.

The ODE in (6) is integrated in time by the following scheme [18]:

$$\begin{cases} \mathbf{AI}_n = \mathbf{LI}_{n-1} + \mathbf{V}_{0,n} - \mathbf{V}_{0,n-1} \\ \mathbf{I}_0 = \mathbf{i}_0 \end{cases}, \tag{10}$$

where $\mathbf{I}_n = \mathbf{I}(n\Delta t)$ and $\mathbf{V}_n = \mathbf{V}(n\Delta t)$, and matrix $\mathbf{A}$ is expressed as

$$\mathbf{A} = \mathbf{R}\Delta t + \mathbf{L}. \tag{11}$$

The quantity Δt is the time integration step. Matrix $\mathbf{R}$ is sparse and local, whereas $\mathbf{L}$ is fully populated because it arises from the discretization of an integral operator. Note that $\mathbf{R}$, $\mathbf{L}$, and $\mathbf{A}$ are positive definite. The solution of large linear systems with a dense coefficient matrix poses a relevant computational challenge as it requires fast matrix solvers with reduced algorithmic and memory complexity. In this work, we solve Eq. (10) iteratively, for each prescribed n. To speed up the iterative solution, we develop an accurate and computationally efficient preconditioner $\mathbf{P}$ built upon the $\mathcal{H}^2$-matrix representation of matrix $\mathbf{A}$.

3. The need of an effective preconditioner

As it is well known, the main operations that are performed at each step of an iterative solver are: (i) the computation of the matrix-by-vector product $\mathbf{Ax}$, and (ii) the application of the preconditioner. The overall computational cost of the iterative solution is then proportional to the number of arithmetic operations required to carry out the multiplication $\mathbf{Ax}$ and to the number of iterations that are necessary to converge to a user-defined accuracy. The role of the preconditioner is to reduce the number of iterations and, ultimately, the overall solution cost [19]. In this work, we apply the preconditioner from the left and replace the linear system in (10) with the new equivalent system

$$\mathbf{P}^{-1}\mathbf{AI}_n = \mathbf{P}^{-1}(\mathbf{LI}_{n-1} + \mathbf{V}_{0,n} - \mathbf{V}_{0,n-1}), \tag{12}$$

where the preconditioned stiffness matrix $\mathbf{P}^{-1}\mathbf{A}$ is assumed to be well conditioned and to have most of its eigenvalues clustered around point one of the spectrum. Therefore, the "ideal" preconditioner has to be a good approximation to $\mathbf{A}^{-1}$. A critical issue in this context is the dependence of matrix $\mathbf{A}$ from Δt. In fast transient analysis, Δt has to be small enough to model properly the underlying dynamics. On the other hand, in slow transients Δt has to be large enough to cover the full-time interval of interest at acceptable computational cost. The dependence of $\mathbf{A}$ on Δt yields the dependence of $\mathbf{P}$ on Δt. According to (8), for small Δt the preconditioner should be tailored mainly on $\mathbf{L}$, whereas for large Δt the preconditioner should be tailored mostly on $\mathbf{R}$. Here and in the following, "small" and "large" Δt should be intended as compared with the slowest eigenmodes of the dynamical matrix $\mathbf{L}^{-1}\mathbf{R}$. In intermediate cases (Δt neither too small nor too large), the preconditioner should depend on both $\mathbf{R}$
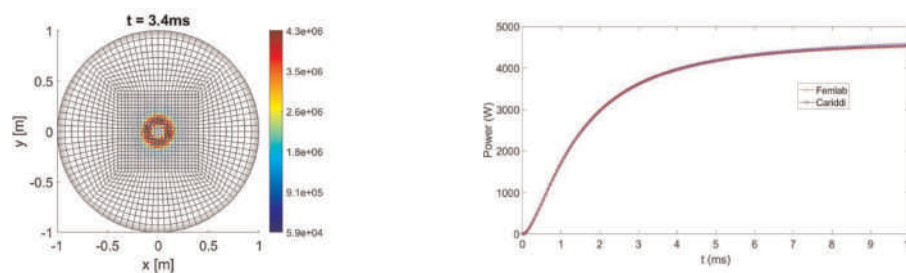
Figure 1.
Left: discretization of the plate used for assessing the performances of the preconditioner, together with the induced current distribution due to a current on a coaxial ring in a significant instant of the transient. Right: power losses on the plate as a function of time computed by CARIDDI (blue) and by Femlab© code (red), under the hypothesis of axisymmetry.

and $\mathbf{L}$. Since the use of an implicit time stepping does not impose specific restrictions on Δt, the appropriate value of Δt depends on the underlying dynamics induced by the source, i.e., on the rate of change of $\mathbf{V}_0(t)$ defined in (9) and appearing in (6).

A canonical waveform for $i_s(t)$, which can be used as the elementary building block to approximate more complex waveforms[1], is given by a linear ramp $i_s(t) = \alpha t$, for $t \geq 0$, being α the rate of change for the electrical current. Consequently, $\mathbf{V}_0(t) = \mathbf{W}t$ for $t \geq 0$ is also linear. The source term $\mathbf{V}_{0,n} - \mathbf{V}_{0,n-1}$ is equal to $\mathbf{W}\Delta t$, which is constant for any n. Let us consider a transient starting from a vanishing initial condition $\mathbf{i}_0 = \mathbf{0}$ in (6). As long as the current at the previous step is negligible, Eq. (10) reduces to $\mathbf{AI}_n = \mathbf{W}$. Therefore, the matrix to be inverted is $\mathbf{A}$, and the preconditioner $\mathbf{P}$ has to be "tuned" on such matrix. On the other hand, when the stationary state is achieved, the solution $\mathbf{I}_n$ is constant, and Eq. (10) reduces to $(\Delta t\mathbf{R} + \mathbf{L})\mathbf{I}_\infty = \mathbf{LI}_\infty + \mathbf{W}$, that is, $\Delta t\mathbf{RI}_\infty = \mathbf{W}$. In this case, the matrix to be inverted is $\mathbf{R}$, and the preconditioner needs to be "tuned" on $\mathbf{R}$. This explains the reason why the preconditioner based on matrix $\mathbf{R}$ is not effective in dealing with fast dynamics. As an example, we measured its performances on a 3D transient eddy current problem where the driving current has a time-varying waveform given by $i_s(t) = \alpha t$, for $t \geq 0$, where $\alpha = 10^7 Hz$. This electrical current flows in a circular ring ($R = 10cm$), centered on the axis of a flat conducting disk (radius $R_0 = 1m$, thickness $3mm$). Validation is carried out against the Femlab© code [Version 3.51], as shown in **Figure 1** (right). **Figure 1**(left) shows the induced current distribution at $t = 3.4\,ms$ together with the finite element mesh used in the computation and the ohmic losses in the conductor. **Figure 2** shows the characteristics
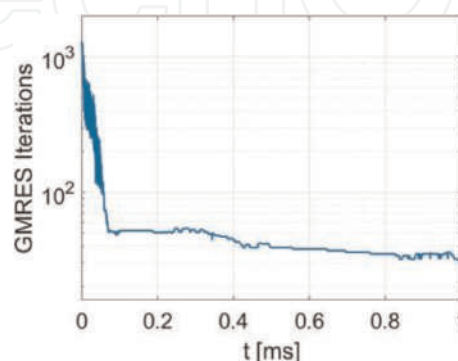

Figure 2.
Number of iterations of GMRES using R as a preconditioner during the transient.

---

[1] The linear ramp can be used to build a piecewise linear approximation of a continuous function.

of the iterative inversion using $\mathbf{P} = \mathbf{R}$ as a preconditioner and the Generalized Minimal Residual Method (GMRES) [20] as the iterative solver. Since the number of discrete unknowns for this test problem is 22,657, the results of **Figure 2** clearly show that that the resistive preconditioner ($\mathbf{P} = \mathbf{R}$) is not effective at the early stage of the transient phase, when the inductive effects accounted by matrix $\mathbf{L}$ are not negligible.

4. $\mathcal{H}^2$-matrix representation

The $\mathcal{H}^2$-matrix representation is widely used for storing efficiently a dense matrix arising from the discretization of a boundary integral equation [15]. In $\mathcal{H}^2$-matrix theory, the degrees of freedom (DoFs) of the underlying finite element mesh are partitioned into small subsets (or cluster) of nodes (they are edges in our problem). We illustrate the partitioning process with reference to the geometry shown in **Figure 3** that will be described in detail in the next section. At the first step, the set of DoFs is split in two clusters of nodes (see **Figure 3** (left)); then, each cluster is split recursively (see **Figure 3** (center) and (right)) until a minimum number of DoFs (called leaf size or LS) is reached by the recursive partitioning. The binary split is carried out using geometric information from the mesh. First, the coordinates of the barycenter of the DoFs are computed along the $x, y,$ and z axes. Then, the axis (either x or y or z) corresponding to the largest geometric coordinate in magnitude is selected, and the DoFs are split accordingly by introducing a plane orthogonal to this axis and passing through the median of the distribution of the coordinates of the DoFs along the same axis (see **Figure 4**). A key point of the partitioning is that cluster of nodes are built to contain DoFs that are geometrically neighbors in the finite element mesh. From a geometric viewpoint, all the DoFs belonging to a given cluster of edges are
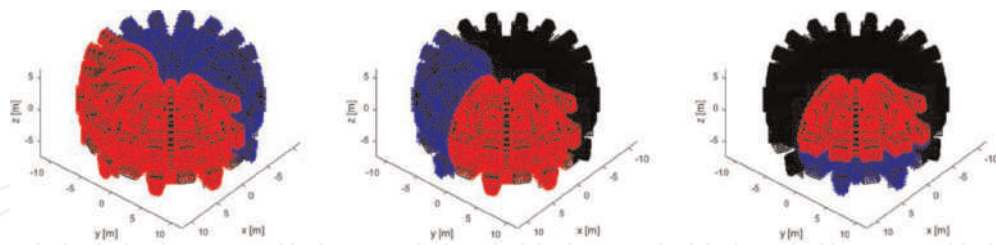

Figure 3.
The hierarchical partitioning of the DoFs. Left: The DoFs of the mesh are split into two sets (or clusters) of nodes. Center: The DoFs of the red set at the first step are partitioned in two subsets. Right: The DoFs of the red set at the second step are further partitioned into two subsets and so on.
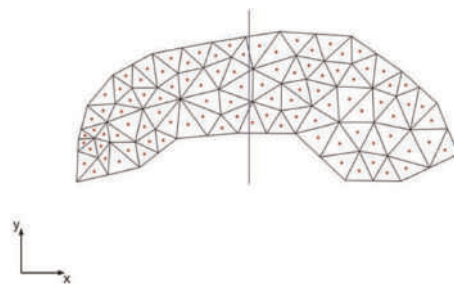

Figure 4.
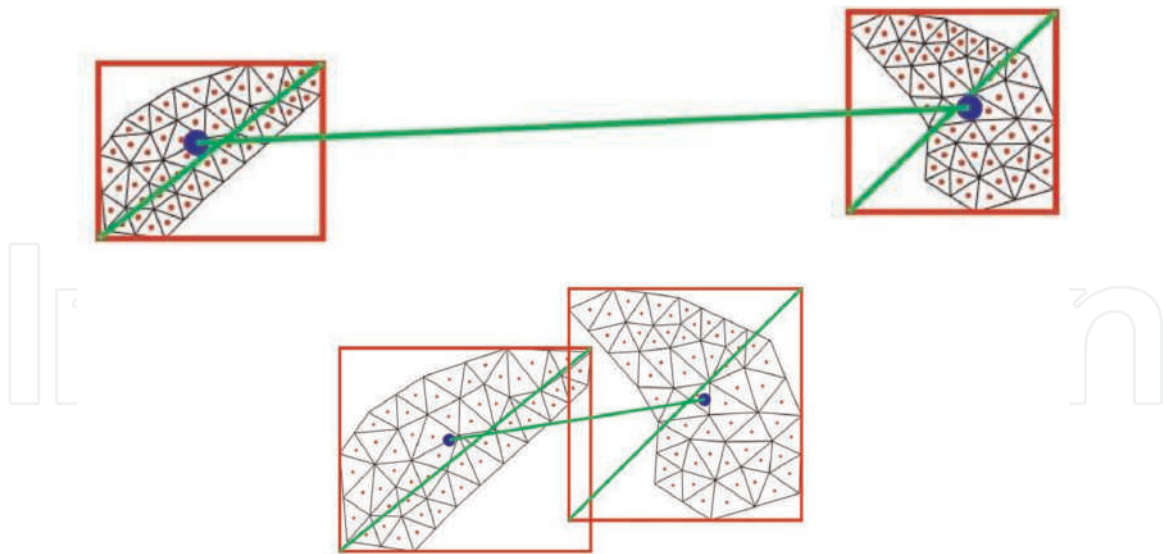*Example of DOFs splitting for a two-dimensional (2D) unstructured mesh.*

Figure 5.
Top: Two clusters that are classified as far. The size of the individual regions (given by the diagonal of the parallelepiped that bounds the region) occupied by the DoFs is larger than the distance between the barycenter of the clusters. Bottom: Two clusters that are classified as near. The size of the individual regions occupied by the DoFs is not large enough if compared with the distance between the barycenter of the clusters.

contained within a parallelepiped, which is parallel to the coordinate planes (see **Figure 5**). The key parameters related to a cluster N_k are: (i) the number of DoFs contained in the cluster, (ii) the parallelepiped P_k containing the DoFs of N_k, (iii) the diameter $d_k = |P_k|$ and the center c_k of P_k.

This partitioning process can be efficiently represented in a binary tree data structure. The binary tree is of paramount importance to classify interactions between clusters of DoFs in terms of near (or *inadmissible*) interactions and far (or *admissible*) interactions. An interaction is defined far if the two clusters of DoFs are geometrically well separated in the mesh, and near otherwise, as shown in **Figure 5**. We will use a simple criterion based on geometric distance for the classification. Two cluster of nodes N_k and N_j are named far if the ratio

$$\xi_{kj} \hat{=} \frac{|\mathbf{c}_k - \mathbf{c}_j|}{\max\left(d_k, d_j\right)}, \tag{13}$$

is greater than a suitable threshold $\xi_{THR} > 1$.

The mesh partitioning into clusters of nodes is represented by means of the so-called Block Cluster Tree (BCT) data structure (see **Figure 6** and [16] for details). Thanks to its binary structure, the BCT can be easily mapped into a corresponding partitioning of the discretization matrix $\mathbf{L}$ and, hence, of $\mathbf{A}$ into small blocks, yielding naturally a decomposition $\mathbf{A} = \mathbf{A}_{near} + \mathbf{A}_{far}$.

Interactions of near clusters lead to high or full-rank blocks (the near part $\mathbf{A}_{near}$ of $\mathbf{A}$) that need to be explicitly computed and stored, whereas far clusters interactions give rise to low-rank blocks (the far part $\mathbf{A}_{far}$ of $\mathbf{A}$). In the $\mathcal{H}^2$ -matrix representation, the far interactions between, say, the i-th and j-th clusters, are approximated by a low-rank matrix factorization of the form

$$\mathbf{A}_{ij} \approx \mathbf{V}_i \cdot \mathbf{S}_{ij} \cdot \mathbf{V}_j^{\mathrm{T}}. \tag{14}$$
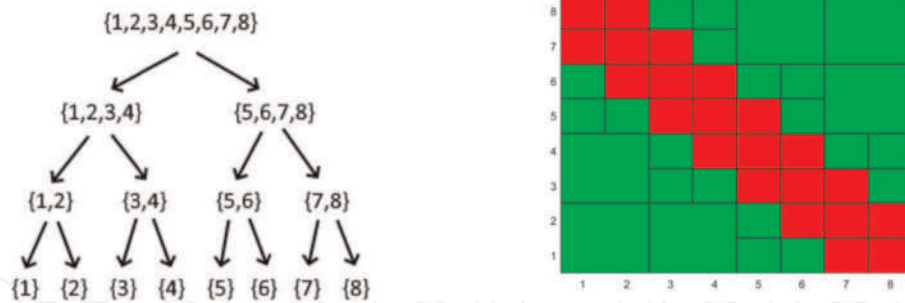
Figure 6.
Example of cluster tree partitioning (n = 8 clusters). Left: The block cluster tree. Right: Matrix representation of the block cluster tree after four levels of matrix block partitioning. Admissible blocks are green, and inadmissible blocks are red.

Such factorization can be obtained by using a degenerate Lagrange polynomial approximation of the kernel [3]. This is possible because the kernel defined in Eq. (8) is smooth when it is evaluated on the far field. The columns of matrix $\mathbf{V}_i$ represent the expansion basis for the DoFs associated to the i-th cluster, and $\mathbf{S}_{ij}$ is the coupling matrix of dimensions $k_i \times k_j$ where k_i and k_j are the column dimensions of $\mathbf{V}_i$ and $\mathbf{V}_j$, respectively. It is worth noting that for far interactions, integers k_i and k_j are expected to be much smaller than the number of rows of matrices $\mathbf{V}_i$ and $\mathbf{V}_j$. This representation of the far field is highly efficient in terms of both memory and computational costs, since it involves only small-rank matrices ($\mathbf{V}_i$ for any i, and $\mathbf{S}_{ij}$ for any i and j). Indeed, linear memory complexity can be achieved by means of the $\mathcal{H}^2$ -matrix representation [12].

Hereafter, the following notation will be used: we denote by N_p the number of Lagrange points per direction used for the degenerate kernel approximation, and by e_{ij} the relative error of the low-rank representation of a matrix block $\mathbf{A}_{ij}$ associated to the interactions of the i-th and j-th far clusters:

$$e_{ij} = \frac{\left\| \mathbf{A}_{ij} - \mathbf{V}_i \mathbf{S}_{ij} \mathbf{V}_j^{\mathrm{T}} \right\|}{\left\| \mathbf{A}_{ij} \right\|},$$ (15)

where $\| \cdot \|$ is the conventional 2-norm for matrices.

5. The $\mathcal{H}^2$-matrix factorization

To develop an effective preconditioner $\mathbf{P}$ for solving Eq. (12), first we set $\mathbf{P}$ equal to $\mathbf{A}_{\mathcal{H}^2}$, the $\mathcal{H}^2$-matrix representation of $\mathbf{A}$. Then, by exploiting the hierarchical structure of $\mathbf{A}_{\mathcal{H}^2}$, we build an efficient LU factorization of $\mathbf{P}$. A core operation of the factorization of $\mathbf{P}$ is the computation of the Shur complement for the block matrix $\mathbf{A}_{\mathcal{H}^2}$. In general, this computation is very expensive. However, the $\mathcal{H}^2$-approximation introduces many off-diagonal blocks, which are vanishing upon a suitable orthonormal transformation of $\mathbf{A}_{\mathcal{H}^2}$. Hence, the overall factorization costs of $\mathbf{P}$ can be significantly reduced to $\mathcal{O}(N \cdot \log(N))$, N being the number of DoFs [16, 21].

The factorization algorithm proceeds level by level, starting from the last level of the BCT and computing a partial LU decomposition at each cluster of the tree. With

reference to the leaf level, the last level in the BCT, the original stiffness matrix $\mathbf{P}$ is expressed as:

$$\mathbf{P} = \mathbf{L_o}\mathbf{C_1}\mathbf{U_p} \tag{16}$$

where $\mathbf{C_1} = diag\left(\mathbf{I}_{d_1}, \mathbf{I}_{d_2}, \dots, \mathbf{I}_{d_{\#(leaf\ clusters)}}, \mathbf{C}\right)$ and $\mathbf{L_o}$ and $\mathbf{U_p}$ can be easily inverted because they are lower and upper triangular matrices, respectively. In (16), $\mathbf{I}_{d_i}$ is an identity matrix of proper size, and $\mathbf{C}$ is a full matrix of dimension much smaller than the original matrix $\mathbf{P}$. After the factorization (16) has been computed at the current level, the algorithm continues at a higher level of the BCT by applying recursively the same process to matrix $\mathbf{C}$.

Two key computational aspects have to be carefully considered and monitored during the factorization. The first one is the accuracy of the approximation $\mathbf{A}_{\mathcal{H}^2}$ to $\mathbf{A}$, which is used to define the preconditioner $\mathbf{P}$. Obviously, the closer $\mathbf{A}_{\mathcal{H}^2}$ to $\mathbf{A}$, the more effective $\mathbf{P}$ is as a preconditioner for the iterative solver. The second aspect refers to the error introduced in the approximated factorization of $\mathbf{P}$. In the rest of the section, we discuss in detail the factorization of $\mathbf{P}$.

Specifically, matrix $\mathbf{P}$ is factorized in terms of a partial LU decomposition [16]. For doing this operation efficiently, using some properties of $\mathcal{H}^2$-matrix theory is of paramount importance to reduce the overall cost. The complete multilevel factorization algorithm is presented in Algorithm 1.

Algorithm 1: The iterative factorization algorithm.

---

1. Set $\mathbf{A}_{curr} = \mathbf{A}_{\mathcal{H}^2}$.

2. **for** k=last level to the root **do.**

3.   **for** any cluster i at level k **do.**

4.   Set $\mathbf{A}_{curr} = \mathbf{Q}_i^H \mathbf{A}_{curr} \mathbf{Q}_i$, where $\mathbf{Q}_i$ is defined in Eq. (14).

5.   Compute the partial LU factorization of $\mathbf{A}_{curr}$ as.

   $\mathbf{A}_{curr} = \mathbf{L}_i \begin{bmatrix} \mathbf{I} & \mathbf{0} \\ \mathbf{0} & \tilde{\mathbf{A}}_{curr} \end{bmatrix} \mathbf{U}_i$, where $\mathbf{L}_i$ and $\mathbf{U}_i$ are lower and upper triangular matrices, respectively.

6.   Set $\mathbf{A}_{curr} = \begin{bmatrix} \mathbf{I} & \mathbf{0} \\ \mathbf{0} & \tilde{\mathbf{A}}_{curr} \end{bmatrix}$

7.   **end for.**

8. **end for.**

At step 5, matrix $\mathbf{Q}_i$ encompasses the basis related to the i-th cluster as follows:

$$\mathbf{Q}_i = diag\left\{\mathbf{I}_{d_1}, \mathbf{I}_{d_2}, \dots, \begin{bmatrix} \mathbf{V}_i^\perp, & \mathbf{V}_i \end{bmatrix}, \dots, \mathbf{I}_{\#(leaf\ clusters)}\right\}. \tag{17}$$

The orthonormal transformation at step 5 is computationally cheap to carry out because of the simplified structure of matrix $\mathbf{Q}_i$, which involves only the i-th diagonal block of matrix $\mathbf{A}_{curr}$, of dimension $d_i \times d_i$. In the definition of $\mathbf{Q}_i$ in Eq. (17), $\mathbf{V}_i^{\perp}$ is the orthogonal complement of the cluster basis $\mathbf{V}_i$. This update of $\mathbf{A}_{curr}$, which essentially corresponds to a change of basis, is very effective on the far blocks to the i-th diagonal block of $\mathbf{A}_{curr}$. Thanks to (14), it is easy to verify that the first $d_i - k_\ell$ rows of these blocks are zeroed out, where k_ℓ is the rank used for the approximate factorization at the ℓ-th level of the BCT. Since most of the blocks in the original matrix $\mathbf{A}$ are far, they will be efficiently compressed by the procedure described above (see [16]). At step 10, a complete LU factorization of a dense matrix is required. However, this operation is rather cheap because matrix $\tilde{\mathbf{A}}_{curr}$, resulting from the previous steps, is small.

We highlight an important computational aspect of Algorithm 1. Upon processing the i-th cluster at step 5, the partial LU factorization of $\mathbf{A}_{curr}$ writes as

$$\mathbf{A}_{curr} = \begin{bmatrix} \mathbf{A}_{i'i'} & \mathbf{A}_{i'p} \\ \mathbf{A}_{pi'} & \mathbf{A}_{pp} \end{bmatrix} = \underbrace{\begin{bmatrix} \mathbf{L}_{i'i'} & \mathbf{0} \\ \mathbf{A}_{pi'}\mathbf{U}_{i'i'}^{-1} & \mathbf{I} \end{bmatrix}}_{\mathbf{L}_i} \begin{bmatrix} \mathbf{I} & \mathbf{0} \\ \mathbf{0} & \tilde{\mathbf{A}}_{curr} \end{bmatrix} \underbrace{\begin{bmatrix} \mathbf{U}_{i'i'} & \mathbf{L}_{i'i'}^{-1}\mathbf{A}_{i'p} \\ \mathbf{A}_{pi'} & \mathbf{I} \end{bmatrix}}_{\mathbf{U}_i} \qquad (18)$$

where $\mathbf{A}_{i'i'} = \mathbf{L}_{i'i'}\mathbf{U}_{i'i'}$, i' is equal to the number of nodes in the i-th clusters minus the approximation rank at the current level, and

$$\tilde{\mathbf{A}}_{curr} = \mathbf{A}_{pp} - \mathbf{A}_{pi'}\mathbf{U}_{i'i'}^{-1}\mathbf{L}_{i'i'}^{-1}\mathbf{A}_{i'p}. \qquad (19)$$

Clearly, matrix $\tilde{\mathbf{A}}_{curr}$ still has a block structure, which is inherited from the cluster-to-cluster interactions. Contributions to the update term $\mathbf{A}_{pi'}\mathbf{U}_{i'i'}^{-1}\mathbf{L}_{i'i'}^{-1}\mathbf{A}_{i'p}$ due to near clusters mesh interactions are computed explicitly. On the other hand, contributions due to far clusters interactions are approximated using a low-rank factorization of the form given by Eq. (11), where cluster bases are simply updated by appending new columns pointing in the direction of the space orthogonal to the range of $\mathbf{V}_i$, thus avoiding to re-compute the whole basis from scratch. This approximate computation of the Schur complement is essential to achieve $\mathcal{O}(N \cdot \log(N))$ complexity. For further details, see [16].

Summing up, in this method two important sources of errors are introduced during the factorization:

- The far-field approximation. Rather than factorizing the original matrix $\mathbf{A}$, we factorize its $\mathcal{H}^2$-matrix representation $\mathbf{A}_{\mathcal{H}^2}$. The accuracy of this approximation depends on the number of Lagrange points (N_p) used to compute the $\mathcal{H}^2$-matrix approximation of $\mathbf{A}$.

- The error introduced in the Schur complement update (6) for each processed cluster. This error is controlled by a suitable threshold parameters and is the dominant one in the presented algorithm.

6. Numerical results and discussion

The numerical example described in this section refers to eddy current computations in fusion devices [22, 23]. The mesh of our case study is depicted in **Figure 7**.
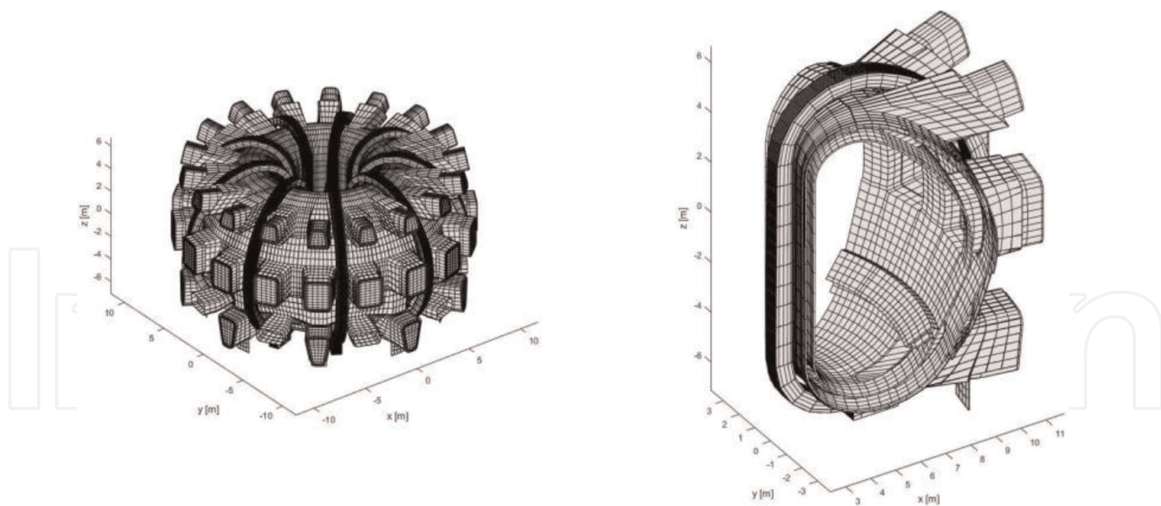
Figure 7.
The analyzed case study. Left: mesh of ITER magnet system. Right: A 45° sector.

The plasma made of hydrogen isotopes inside the vacuum chamber of the device can be broadly described as a deformable current-carrying conductor in the frame of the so-called Magneto-Hydro-Dynamics (MHD) equations. Consequently, the electromagnetic interaction of the plasma with surrounding conducting structures is fundamental in the description of the behavior of such devices. In nominal situations, when one wants to intentionally control plasma current, position, and shape [24], this interaction occurs on a time scale of the order of tens or hundreds of milliseconds in the largest existing devices. Conversely, also off-normal events can occur, such as the so-called disruptions [25]; in such cases, the plasma energy content is released on a much shorter time (milliseconds or submilliseconds time range).

It should be noted that the geometry of fusion devices, which is ideally axisymmetric, in practice can show significant three-dimensional features (ports, holes, cuts, slits, etc.), which must be taken into account when computing the magnetic fields, the current densities, and the related force densities, which are required to get a satisfactory electromagnetic modeling. Summing up, fusion devices are particularly challenging from the computational electromagnetic viewpoint: they are multiphysics devices, with complicated three-dimensional features giving rise to huge computational models, with different timescales of interests involved. The methods developed in the present paper are designed to enable us to tackle such intrinsic difficulties to some extent. The number of nodes and elements of the finite element mesh is 249849 and 132562, respectively, resulting in 145243 DoFs. The first three partitioning levels for such mesh are schematically depicted in **Figure 3**. In this study, the time step Δt is set equal to $1ms$ and $0.1ms$, to account for the different timescales mentioned above.

As aforementioned, the main operations required by an iterative solver are: (i) the computation of the matrix-by-vector product $\mathbf{Ax}$ and (ii) the application of the preconditioner at every iteration. We choose GMRES as the iterative solver. The preconditioner is the compressed approximate matrix $\mathbf{A}_{\mathcal{H}^2}$ presented in Section 5. Clearly, the use of a preconditioner introduces additional costs in terms of memory and computational cost, during the preprocessing and at each iteration. Therefore, it pays off only if there is a proper reduction of the number of required iterations. Here, to assess the performances of the preconditioner, we use matrix $\mathbf{A}$ without any approximation in computing the matrix-by-vector product during GMRES iterations. We stop the iterative process either when the initial preconditioned residual norm is

reduced by five orders of magnitude or after 90 iterations. In our case, the computational time required to apply the preconditioner is proportional to its memory footprint. This is because of the almost linear complexity of the overall procedure (see [16] for details): both computational time and memory requirements increase linearly with the number of DoFs.

The performance of the proposed approach depends mainly on two key parameters: the number of Lagrange points N_p and the leaf size LS. We remind that LS determines the size of matrix $\mathbf{A}_{near}$ arising from near cluster interactions, whereas N_p affects the number of columns of $\mathbf{V}_i$, the size of $\mathbf{S}_{ij}$ and, consequently, the accuracy of $\mathbf{A}_{far}$. It is worth noting that $\mathbf{A}_{far}$ in the $\mathcal{H}^2$ -matrix representation does not contribute significantly to the overall required memory: in all numerical experiments of this work, the memory required by $\mathbf{A}_{far}$ is less than 10% of the storage required by $\mathbf{A}_{near}$.

From (11), we have that the preconditioner memory footprint depends only on the storage of matrices $\mathbf{L}_0$, $\mathbf{U}_p$ and the dense but smaller block $\mathbf{C}$ of matrix $\mathbf{C}_1$ appearing in (16). **Figure 8** shows the memory required by the preconditioner (M_{LU}) as a function of LS and N_p. The result is normalized with respect to the memory required to store the full matrix $\mathbf{A}$, which is about 169 GB.

The memory footprint required by matrix $\mathbf{C}_1$ decreases with LS. Indeed, an increase of LS enlarges the size of the block-to-block interactions, resulting in a smaller reduced matrix $\mathbf{C}_1$ because of a more effective compression of the block-to-block interactions. On the other hand, the sizes of $\mathbf{L}_0$ and $\mathbf{U}_p$ depend on: (i) the size of the near part, strictly depending on LS, and (ii) the ability of the $\mathcal{H}^2$ -matrix representation to compress the admissible block-to-block far-field interactions.

If we reduce LS, the memory required by the near interactions matrix $\mathbf{A}_{near}$ decreases, but the memory required by the far-field block-to-block interactions matrix increases. Indeed, we observe that at $LS = 500$ the required memory depends on N_p, whereas for $LS = 2000$ the required memory is almost independent on N_p. Eventually, we have an intermediate dependence for $LS = 1000$. The drawback related to the memory demands can be addressed in a parallel environment.

To assess the effectiveness of the proposed preconditioner, we make a comparison with the "reference" preconditioner based solely on matrix $\mathbf{R}$. This choice resulted to be much more effective than many other state-of-the-art algebraic preconditioners, such as robust multilevel, incomplete LU factorizations, and sparse approximate inverse methods to accelerate the GMRES convergence. Also, we evaluated a preconditioner based on the sum of matrix $\mathbf{R}$ plus a contribution from matrix $\mathbf{L}$ on the same pattern of $\mathbf{R}$. This preconditioner failed to converge at increasing mesh size.
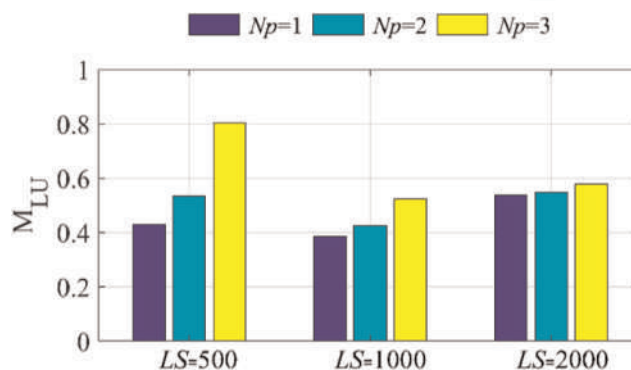

Figure 8.
Memory occupation as LS and N_p varies.

Summing up, finding a proper preconditioner for this class of large-scale problems is challenging.

Figure 9 (top $\Delta t = 1ms$) and (bottom $\Delta t = 0.1ms$) shows the preconditioned relative residual norm E_R of the GMRES solver versus the number of iterations for different LS and N_p.

The numerical results clearly show that:

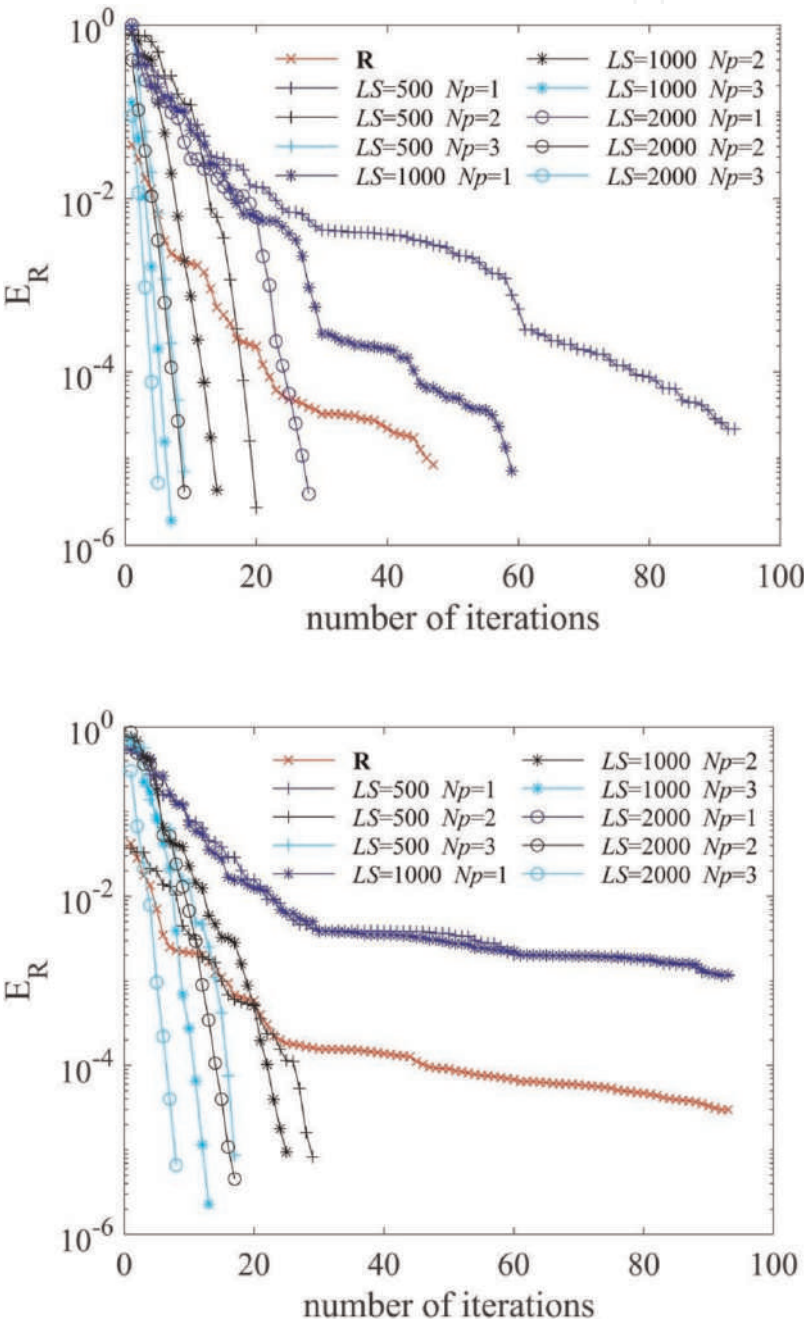- The $\mathcal{H}^2$-LU generally performs much better than the preconditioner based on **R** preconditioner.

Figure 9.
Performance of $\mathcal{H}^2$-LU preconditioner, for different values of the leaf size (LS) and number of Lagrange points (N_p). Top: $\Delta t = 1$ ms. bottom: $\Delta t = 0.1$ ms. performances from the reference preconditioner based on R are also shown.

- The efficiency of the preconditioner strongly depends on the choice of the parameters N_p and LS that control the accuracy of $\mathbf{A}_{far}$.

We highlight that the accuracy of $\mathbf{A}_{far}$ is rather low for $N_p = 1$ and that the preconditioner based on $\mathbf{R}$ performs better in this situation. In the other cases, the proposed $\mathcal{H}^2$-LU preconditioner outperforms the reference one based on $\mathbf{R}$, proving that it incorporates a good mechanism to balance contributions from matrices $\mathbf{L}$ and $\mathbf{R}\Delta t$ in $\mathbf{A}$. This explains why at the smaller Δt, when $\mathbf{L}$ gives the dominant contribution to $\mathbf{A}$, the number of iterations for the $\mathbf{R}$ based preconditioner increases. On the other hand, when using the $\mathcal{H}^2$-LU preconditioner, which accounts for both $\mathbf{R}\Delta t$ and the dominant part of $\mathbf{L}$, the number of iterations remains almost unchanged with Δt.

The accuracy of $\mathbf{A}_{far}$ is a critical point for the effectiveness of the proposed preconditioner. To asses this, we define two quantities, denoted as E_A and E_{SD}, that are the mean and the standard deviation for the relative error e_{ij} defined in (15) arising from all the admissible block-to-block pairs (i, j). As expected, **Figure 10** shows that the error decreases as N_p increases. Note that for $N_p = 1$, a relative error larger than 0.1 can be obtained. Eventually, the accuracy of the preconditioner is shown in **Figure 11** for different values of LS, N_p, and Δt. To quantify the error, we introduce the metric E_S defined as

$$E_S = \frac{\left\| I_{app} - I \right\|}{\|I\|}, \tag{20}$$

where I is computed using a direct method, whereas I_{app} is computed with the proposed preconditioned iterative solver. In (19), $\|\cdot\|$ is the 2-norm, and both I and I_{app} are evaluated at a prescribed time.
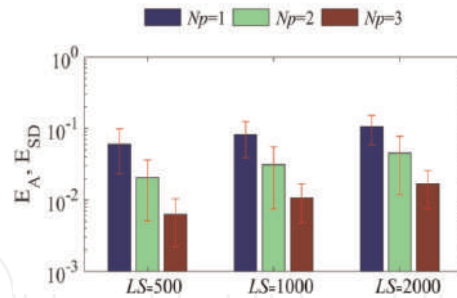

Figure 10.
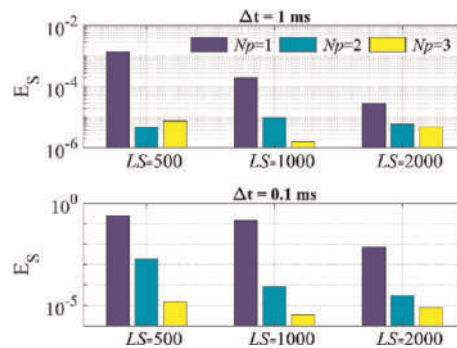*Mean and standard deviation of the relative error in A_{far}.*

Figure 11.
Solution error E_s, as LS, N_p, and Δt vary.

Figure 11 confirms that the accuracy of the solution increases with N_p. Only for $LS = 500$ and $\Delta t = 1ms$ the solution with $N_p = 3$ is a little bit less accurate than the one with $N_p = 2$. It is worth noting that as the accuracy of $\mathbf{A}_{far}$ increases, the iterative scheme converges in very few iterations. Summing up, these numerical results confirm that an efficient iterative solver for the CARIDDI integral model of the eddy current problem needs a preconditioner incorporating some far-field approximations from the interaction matrix $\mathbf{L}$.

7. Conclusions and future work

In this paper, a new preconditioner based on the $\mathcal{H}^2$-LU decomposition has been introduced for solving integral equations models for eddy current problems. The application case refers to a large-scale model arising in nuclear fusion devices. The numerical results show that the preconditioner exhibits better performances compared with the purely resistive preconditioner. Specifically, the required number of iterations has been strongly reduced at different time steps. Moreover, the increase of costs in terms of both memory and CPU time during the preprocessing and at each iteration is largely paid off by the reduced number of iterations. In our view, two possible areas of future developments are: (i) deploying a parallel implementation of the $\mathcal{H}^2$-LU decomposition in order to speed up the code execution and reduce the memory demands, and (ii) studying the performances of the method when it is used as a direct solver.

Acknowledgements

Author details

Salvatore Ventre[1], Bruno Carpentieri[2]*, Gaspare Giovinco[3], Antonello Tamburrino[1,4], Fabio Villone[5] and Guglielmo Rubinacci[5]

1 Department of Electrical Engineering and Information, University of Cassino and Southern Lazio, Cassino, Italy

2 Faculty of Computer Science, Free University of Bozen-Bolzano, Bolzano, Italy

3 Department of Civil and Mechanical Engineering, University of Cassino and Southern Lazio, Cassino, Italy

4 Department of Electrical and Computer Engineering, Michigan State University, East Lansing, USA

5 Department of Electrical Engineering and Information Technology, University of Naples Federico II, Napoli, Italy

*Address all correspondence to: bruno.carpentieri@unibz.it

IntechOpen

References

[1] Albanese R, Rubinacci G. Finite element methods for the solution of 3D eddy current problems. Advances in Imaging and Electron Physics. 1997;**102**: 1-86

[2] Rubinacci G, Tamburrino A, Villone F. Circuits/fields coupling and multiply connected domains in integral formulations. IEEE Transactions on Magnetics. 2002;**38**(2):581-584

[3] Rubinacci G, Tamburrino A. Automatic treatment of multiply connected regions in integral formulations. IEEE Transactions on Magnetics. 2010;**46**(8):2791-2794

[4] Carpentieri B. Algebraic preconditioners for the fast multipole method in electromagnetic scattering analysis from large structures: Trends and problems. Electronic Journal of Boundary Element. 2009;7(1):13-49

[5] Carpentieri B. Fast iterative solution methods in electromagnetic scattering. Progress in Electromagnetic Research. 2007;**79**:151-178

[6] Carpentieri B. A matrix-free two-grid preconditioner for boundary integral equations in electromagnetism. Computing. 2006;**77**(3):275-296

[7] Carpentieri B, Bollhöfer M. Symmetric inverse-based multilevel ILU preconditioning for solving dense complex non-hermitian systems in electromagnetics. Progress In Electromagnetics Research. 2012;**128**: 55-74

[8] Carpentieri B, Duff I, Giraud L, Sylvand G. Combining fast multipole techniques and an approximate inverse preconditioner for large electromagnetism calculations. SIAM Journal on Scientific Computing. 2005; **27**(3):774-792

[9] Albanese R, Rubinacci G. Solution of three dimensional eddy current problems by integral and differential methods. IEEE Transactions on Magnetics. 1988;**24**(1):98-101

[10] Rubinacci G, Ventre S, Villone F, Liu Y. A fast technique applied to the analysis of resistive wall modes with 3D conducting structures. Journal of Computational Physics. 2009;**228**(5): 1562-1572

[11] Hackbusch W. A sparse matrix arithmetic based on $\mathcal{H}$-matrices. Part i: Introduction to $\mathcal{H}$-matrices. Computing. 1999;**62**(2):89-108

[12] Börm S, Grasedyck L, Hackbusch W. Hierarchical Matrices. Leipzig: Max Planck Institute for Mathematics in the Sciences; 2003

[13] Voltolina D, Bettini P, Alotto P, Moro F, Torchio R. High-performance PEEC analysis of electromagnetic scatterers. IEEE Transactions on Magnetics. 2019;**55**(6):1-4

[14] Bebendorf M. Hierarchical LU decomposition-based preconditioners for BEM. Computing. 2005;**74**(3): 225-247

[15] Börm S. Efficient Numerical Methods for Non-Local Operators: $\mathcal{H}2$-Matrix Compression, Algorithms and Analysis. Vol. 14. Zürich, Switzerland: European Mathematical Society; 2010

[16] Ma M, Jiao D. Accuracy directly controlled fast direct solution of general $\mathcal{H}2$-matrices and its application to solving Electrodynamic volume integral equations. IEEE Transactions on

Microwave Theory and Techniques. 2017;**66**(1):35-48

[17] Albanese R, Rubinacci G. Integral formulation for 3D eddy-current computation using edge elements. IEE Proceedings A-Physical Science, Measurement and Instrumentation, Management and Education-Reviews. 1988;**135**(7):457-462

[18] Atkinson K, Han W, Stewart D. Numerical Solution of Ordinary Differential Equations. Vol. 108. Hoboken, New Jersey, U.S.: John Wiley & Sons; 2011

[19] Golub G, Loan CV. Matrix Computations: Johns Hopkins Studies in the Mathematical Sciences. third ed. Baltimore, MD, USA: The Johns Hopkins University Press; 1996

[20] Saad Y. Iterative Methods for Sparse Linear Systems. 2nd ed. Philadelphia: SIAM; 2003

[21] Ventre S, Carpentieri B, Giovinco G, Tamburrino A, Rubinacci G, Villone F. An $\mathscr{H}$2-LU preconditioner for MQS model based on integral formulation. In: Poster Presentation at the 22nd International Conference on the Computation of Electromagnetic Fields, COMPUMAG 2019, July 15–19. Paris, France; 2019

[22] Testoni P, Forte R, Portone A, Rubinacci G, Ventre S. Damping effect on the ITER vacuum vessel displacements during slow downward locked and rotating asymmetric vertical displacement events. Fusion Engineering and Design. 2018;**136**:265-269

[23] Ramogida G, Maddaluno G, Villone F, et al. First disruption studies and simulations in view of the development of the DEMO physics basis. Fusion Engineering and Design, Open Access. 2015;**96–97**:348-352

[24] Ariola M, Pironti A. Magnetic Control of Tokamak Plasmas. Vol. 187. Berlin/Heidelberg, Germany: Springer; 2008

[25] Hender T, Wesley J, Bialek J, et al. MHD stability, operational limits and disruptions. Nuclear Fusion. 2007;**47**(6): S128

We are IntechOpen,
the world's leading publisher of Open Access books
Built by scientists, for scientists

6,300
Open access books available

171,000
International authors and editors

190M
Downloads

154
Countries delivered to

Our authors are among the

TOP 1%
most cited scientists

12.2%
Contributors from top 500 universities

CLARIVATE ANALYTICS
BOOK CITATION INDEX
INDEXED

WEB OF SCIENCE™

Selection of our books indexed in the Book Citation Index
in Web of Science™ Core Collection (BKCI)

Interested in publishing with us?
Contact book.department@intechopen.com

Numbers displayed above are based on latest data collected.
For more information visit www.intechopen.com

Chapter

Large Scale Simulations for Dust Acoustic Waves in Weakly Coupled Dusty Plasmas

Aamir Shahzad, Zamar Ahmed, Muhammad Kashif,
Amjad Sohail, Alina Manzoor, Fazeelat Hanif,
Rabia Waris and Sirag Ahmed

Abstract

Dust acoustic wave of three-dimensional (3D) dusty plasmas (DPs) has been computed using equilibrium molecular dynamics (EMD) simulations for plasma parameters of Coulomb coupling strength (Γ) and Debye screening (κ). New simulations of wave properties such as longitudinal current correlation (LCC) $C_L(k, t)$ function have been investigated for 3D weakly DPs (WCDPs), for the first time. EMD results, $C_L(k, t)$ have been simulated for four normalized wave numbers ($k = 0, 1, 2,$ and 3). Our simulations illustrate that the frequency and amplitude of oscillation vary with increasing of Γ and κ. Moreover, present simulations of $C_L(k, t)$ illustrate that the varying behavior has been observed for changing (Γ, κ) and system sizes (N). Current investigation illustrates that amplitude of wave oscillation increases with a decrease in Γ and N. However, there are slightly change in the value of $C_L(k, t)$ and its fluctuation increases with an increasing k. The obtained outcomes have found to be more acceptable than those that of previous numerical, theoretical, and experimental data. EMD simulation has been performed with an increasing sequence for WCDPs and it serves to benchmark improved approach for future energy generation applications.

Keywords: plasma, complex (dusty) plasma, wave properties, weakly coupled (dusty) plasma, current correlation function, equilibrium molecular dynamics simulation

1. Introduction

Nowadays, it has been seen complex liquids have attracted considerable interest for many researchers. Complex liquids have introduced themselves by emerging the technology of all processes. Different techniques such as experimental, theoretical, and simulation are used to study the behavior of the complex liquid. Unambiguous models have been used to describe physical properties for specific ranges of temperature and pressure. Explicit equations can also be used to calculate the thermophysical

properties of fluids when there is not any literature on complex fluids present. To study the behavior of complex fluids, information on thermophysical properties should be required. Transport properties of complex fluids play an essential role in laboratory and industrial applications. Moreover, thermophysical properties have played a very dominant role in optimization and system design. For the past few years, research on transport properties has occurred through several techniques such as experimental, theoretical, and simulation. Experimental research on transport properties has resulted in non-absolutely convergent expression because there is no accurate and precise experimental calculation of transport properties [1].

1.1 Plasma

Plasma makes up 99% of the matter in space and is referred to as the fourth state of matter. In essence, plasma is a sort of electrified gas in which atoms have split into positive ions and electrons. It is a type of matter in a variety of branches of physics, including astrophysics, technical plasma, and terrestrial plasma. Plasma is created artificially in a lab and used for a variety of technical applications, including fusion energy research, display, fluorescent lighting, and more. The term "plasma" was initially used by American scientist Irving Langmuir, who defined it as "a quasi-neutral gas of charged particles that exhibits collective behavior." When the number of ions equals the number of electrons ($n_i \approx n_e \approx n$), a gas is said to be "quasi-neutral," meaning it becomes electrically neutral. Where n is the number density, n_i is the ion density, and n_e is the electron density. The electric field and coulomb potential cause charged particles to collide when they exhibit collective behavior. The usage of plasma in research and technology is widespread. It is extremely important in daily life. Plasma is employed in many aspects of daily life, including lasers, sterilizing medical equipment, lightning, high-intensity beams, purifying water, and many more [2].

1.2 History of plasma

Plasma was initially defined in 1922 by American scientist Irving Langmuir, who was the only one to do so. Various academics began studying plasma physics in 1930 after being motivated by some particle puzzles. Hanes Alfven developed hydromagnetic waves in 1940; these waves are known as Alfven waves. He also mentioned that astrophysical plasma would be studied using these waves. Beginning around the same time in the Soviet Union, Britain, and the United States in 1950, research on magnetic fusion energy was initiated. The study of magnetic fusion energy was regarded as a subfield of thermonuclear power in 1958. This study was initially conducted under strict confidentiality, but after it became clear that the military did not appreciate controlled fusion research, the above-mentioned three countries made the research publicly available. Because of this, additional nations may take part in plasma-based fusion research. By the end of 1960, a Russian Tokomak configuration produces plasma with various plasma characteristics. Numerous sophisticated tokamaks that were created between 1970 and 1980 validated the effectiveness of the tokamak. Additionally, the Tokamak experiment nearly succeeded in achieving fusion break, and in 1990, work on DP physics started. When charged particles are absorbed by plasma, they split into four different components: electrons, ions, neutral particles, and dust particles and dust particles change plasma properties which are called as "Dusty plasma" [3].

1.3 Dusty plasma

When charged particles are submerged in plasma, the plasma properties become more complicated. This causes the plasma to be referred to as dusty plasma, which is also known as complex plasma. DP typically contains an extra charged particle and is electron-ion plasma. DPs contain dust particles of sizes ranging from tens of nanometers to hundreds of microns. The size of the particle is 3e-8g. This charged component can also be thought of as a micron-sized dust particle. Ice or metallic particles could make up dust particles. Different sizes and types of dust particles can be found throughout the universe and in the atmosphere. Although it typically takes the form of a solid, it can also be liquid or gaseous. The movement of ions and electrons can charge up dust particles. The electric potential of charged dust particles, which ranges from 1 to 10 V, is altered by the electric and magnetic fields. In a lab, dust particles can be grown. The existence of dust particles in plasma has exposed advanced fields for researchers and scientists. The majority of plasma in the universe is DP. It occurs frequently in the atmospheres of stars, the sun, planetary rings, galaxies, cosmic radiation, and the earth's magnetosphere and ionosphere. Based on the ordering of many radii and characteristic lengths between particles interacting (rd, λD), plasma with dust particles can be called either "dusty plasma" or "dust in plasma". If the $\lambda D > rd$ then it is called "dusty plasma" and if $\lambda D < rd$ then it is called "dust in plasma". Here, λD is dust particles' Debye length and rd is the interparticle distance. These are the conditions for DP [3, 4].

1.3.1 History of dusty plasma

Plasma is a very advanced field of science and technology. Many researchers have been motivated by their achievements in the field of science, medical field, and technology. In 1924, the term "plasma" first time defined by Irving Langmuir. Contemporary research on DP also has motivated many researchers and has become an interesting field of science and technology. In 1980, very exciting incident happened in the field of DP for the Saturn ring. In 1997, Mendis discovered a bright comet by a distant ancestor. The "distant ancestor" is an extraordinary comic laboratory for the investigation and study of interactions between dust particles and their physical and dynamic behaviors. Further manifestations of DPs were noctilucent clouds, origin nebula (which can be seen from the naked eye), zodiac light, etc. Images that are taken from the Saturn ring have shown that dust particles rotating around the Saturn ring have shape of spokes. The research from the last analysis has shown that these dust particles are fine particles. In 2000–2017, the present condition of DP is stable and is playing a main dominant role in science, industries, technology, energy sectors, and medical stores [5].

1.3.2 Charge on dust particle

Charging of dust grains can be drained through different processes involving the background plasma (electron and ion) being bombarded on surface of dust particles, secondary electron production, ion sputtering, photoelectronic emission by UV radiations, etc. Mostly, the charge on dust particles is negative in low-temperature laboratory plasma. When an electron from the background plasma strikes the surface of dust particle and is attached and lost from the plasma. Because electrons are more moveable than ions, the surface dust grain collects electrons, attracts ions, and repels

electrons until the state of immobility is attained. This charge is accountable for a long lifetime of particles and confinement in plasma [4]. Other collective phenomena and wave instabilities are created due to interactions between these particles.

1.4 Types of dusty plasma

Dusty plasma is classified by the Coulomb coupling parameter.

• Weakly coupled plasma

• Strongly coupled plasma

1.4.1 Weakly coupled plasma

Weakly coupled plasma (WCP) is described by Coulomb coupling parameter Γ. Plasma is referred to as WCP when the coupling parameter's value becomes negligible. Hot plasma is another name for WCP. Plasma is referred to be hot plasma or ideal plasma when the temperature of the electron reaches the same level as the temperature of the ion (Te ≅Ti). In a laboratory discharge tube with high gas pressure, hot plasma is produced. The flame, atmospheric arcs, and sparks are examples of hot plasma. WCDP lacks a defined shape due to the extremely weak interactions between interacting particles at high temperatures and low densities. The EMD simulation has been used to examine the occurrence of diffusion motion in WCDPs [6].

1.4.2 Strongly coupled plasma

Strongly coupled plasma (SCP) is defined by the Yukawa potential, also known as the screened coulomb coupling potential (Γ). Coulomb coupling potential (Γ) is the ratio of potential energy to kinetic energy. Whenever potential energy exceeds unity, then kinetic energy becomes as Γ > 1. Its mean SCP is also defined as cold plasma since potential energy increases from inter-particle kinetic energy and plasma particles change into crystalline form. Cold plasma is used for teeth sterilization and food processing. Charged particles in SCP are influenced by the electric field, but the influence of the magnetic field is ignored for this kind of cold plasma.

1.5 Formation of dusty plasma in the laboratory

Different methods have been expanded for the production of DP in laboratories. Modified Q machines, rf discharges, and dc discharges are different methods that have been used in the last few years. Modified Q machine is single-ended machine used for the production of DP which allows the dust grains to dispersion over a cylindrical plasma column portion. In dc neon glow discharge stratum, DP is produced by a micron-sized dust particle. The discharge is created with cold electrodes in cylindrical glass tube. The distance between electrodes is 40 cm. The neon pressure is varied from 0.2 to 1 Torr and the fluctuation of the discharge current is 0.4–2.5 mA. DP is restrained in a cylindrical symmetric rf plasma system. The system of rf discharges consists of grounded electrodes, hollow outer electrode capacitive coupled to a 14 MHz rf power amplifier, and glass window. Man-made DP or DP generated in laboratory is dust in fusion devices, rocket exhaust, dust in space stations, dust precipitators, and thermonuclear fireballs. Other applications of DP are microelectronics

fabrications; plasma enhanced chemical vapor deposition (PECVD), flat panel displays, solar cells, semiconductor chips, dusty plasma devices (DPDs) are used to produce DP in the laboratory. Ordinary flames, flame of candlelight, strong passion, fire, and blaze produced by burning gas are basically weakly ionized plasma that contains dust particles. Thermionic electron emission of 10 nm dust particles increases the degree of ionization in ordinary hydrocarbon flames. DP also contains volcanos and charged snow [7].

1.6 Acoustic modes

Acoustic modes are categorized into two different types such as collision-less, uniform, and unmagnetized dusty plasma. These are dust acoustic (DA) and ion-acoustic (IA) waves.

1.6.1 Dust acoustic (DA) wave

Dust Acoustic Wave (DAW) is a low-frequency type of longitudinal wave. Basically, DAW is a sound wave when it travels through complex fluid which causes the oscillation between charged particles. The mass of dust particles is considered very important because it provides inertia which is used to sustain DAW, pressure of ions and electrons affords the restoring force. The dust acoustic wave is examined in DP and presented the dispersion relation using the Boltzmann distribution of ion and electron density [8].

1.6.2 Ion acoustic (IA) wave

The propagation of sound waves in ordinary gas is absurd due to the absence of collision between particles. Thus, in ionized gas, there is no possibility of the occurrence of sound waves due to the absence of collision. However, in the case of plasma, ions can transmit vibrations to each other due to their charges. IA wave is a constant velocity wave. The occurrence of IA wave depends upon the thermal motion of ions. It is a longitudinal wave in magnetized plasma. It demonstrates reflection, diffraction, and interference phenomena. The phase velocity of electron thermal speed is much greater than the IA wave. Particle displacement, particle velocity, sound intensity, and sound pressure are essential quantities of IA waves.

2. Models and numerical simulations

Interactions of the dust particle are studied by many mathematical models such as "in the center of potential well and repulsion potential, in rigid sphere". There are a number of interaction potentials for the calculations of complex systems for instance DP. However, in the best of accurate experimental and theoretical balance, the Yukawa potential is more favorable interaction potential for WCDPs and is also used in many other physical systems (for instance, medicine and biology systems, chemicals, astrophysics environmental and physics of polymers, etc.) [9]. For charged particles, Yukawa potential has the following form [5]:

$$\phi(|r|) = \frac{Q^2}{4\pi\varepsilon_o} \frac{e^{\frac{-|r|}{\lambda_D}}}{|r|} \tag{1}$$

In the above equation, r represents inter-particle distance, Debye screening length is represented by λ_D, the permittivity of free space is represented by ε_0, and charge on dust particle is represented by Q. System particle is expressed by plasma parameters. Coulomb coupling strength (Γ) is defined as the potential energy of interaction between particles and the average kinetic energy of the particles. The Γ defines the distribution of plasma. Γ is given in this form of:

$$\Gamma = \left(\frac{Q^2}{4\pi\varepsilon_o} \frac{1}{a_{WS}k_B T} \right) \tag{2}$$

In Eq. (2), T is absolute temperature, k_B is Boltzmann constant, and a_{ws} represents Wigner Seitz (*WS*) radius and its value is $(3/4\pi n)^{1/3}$ with n representing number density ($n = N/V$) of dust particle. There is another parameter, k equal to $2\pi/L$ which affects the system of WCDPs. Where L represents the computational box length and $k^* = 2a_{ws}\pi/L$ is the normalized value of k. The $F_i = \sum_j F_{ij}$ is the force experienced on all dust particles. The force on *ith* particle is exerted by other particles. Debye screening strength is the ratio of the interparticle distance a (Wigner Seitz radius) to the Debye length λ_D [3, 5, 7, 10]. The value of κ can be represented in this form:

$$\kappa = \frac{a}{\lambda_D} \tag{3}$$

In this part, the EMD simulation is reported of $C_L(k, t)$ of WCDP for large domain of plasma parameter of ($0.9 \leq \Gamma \leq 0.1$) and ($1 \leq \kappa \leq 3$) along with the varying value of wave number ($k = 0, 1, 2$ and 3). The accuracy and correctness of our proposed model for DAWs $C_L(k, t)$ is checked with different system sizes ($N = 500, 2048$, and 4000).

For the system of 3D Yukawa system, time scales in WCDP are categorized by the inverse of plasma frequency as (ω_p^{-1}) [1].

$$\omega_p^{-1} = \left(\frac{nQ_d^2}{\varepsilon_o m} \right)^{\frac{-1}{2}} \tag{4}$$

In Eq. (4), dust particle mass and number density are represented by m and n. In EMD simulation, the number of particles is $N = 500$ to 4000 (the system size will be increased on the validity of computational power) placed in computational box.

2.1 Current correlation function

Local density provides information about the distribution of atoms. It is possible to study the local variations in motion of atoms. The momentum and particle current for single atomic particles are calculated by molecular dynamics simulation [9].

$$\pi(r, t) = \sum_j v_j \delta(r - r_j(t)) \tag{5}$$

With Fourier transformation

$$\pi(r, t) = \sum_j v_j e^{-ik.r_j(t)} \tag{6}$$

Fourier transform equation is used to measure the LCC function.

$$C_{\alpha\beta}(k, t) = \frac{k^2}{N_m} \left(\pi_\alpha(k, \ t) \pi_\beta(-k, \ 0) \right) \tag{7}$$

In Eq. (7), k is the wave vector. The equation given above can also be stated in form of the longitudinal and transverse current correlation function.

$$C_{\alpha\beta}(k, t) = \frac{k_\alpha k_\beta}{k^2} C_L(k, t) + \left(\delta_{\alpha\beta} - \frac{k_\alpha k_\beta}{k^2} \right) C_L(k, t) \tag{8}$$

Longitudinal and transverse current functions are acquired in X, Y, and Z directions by locating k are equal to $k\hat{z}$.

2.2 Normalized longitudinal current correlation function C_L (k, t)

Fourier transformation is used to write Eq. (7) into LCC functions which are normalized

$$C_L(k, t) = \frac{k^2}{N^m} \langle \pi_Z(k, \ t)\pi_Z(-k, \ \ 0) \rangle \tag{9}$$

By putting π_z value in Eq. (9), we obtain

$$C_L(k, t) = \frac{k^2}{N^m} \left\langle \sum v_j e^{-ik.Z_j(t)}(k, \ t) \sum v_j e^{-ik.Z}(k, \ t) \right\rangle \tag{10}$$

Eq. (10) explains charge particle transports in longitudinal motion. Longitudinal current correlation function describes that wave is propagating in negative and positive directions of the Z-axis.

2.3 Parameters and simulation techniques

This segment shows that system contains N = 500–4000 particles. Yukawa potential causes the interaction between these numbers of particles which is shown in Eq. (1) and contain in the cubic region. Moreover, this segment illustrates an overview of results attained through EMD simulation for longitudinal current correlation function which is shown in Eq. (10). The simulation takes place in simulation box and the simulation box dimension is selected as L_X, L_Y, and L_Z. In our case, we have used the EMD simulation to calculate the longitudinal current correlation function for N = 500 number of particles at plasma coupling parameter Γ = (0.1–0.9) with κ = (1.4, 2.0 and 3.0) at four varying values of wave numbers k = (0, 1, 2 and 3). The EMD simulation has been used to investigate shear viscosity and dynamical structure S(k,ω) of SCDPs [5, 7, 10–12].

3. EMD simulation results

3.1 Time-dependent longitudinal current correlation function $C_L(k, t)$, at $\kappa = 1.4$
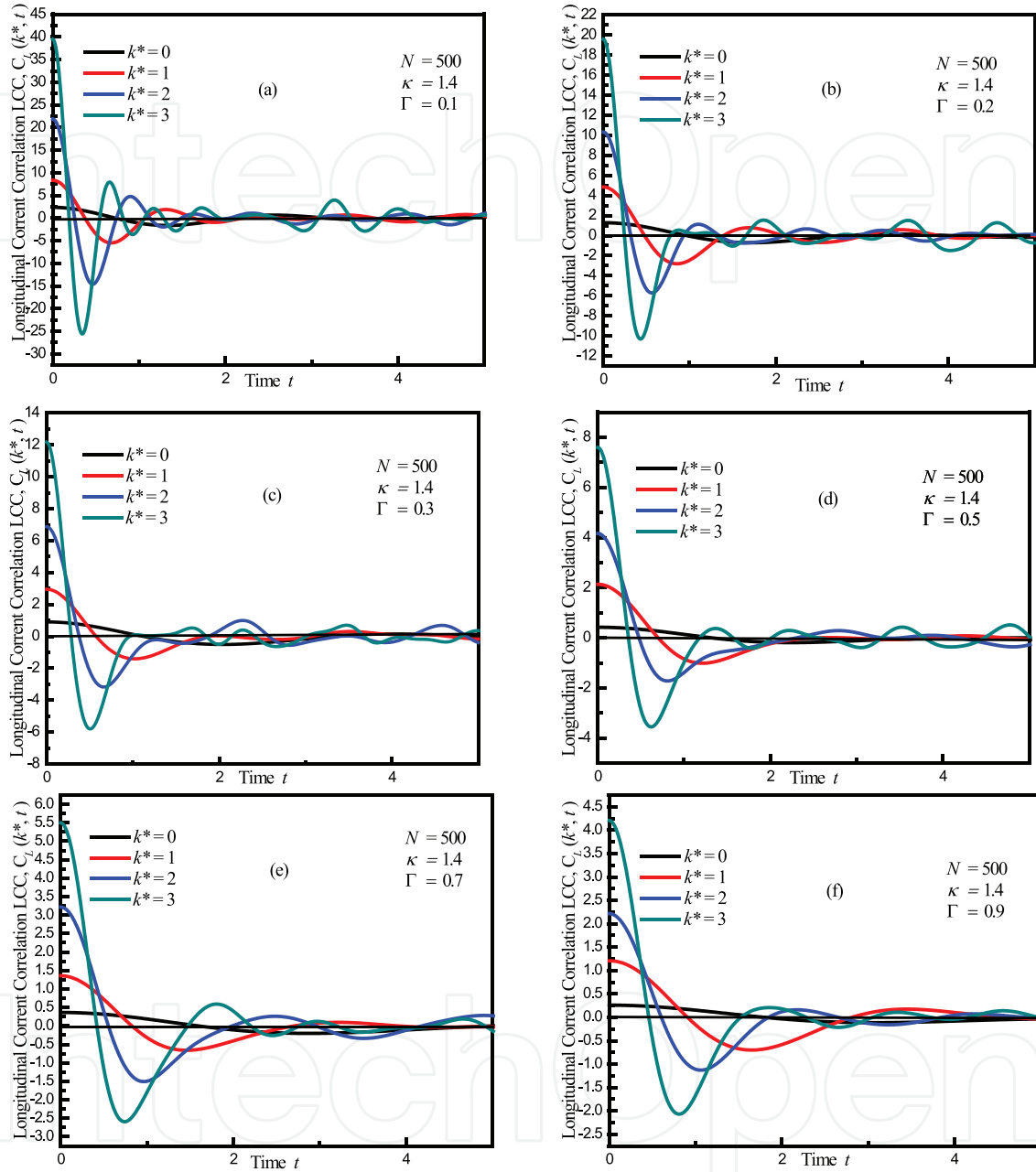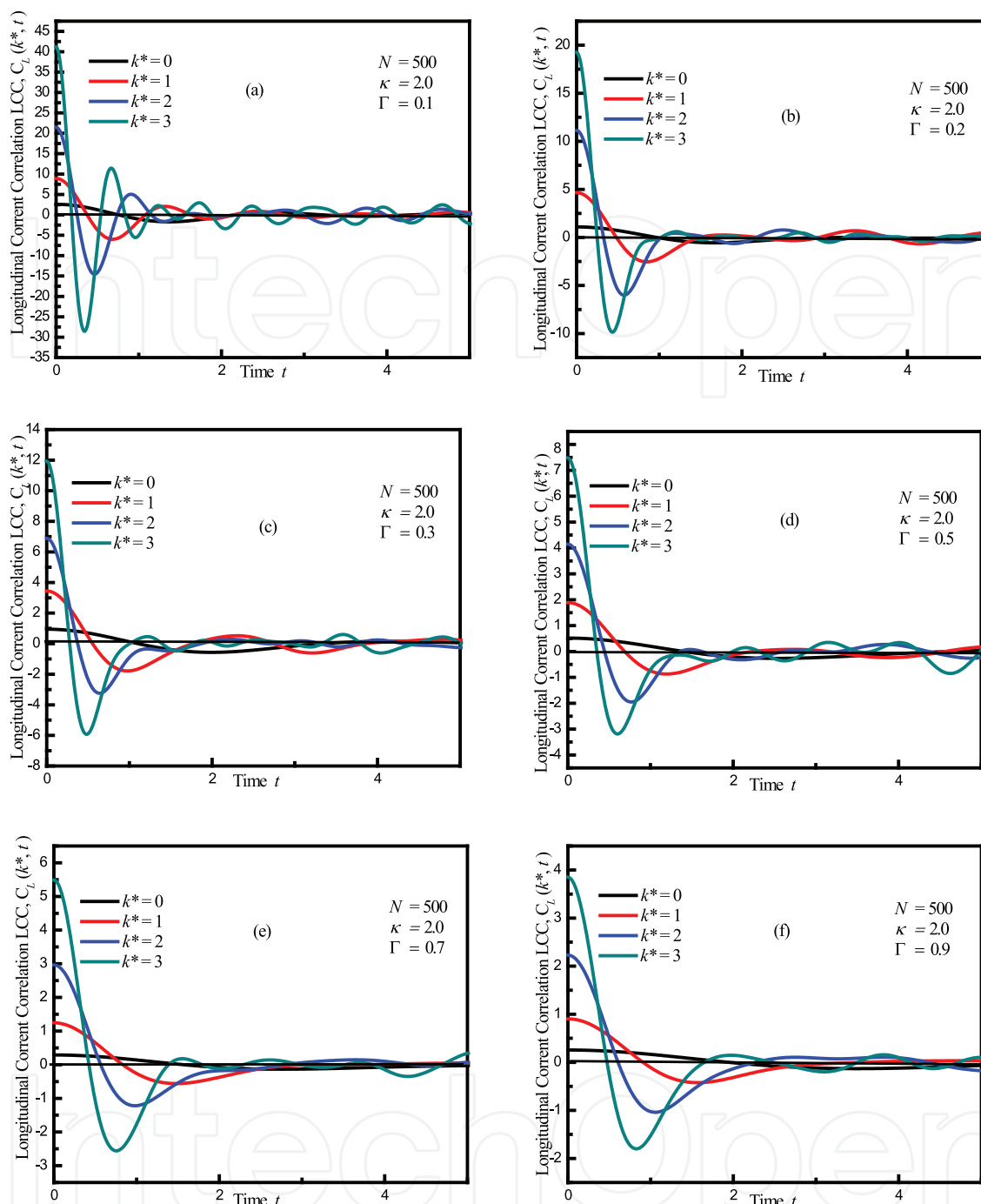

Figure 1.
The fluctuation of C_L (k, t) as function of time of WCDP at system size N = 500, κ = 1.4, wave numbers (k = 0, 1, 2 and 3) for six different plasma parameters (a) Γ = 0.1, (b) Γ = 0.2, (c) Γ = 0.3, (d) Γ = 0.5, (e) Γ = 0.7, and (f) Γ = 0.9.

3.2 Time-dependent longitudinal current correlation function $C_L(k, t)$, at $\kappa = 2.0$

Computational results using EMD simulation have shown in **Figures 1** and **2** for weakly coupled Yukawa system LCC, $C_L(k, t)$ as a function of time at κ (= 1.4, 2.0 and 3.0) for six different values of Γ (= 0.1, 0.2, 0.3, 0.5, 0.7 and 0.9) and size of system is N=500 and four values of wavenumbers k (= 0, 1, 2 and 3) which are normalized. **Figures 1** and **2** explain main results for every three different values of

Figure 2.
The fluctuation of C_L (k, t) as function of time of WCDP at system size N = 500, κ = 2.0, *wave numbers (*k = 0, 1, 2 and 3*) for six different plasma parameters (a) Γ = 0.1, (b) Γ = 0.2, (c) Γ = 0.3, (d) Γ = 0.5, (e) Γ = 0.7, and (f) Γ = 0.9.*

the Debye screening parameter ($κ$ = 1.4, 2.0, 3.0) of 3D Yukawa complex liquids. It is obtained from six panels of **Figure 1** that the amplitude and wavelength of LCC CL (k, t) increase with decrease of Γ (0.9–0.1). It is also obtained that by increasing wave numbers k (0, 1, 2, and 3), the amplitude of longitudinal current increases. It is noted that the CL (k, t) value for k = 2 and 3 shows maximum sinusoidal wave behavior at lower value of Γ from **Figures 1a–d** and **2a–c**. The sinusoidal wave behavior decreases with an increase of Γ and damping of the wave increases with an increase of time and Γ.

4. Summaries

Time-dependent LCC function, $C_L(k, t)$ has been studied for weakly coupled Yukawa system through EMD simulation over a wider range of plasma parameters ($0.9 \leq \Gamma \leq 0.1$), and ($1.4 \leq \kappa \leq 3.0$) along with varying wave numbers values ($k = 0$, 1, 2, 3). The behavior of the Weakly Coupled Yukawa system using EMD simulation has not been studied yet. It is observed that the amplitude and frequency $C_L(k, t)$ of wave of oscillation increase when the value of Γ (0.9–0.1) decreases. $C_L(k, t)$ value also increases when wave number k increases. The amplitude of $C_L(k, t)$ steadily decreases with an increase in the number of particles N. It is implied that the presented simulation is based on Yukawa potential which has been employed to investigate the propagation of waves in WCDP. The presented simulation provides a great understanding of the propagation of the wave in WCDP. The employed simulation affords further respectable data for propagation in WCDP. It has been observed from these simulations that waves are repeatedly propagated at intermediate and higher values of Γ. The frequency and amplitude of waves are examined at different mode of waves.

Acknowledgements

Abbreviations

EMD	equilibrium molecular dynamics
Γ	Coulomb coupling
κ	Debye screening strength
MD	molecular dynamics
PBCs	periodic boundary conditions
$C_L(k, t)$	longitudinal current correlation function
DP	dusty plasma
EMD	equilibrium MD
LCC	longitudinal current correlation
k	wave number
WCDPs	weakly coupled dusty plasmas
WCP	weakly coupled plasma
SCP	strongly coupled plasma
DA	dust acoustic
IA	ion acoustic
DAW	DUST ACOUSTIC WAVE

Author details

Aamir Shahzad*, Zamar Ahmed, Muhammad Kashif, Amjad Sohail, Alina Manzoor, Fazeelat Hanif, Rabia Waris and Sirag Ahmed
Modeling and Simulation Laboratory, Department of Physics, Government College University Faisalabad (GCUF), Faisalabad, Pakistan

*Address all correspondence to: aamirshahzad_8@hotmail.com; aamir.awan@gcuf.edu.pk

IntechOpen

References

[1] Shahzad A, He MG. Thermal conductivity calculation of complex (dusty) plasmas. Physics of Plasmas. 2012;**19**(8):083707

[2] Chen FF. Introduction to Plasma Physics and Controlled Fusion. New York: Plenum Press; 1984. pp. 19-51

[3] Bellan PM. Fundamentals of Plasma Physics. New York, US: Cambridge University Press; 2008

[4] Rodriguez IJ. Some Assembly Required: Computational Simulations of Dusty Plasma. Portland, US: Portland State University; 2018. p. 622

[5] Shahzad A, Shakoori MA, Mao-Gang HE, Feng Y. Numerical Approach to Dynamical Structure Factor of Dusty Plasmas: Plasma Science and Technology-Basic Fundamentals and Modern Applications. Croatia/London, UK: INTECH Publisher; 2019

[6] Shahzad A, He M, Nikitin M. Thermal conductivity and non-newtonian behavior of complex plasma liquids. In: Thermoelectrics for Power Generation-A Look at Trends in the Technology. Rijeka: InTech; 2016

[7] Shukla PK, Mamun AA. Introduction to Dusty Plasma Physics. Florida, US: CRC Press; 2015

[8] Shukla PK. Twisted dust acoustic waves in dusty plasmas. Physics of Plasmas. 2012;**19**(8):083704

[9] Rapaport DC. The Art of Molecular Dynamics Simulation. New York, US: Cambridge University Press; 2004

[10] Shahzad A, He MG. Thermal conductivity of three-dimensional Yukawa liquids (Dusty Plasmas). Contributions to Plasma Physics. 2012; **52**(8):667-675

[11] Merlino R. Dusty plasma physics: Basic theory and experiments. Summer College on Plasma Physics. 2007;**30**: 1-130

[12] Xu W, Song B, Merlino RL, D'Angelo N. A dusty plasma device for producing extended, steady state, magnetized, dusty plasma columns. Review of Scientific Instruments. 1992; **63**(11):5266-5269

We are IntechOpen,
the world's leading publisher of
Open Access books
Built by scientists, for scientists

6,300
Open access books available

171,000
International authors and editors

190M
Downloads

154
Countries delivered to

Our authors are among the

TOP 1%
most cited scientists

12.2%
Contributors from top 500 universities

BOOK CITATION INDEX
CLARIVATE ANALYTICS
INDEXED

WEB OF SCIENCE™

Selection of our books indexed in the Book Citation Index
in Web of Science™ Core Collection (BKCI)

Interested in publishing with us?
Contact book.department@intechopen.com

Numbers displayed above are based on latest data collected.
For more information visit www.intechopen.com

Chapter

Future Particle Accelerators

Javier Resta López

Abstract

Particle accelerators have enabled forefront research in high energy physics and other research areas for more than half a century. Accelerators have directly contributed to 26 Nobel Prizes in Physics since 1939 as well as another 20 Nobel Prizes in Chemistry, Medicine and Physics with X-rays. Although high energy physics has been the main driving force for the development of the particle accelerators, accelerator facilities have continually been expanding applications in many areas of research and technology. For instance, active areas of accelerator applications include radiotherapy to treat cancer, production of short-lived medical isotopes, synchrotron light sources, free-electron lasers, beam lithography for microcircuits, thin-film technology and radiation processing of food. Currently, the largest and most powerful accelerator is the Large Hadron Collider (LHC) at CERN, which accelerates protons to multi-TeV energies in a 27 km high-vacuum ring. To go beyond the maximum capabilities of the LHC, the next generation of circular and linear particle colliders under consideration, based on radiofrequency acceleration, will require multi-billion investment, kilometric infrastructure and massive power consumption. These factors pose serious challenges in an increasingly resource-limited world. Therefore, it is important to look for alternative and sustainable acceleration techniques. This chapter pays special attention to novel accelerator techniques to overcome present acceleration limitations towards more compact and cost-effective long-term future accelerators.

Keywords: high energy collider, Plasma wakefield, dielectric accelerator, solid-state plasma, plasmonic accelerator

1. Introduction

Currently, there are more than 30,000 particle accelerators in operation around the world, with a strong impact on science, industry and economy. Although, historically high energy physics (HEP) has been the main driving force for the accelerator R&D, only 1% of particle accelerators worldwide are used for research purposes, the rest are mostly used to support commercial, industrial and medical work. For instance, active areas of accelerator applications include radiotherapy to treat cancer, production of short-lived medical isotopes, synchrotron light sources, free-electron lasers, beam lithography for microcircuits, thin-film technology and radiation processing of food.

Since the pioneering work by Gustave Ising, Rolf Wideröe, Ernest Lawrence and many others in the 1920s and 1930s, the accelerator technology has progressed immensely [1]. Particularly, during the past 70 years, an impressive development of high energy colliders, with ever-increasing luminosities and centre-of-mass energies,

has resulted in a number of fundamental discoveries in particle physics. In recent decades, experiments at hadron colliders, such as the Super Proton Synchrotron (SPS) and Tevatron, at e^+e^- colliders, such as the Large Electron-Positron Collider (LEP) and the Stanford Linear Collider (SLC), and at the electron-proton collider HERA (Hadron-Electron Ring Accelerator) have explored the energy range up to several 100 GeV and established beyond doubt the validity of the Standard Model in this range of energies [2]. In this tremendous progress, the development and optimisation of the radiofrequency (RF) technology has played a key role. Nowadays, most particle accelerators are driven by RF electromagnetic fields. Currently, the largest and most powerful RF-driven accelerator in operation is the Large Hadron Collider (LHC) at CERN [3], which accelerates protons to multi-TeV energies in a 27 km high-vacuum ring. Its kilometric size and complexity have earned it the name of the 'Cathedral' of the particle physics. With the discovery of the Higgs boson in 2012, the LHC has contributed to complete the Standard Model [4, 5].

To go beyond the maximum energy capabilities of the LHC, the next generation of RF-driven colliders under consideration would be among the largest and most complex facilities built on Earth, requiring intensive R&D and multi-billion Euro investments. For instance, the long-term goal of the Future Circular Collider (FCC) study hosted by CERN [6, 7] is the design and construction of a 100 TeV hadron collider in a 100 km long tunnel. Furthermore, future linear e^+e^- colliders based on RF technology, such as the International Linear Collider (ILC) [8] or the Compact Linear Collider (CLIC) [9], are designed to produce acceleration gradients of between 30 MV/m (ILC) and 150 MV/m (CLIC, 30 GHz frequency operation mode). These machines must, therefore, be tens of kilometres long to reach the desired beam energies, 125 GeV (ILC) and 1.5 TeV (CLIC). Another big project proposed by the HEP community is a high luminosity multi-TeV muon collider [10]. However, practically all the projects mentioned above, based on conventional RF acceleration technology, present serious challenges in terms of size and cost per GeV of beam energy. They need large-scale infrastructure (10–100 km scale) and, in most cases, a billion investment. To afford such a cost, it usually requires a consortium of several countries. Another key challenge is the sustainability in terms of the AC wall plug power consumption. High energy colliders are really 'hungry energy' machines that require hundreds of MW AC wall power to operate. To reduce such a power consumption in the latest years there have been a trend towards more 'green accelerators'. This concept includes the investigation of different ways to reduce energy consumption. For instance, through the improvement of the efficiency of existing technologies, e.g., increasing the efficiency of klystrons [11]. Also the design of Energy-Recovery Linacs (ERLs) can be considered as part of the R&D effort aimed at increasing energy efficiency [12].

To tackle the limitations of conventional accelerators, nowadays there is also an intensive R&D program on novel advanced concepts, some of which will be briefly described in the next sections. These alternative acceleration techniques might define the long-term future of particle accelerators, thus transforming the current paradigm in collider development towards more sustainable, compact and low-cost machines. For a more exhaustive review of past, present and future accelerators and colliders, see for example Refs. [2, 13, 14].

2. Plasma wakefield

Since the 1930s the RF acceleration technology has practically dictated the development of high energy colliders. Their power, cost and size have evolved with the
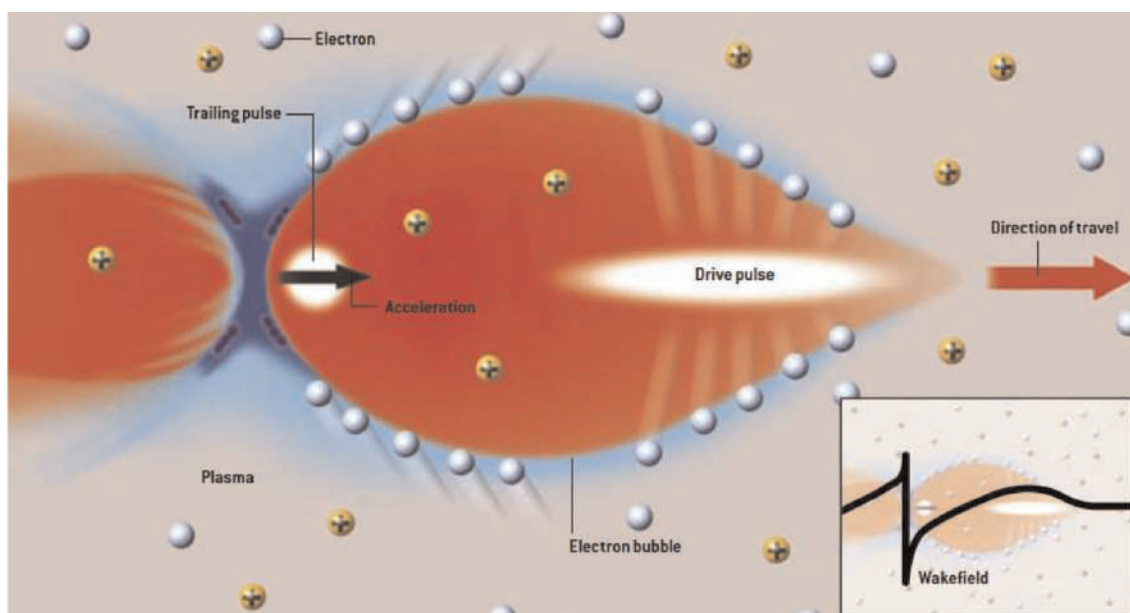
Figure 1.
Conceptual drawing of a plasma wakefield accelerator [17]. A drive pulse, either an intense laser (laser-driven) or a short electron bunch (beam driven) crossing a plasma, pushes away electrons. The much heavier ions are left behind. This charge separation makes a very large electric field. As the electrons rush back to their original position they overshoot forming a plasma wave, which induces a strong electric field behind the driver (wakefield). If a trailing charged particle pulse is positioned at the right spot seeing the right longitudinal wakefield phase behind the driver, it can be accelerated.

continuous improvements and optimisation experienced by RF cavities. However, over the recent decades, it has become apparent that RF technology is reaching its limits in terms of achievable accelerating gradients. Currently, the maximum electro-magnetic fields that it can support are limited to approximately 100 MV/m due to surface breakdown [15]. To overcome this limit, Tajima and Dawson [16] proposed an alternative solution, a plasma accelerator based on laser-driven wakefields. Since plasma[1] is already a broken-down medium, there is no breakdown limit, compared to the conventional metallic RF cavities.

In general terms, the concept of Plasma Wakefield Acceleration (PWFA) is illustrated in **Figure 1**. A drive pulse enters the plasma and expels the electrons of the plasma outward. The plasma ions move a negligible amount due to their higher mass with respect to the electrons. In consequence, a positively charged ion channel is formed along the path of the drive pulse. The drive pulse can be either a short laser pulse (Laser Wakefield Acceleration [LWFA]) [16] or an electron bunch PWFA [18]. After the passage of the driver (laser or particle beam), the plasma electrons rush back in, attracted by the transverse restoring force of the ion channel. In this way a space charge-driven oscillation is excited, generating alternating regions of negative and positive charge, thus inducing a strong longitudinal electric field behind the driver, the so-called plasma wakefield. Therefore, if a witness charged particle bunch is injected behind the driver at the correct distance and phase, then it will be accelerated with high gradients, in some cases exceeding 100 GV/m.

In the last decades, acceleration of relativistic electrons in gaseous plasma has been successfully demonstrated in several experiments, see for example [19–21]. In the same way, PWFA of positrons has also been demonstrated [22–24]. Furthermore, the

---

[1] A plasma is defined as a fluid of positive and negative charges.

Advanced Wakefield Experiment (AWAKE) at CERN has recently shown that 10–20 MeV electrons can be accelerated to GeV energies in a plasma wakefield driven by a highly relativistic self-modulated proton bunch [25].

Previously, we have mentioned injection of a witness beam to be accelerated by the induced wakefield. In addition, internal injection of electrons from the plasma itself is also possible in the so-called 'bubble regime' [26–28].

The wakefields generated in plasma can be evaluated by analytical expressions [29]. The maximum accelerating field in a plasma accelerator can be estimated as follows:

$$E_z[\text{V/m}] \approx 96\sqrt{n_e[\text{cm}^{-3}]} \tag{1}$$

where n_e is the electron density in the plasma. This density determines the plasma frequency, $\omega_p = \sqrt{e^2 n_e/m_e \varepsilon_0}$, with m_e and e the electron rest mass and charge, respectively, and ε_0 the electrical permittivity of free space. For example, a typical plasma density $n_e = 10^{18}$ cm^{-3} gives $E_z \sim 100$ GV/m, that is, approximately three orders of magnitude higher than the maximum gradient obtained in RF structures.

Multi-TeV e^+e^- concepts based on staged plasma cells have been proposed [30–32], see **Figure 2**. However, one of the main drawbacks of plasma accelerators is the production of relatively poorer beam quality (higher energy spread and transverse size) with respect to conventional RF techniques. In order to tackle this problem and produce a reliable and competitive plasma-based accelerator technology, a big research consortium, EuPRAXIA, was recently established [33]. A comprehensive
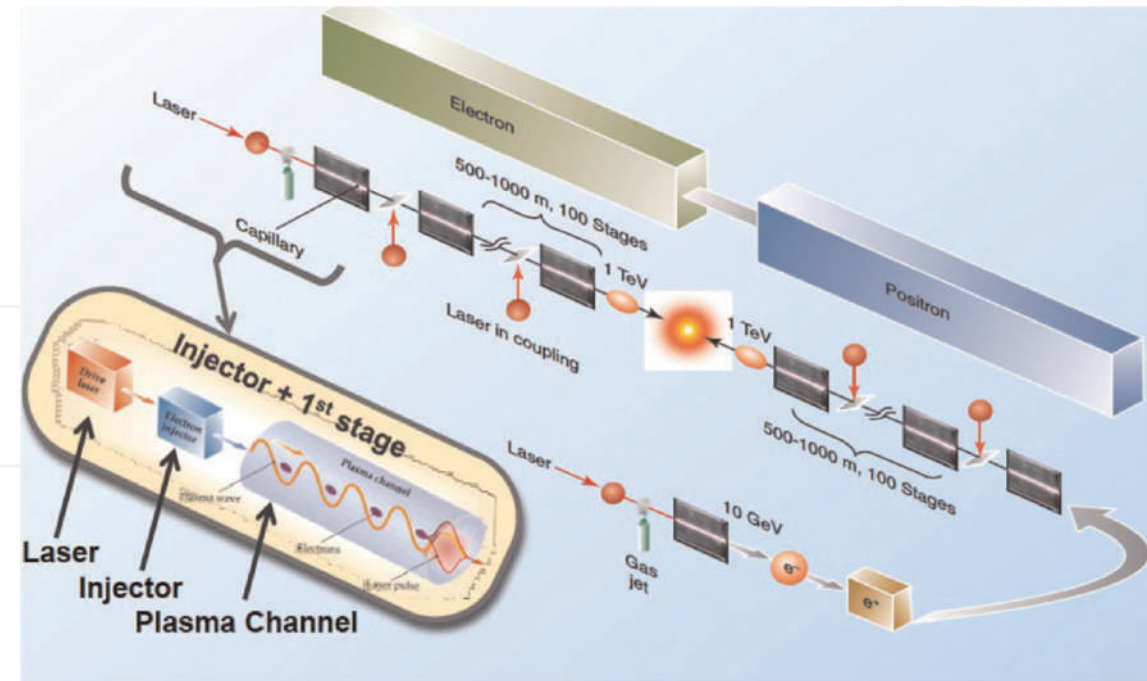

Figure 2.
Conceptual design of an LWFA-based linear collider. Both the electron and positron linacs consist of a sequence of plasma cells instead of RF cavities. The first stage consists of a plasma-based injection-acceleration module where controlled injection techniques are applied to produce a high-quality electron beam with approximately 10 GeV energy. Electrons are then accelerated to 1 TeV using 100 laser-plasma modules, each consisting of a 1 m long preformed plasma channel driven by a 30 J laser pulse giving a 10 GeV energy gain. A fresh laser pulse is injected into each module. Similarly, positrons are produced from a 10 GeV electron beam through pair creation and then trapped and accelerated in a laser-plasma acceleration module to approximately 10 GeV. Subsequent laser-plasma modules would accelerate positrons to 1 TeV [32].

review of near and long-term potential applications of plasma accelerators can be found in Ref. [34].

3. Solid-state-based acceleration

To go beyond the state-of-the-art, solid-state materials might offer new paths for beam manipulation and acceleration. For example, in the field of accelerator physics, the channelling properties of silicon crystals have successfully been used for collimation and extraction of relativistic proton beams [35]. Could also solids provide an alternative medium for acceleration? Depending on their particular atomic configuration and electrical conduction nature, some solid-state micro- and nano-sized structures offer interesting properties to enhance electric field components or induce strong wakefields that could be useful for acceleration, as well as transverse particle guiding and radiation emission. Next, we review some promising concepts that could revolutionise the future generation of accelerators and light sources.

3.1 Dielectric wakefield acceleration

Since the achievable peak field in the conventional RF metallic cavities is limited by surface breakdown, one obvious way to overcome this limit is through the use of materials with better breakdown properties, such as some dielectric materials (e.g., diamond, quartz, silica and ceramics). **Figure 3** illustrates the concept of beam-driven Dielectric Wakefield Acceleration (DWA) [36]. In this case, the dielectric accelerator consists of a hollow channel covered by a layer of a dielectric material and a metallic cladding. The electric field from the driver polarises the atoms of the dielectric medium, which coherently generates high frequency electromagnetic radiation.

Alternatively, lasers can be used as a driving source. Dielectric laser-driven acceleration (DLA) has been demonstrated for both non-relativistic [37] and relativistic electrons [38, 39] and has made enormous progress in recent years. DLA is the method behind the famous concept of 'accelerator on a chip' [40, 41]. DLA and DWA are limited to a maximum gradient of approximately 10 GV/m in the THz frequency range. **Figure 4** shows a particular dual-grating DLA configuration with sub-micron aperture.
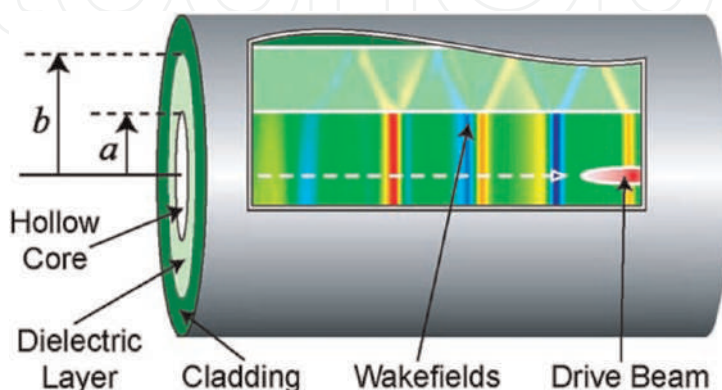

Figure 3.
Conceptual drawing of DWA [36]. A drive beam crosses a dielectric tube of radius "a"and excites wakefields. If a trailing beam is injected with the correct phase-space parameters, then it would be accelerated by the longitudinal component of the electric wakefield (bands of colour).
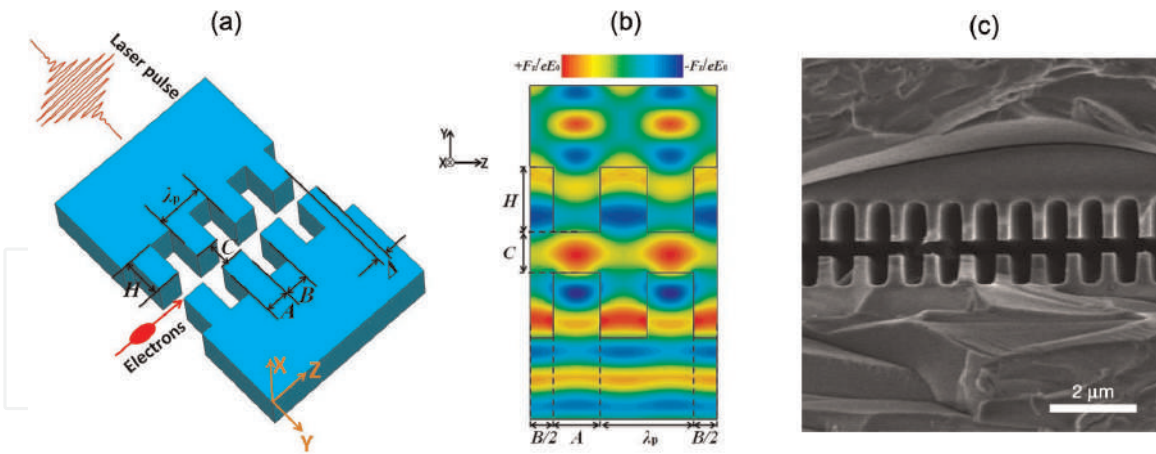
Figure 4.
(a) Conceptual scheme of a dual-grating scheme of DLA. (b) Simulation of the longitudinal accelerating force in a dual-grating structure illuminated by an input laser field along the y-axis [42]. (c) Scanning electron microscope image of the longitudinal cross-section of a DLA dual grating structure with 400 nm gap [38].

Usually, the dielectric structures have sub-mm dimensions, and there have been conceptual proposals to build a high-energy collider based on staged dielectric structures (**Figure 5**). This would allow 'table-top' high energy accelerators.

3.2 Crystal channelling acceleration

Semiconductor and metallic crystalline lattices have been proposed to generate a solid-state plasma medium to guide and accelerate positive particles, taking advantage of the channelling properties in crystals. High electron density in solids could be obtained from the conduction bands. Typical electron densities (n_e) in solid-state plasmas lie within the range of 10^{19} cm$^{-3} \leq n_e \leq 10^{24}$ cm^{-3} [43, 44], that is, between one and six orders of magnitude higher than the density in gaseous plasmas. Taking into account Eq. (1), solid-state-based plasmas might lead to accelerating gradients 0.1 TV/m$\lesssim E_z \lesssim 100$ TV/m.

Solid-state wakefield acceleration using crystals was proposed in the 1980s and 1990s by T. Tajima and others [43, 45, 46] as a technique to sustain TV/m acceleration
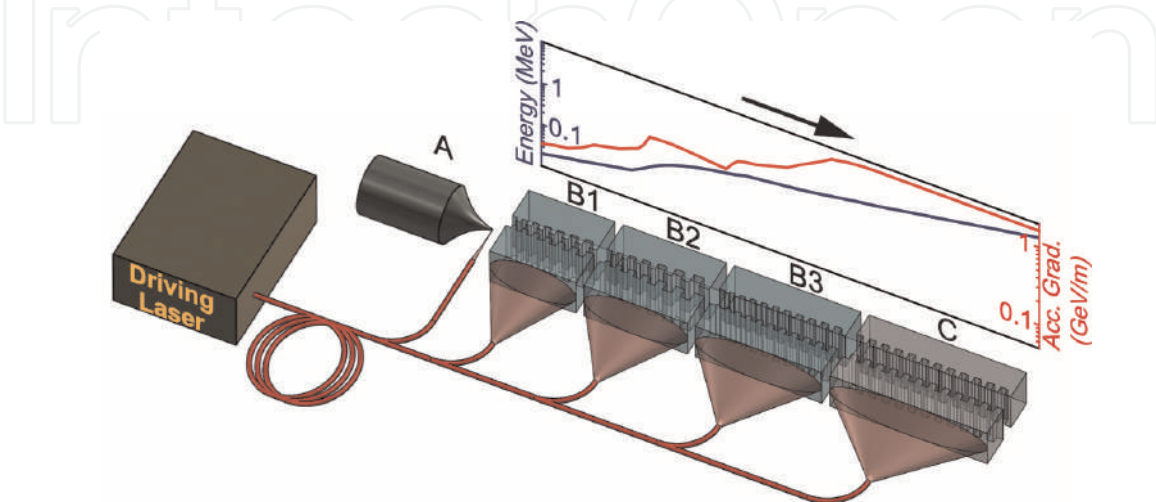

Figure 5.
Conceptual design of a staged DLA collider, consisting of dielectric structures with a tapered grating period to guarantee synchronicity with the accelerating electrons [37].

gradients. In the original Tajima's concept [45], high energy ($\simeq 40$ keV) X-rays are injected into a crystalline lattice at the Bragg angle to cause the Borrmann-Campbell effect [47, 48], yielding slow-wave accelerating fields. Then a witness beam of charged particles, e.g., muons, which is injected into the crystal with an optimal injection angle for channelling, can experience acceleration along the crystal axis.

Wakefields in crystals can be induced by means of the excitation of high-frequency collective motion of conduction electrons through the crystalline lattice (see next section on plasmonic acceleration). To reach accelerating gradients on the order of TV/m, crystals must be excited by ultrashort X-ray laser pulses within a power range of TW– PW, which makes the practical realisation of the concept very challenging. It has only recently become a realistic possibility since the invention of the so-called single-cycled optical laser compression technique by G. Mourou et al. [49, 50].

If natural crystals (e.g., silicon) are used for solid-state wakefield acceleration, the beam intensity acceptance is significantly limited by the angstrom-size channels. In addition, such small size channels increase the dechannelling rate and make the channels physically vulnerable to high energy interactions, thus increasing the damage probability by high power beams.

Over the past decade, there have been great advances in nanofabrication techniques [51–53] that could offer an excellent way to overcome many of the limitations of natural crystals. Metallic nanostructures and metamaterials [54, 55] could lead to suitable ultra-dense plasma media for wakefield acceleration or charged particle beam manipulation, that is, channelling, bending, wiggling, etc. This also includes the possibility of investigating new paths towards ultra-compact X-ray sources [54]. The possibility to excite high acceleration gradients in multilayer graphene structures is also being investigated [56].

In the next section, we describe the plasmonic acceleration, which is a novel acceleration technique based on the excitation of suitable surface plasmonic modes in conducting materials. More concretely, we focus on plasmonic acceleration using nanostructures or metamaterials based on allotropes of carbon.

3.3 Plasmonic acceleration

Plasmonics can be defined as the study of the interaction between electromagnetic fields and the free electron Fermi gas in conducting solids. External electromagnetic fields can excite plasmons, that is, collective oscillations of conduction electrons in metals [57]. To some extent, this collective effect could be exploited to generate ultra-high acceleration gradients. **Figure 6** depicts a scheme of excited plasmons in metallic surfaces. The oscillation of induced longitudinal electric field reminds that in a sequence of a multi-cell RF cavity operating at π-mode.

The excitation of surface plasmonic modes [58, 59] can be driven either by charged particle beam [60] or by laser [61]. To be effective, the driver dimensions should match the spatial ($\sim$ nm) and time (sub-femtoseconds) scales of the excited plasmonic oscillations. Wakefield driving sources working on these scales are now experimentally realisable. For instance, attosecond X-ray lasers are possible thanks to the pulse compression technique [50]. In the case of beam-driven wakefields, the experimental facility FACET-II at SLAC [62] will allow the access to 'quasi-solid' electron bunches with densities up to 10^{24} cm^{-3} and submicron longitudinal size. A comparison of the range of spatial and time scales of the electric field oscillations and achievable acceleration gradient for standard and novel acceleration methods is shown
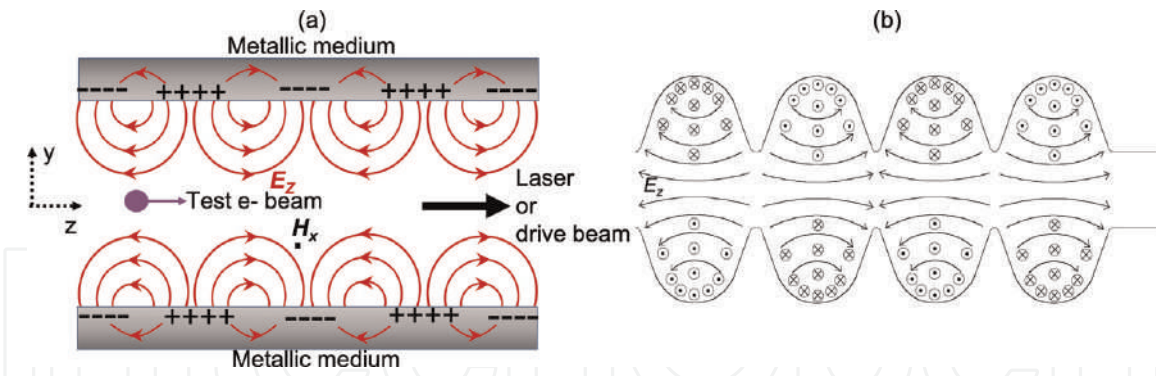
Figure 6.
(a) Plasmonic acceleration concept. (b) Comparison with an RF cavity operating in π-mode. The drawings are not to scale. While the plasmonic structure has micrometric or submicrometric apertures and lengths on the order of 1 mm, for instance, a 9-cell RF cavity has usually apertures of tens of mm and lengths on the order of m.
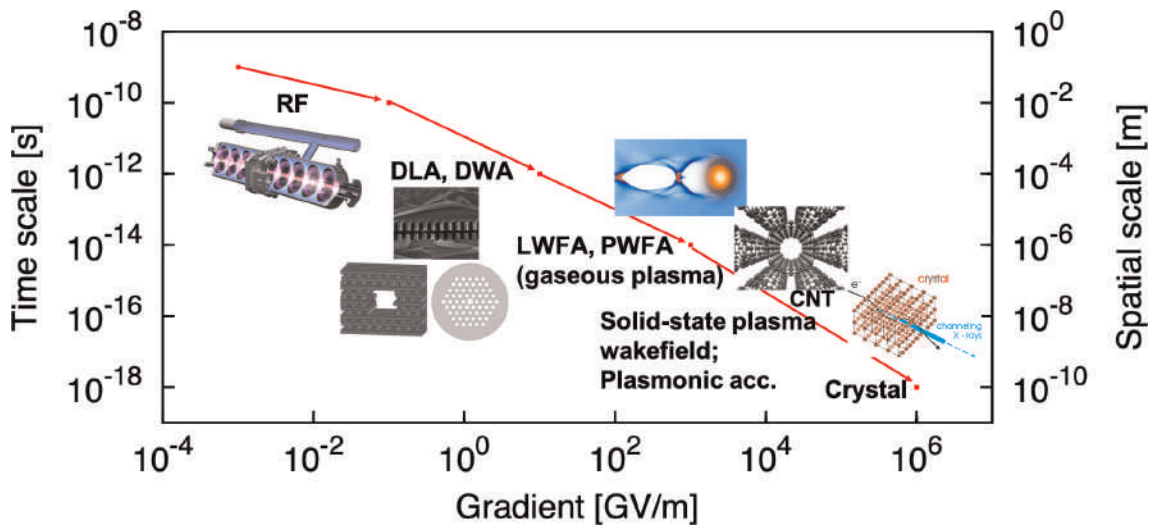

Figure 7.
Schematic comparing the space and time scales of the longitudinal electric field components generated by different techniques for charged particle acceleration and their corresponding amplitude (acceleration gradient). The cases of nanostructure wakefields, plasmonic and crystal acceleration are based on theoretical and numerical predictions.

in **Figure 7**. In principle, solid-state wakefields and plasmonics acceleration with nanostructures are predicted to have the potential to generate higher acceleration gradients than DWA and DLA, LWFA and PWFA with gaseous plasma. Plasmonic acceleration with nanostructures could be considered an intermediate step between PWFA and crystal channelling acceleration towards the PV/m gradient regime.

Due to their special thermo-mechanical and optoelectronic properties, materials based on carbon nanotubes arrays or graphene could offer an excellent medium to generate plasmonic wakefield acceleration. For instance, conduction electrons in CNTs could have densities $n_e \sim 10^{23}$ cm^{-3}. In principle, as proved in [63, 64], in the linear regime the plasmonic dynamics in CNT bundles can be described by classical plasma formulae. Therefore, from Eq. (1) we can estimate a maximum longitudinal wakefield $E_z \sim 10$ TV/m.

Particle-In-Cell (PIC) simulations of beam-driven wakefield acceleration in cylindrical metallic hollow structures (**Figure 8**) with micrometric or nanometric apertures have shown the feasibility of obtaining gradients ≳100 GV/m, envisioning the possibility of an ultra-compact PeV linear collider [66–68]. Similar gradient values have
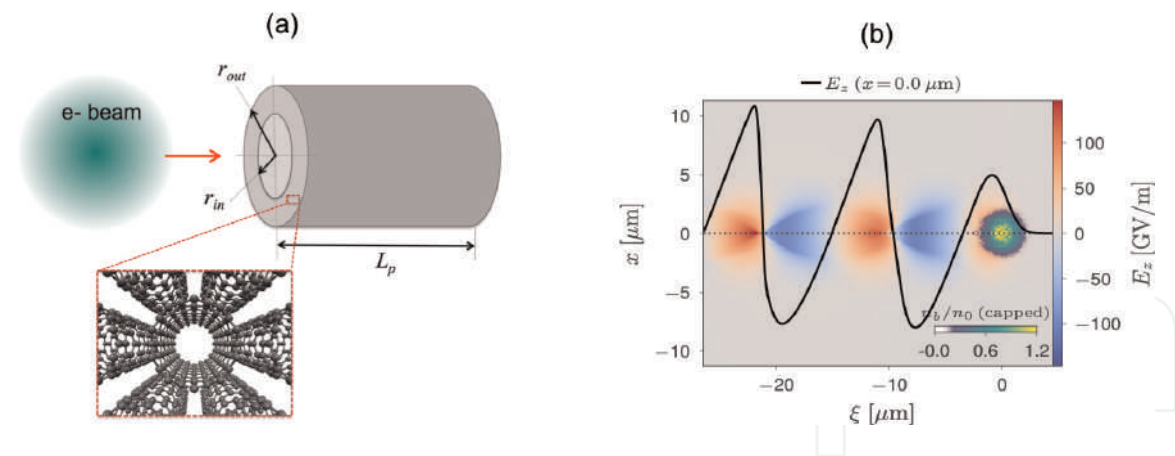
Figure 8.
(a) Schematic model for beam-driven wakefield simulation using a hollow cylinder of solid-state plasma confined in a wall of thickness $r_{out} - r_{in}$ and length L_p. In this model, the cylinder wall represents a solid made of CNT bundles. (b) an example of longitudinal wakefield as a function of the longitudinal coordinate $\xi = z - ct$, with c the speed of light. This particular case has been computed using the PIC code FBPIC [65].

also been predicted from PIC simulations of X-ray laser-driven wakefield acceleration in nanotubes [69].

One of the important properties of the plasmonic excitation is that the ionic lattice of the material remains strongly correlated. Unlike the plasmonic acceleration, other novel solid-state-based acceleration techniques require the complete ionisation of the ionic lattice or the ablation of solids, as described in the next section.

3.4 Target normal sheath acceleration

Solid-state plasmas can also be created by ablation of solids using high-intensity near-infrared femtosecond lasers. In this case, unlike in the plasmon wakefield excitation, the individual ions are uncorrelated. For example, the so-called target normal sheath acceleration (TNSA) technique is based on the ablation of a metallic thin foil [70]. The mechanism is schematically represented in **Figure 9**. A thin foil is irradiated by an intense laser pulse. The laser prepulse creates a pre-plasma on the target's front side. The main pulse interacts with the plasma and accelerates MeV-energy electrons mainly in the forward direction. The electrons propagate through the target, where collisions with the background material can increase the divergence of the electron current. Then the electrons leave the rear side, resulting in a dense sheath. An electric
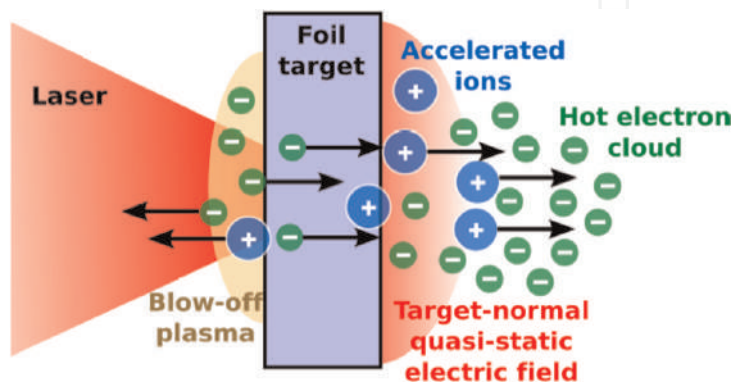

Figure 9.
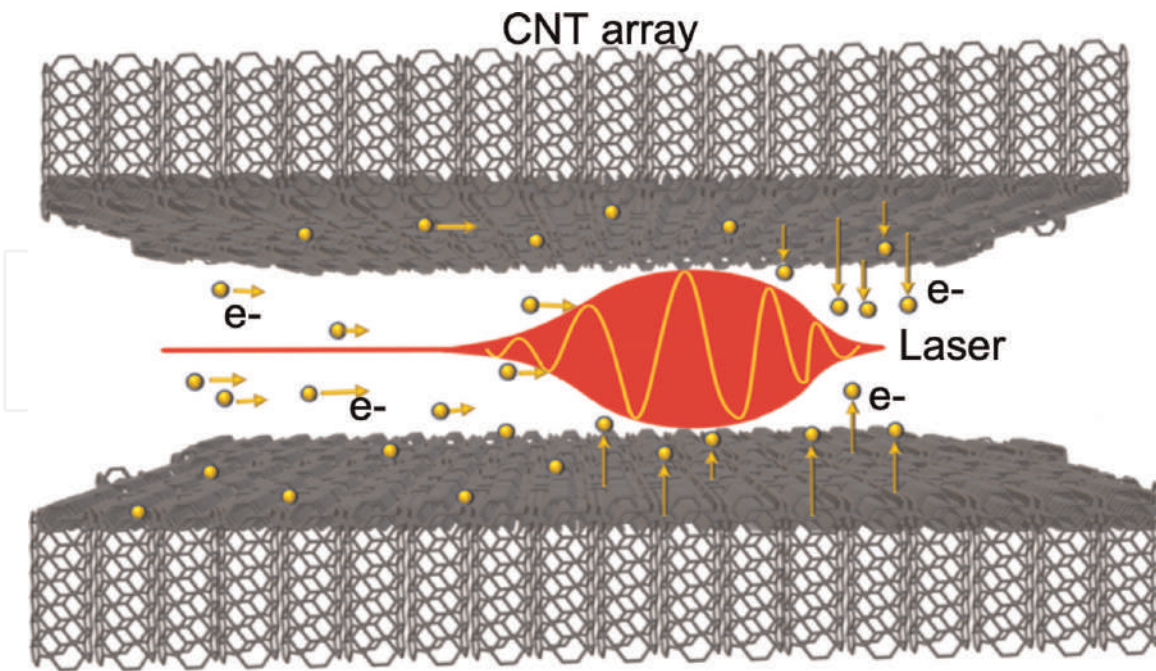*Target normal sheath acceleration mechanism.*

Figure 10.
Laser wakefield acceleration concept with aligned CNT arrays. In this particular configuration, CNTs are arranged perpendicularly to the laser propagation [71].

field due to charge separation is created. The field is of the order of the laser electric field ($\sim$TV/m), which ionises atoms at the surface. Eventually, the ions are accelerated in this sheath field, pointing in the target normal direction.

3.5 Solid-state plasma by electron field emission

Electron field emission from nanostructures could offer another interesting way to generate solid-state plasma. A possible configuration based on two layers of aligned CNT arrays and a gap in between them is shown in **Figure 10**. Taking into account the low work function of CNTs and their emission properties, a first intense laser pulse, travelling through the gap between the CNT sheets, could be used to induce electron field emission from CNT arrays. Then extracted electrons in the gap are accelerated by the ponderomotive force of a second laser pulse. For more details see Ref. [71].

4. Outlook and prospects

Currently, particle accelerators play an important role in many areas, including fundamental science, medicine, industry and society in general. During the last 100 years, the research in HEP has been the main driving force behind the development and progress of the accelerator technology. The LHC is currently the world's most advanced and powerful accelerator, and the only multi-TeV collider in operation. It consists of a 27-km ring of superconducting magnets with a number of accelerating structures based on RF electromagnetic fields to accelerate particles. The next generation of RF-driven high energy accelerators will pose serious challenges in terms of infrastructure size, technology and cost.

The current state-of-the-art of the RF techniques is limited to gradients on the order of 100 MV/m. Hence, larger and more expensive accelerator facilities are

necessary in order to go beyond the LHC capabilities. Therefore, it is important to explore alternative advanced acceleration techniques to overcome the limitations of conventional technologies, thus progressing towards more compact, sustainable and economical particle accelerators. For many years, the development of inexpensive and compact 'table-top' high energy particle accelerators and light sources has been the ultimate dream of the accelerator physics community.

Some of the most promising novel acceleration techniques have briefly been reviewed in this chapter. For instance, PWFA and LWFA using gaseous plasma have experimentally demonstrated to be able to achieve ~ 100 GV/m acceleration [19–24]. Another path towards TV/m acceleration is the use of special solid-state media, such as micrometric and millimetric grating dielectric structures, reaching ~ 1–10 GV/m acceleration [38, 39].

Crystals and, more recently, nanostructures have also attracted attention to create a solid-state plasma medium with electron densities 1–6 orders of magnitude higher than those in gaseous plasmas. For example, recent theoretical and numerical studies have shown the feasibility of obtaining tens of TV/m fields in nanomaterials by excitation of non-linear plasmonic modes driven by a high-density sub-micron particle bunch [66, 67]. To obtain multi-TV/m fields other techniques rely on the ablation of solids [70] or the induced electron field emission from nanomaterials [71].

It is necessary to remark that the excitation of solid-state plasma wakefields requires the use of driving sources (lasers or charged particle bunches) at the same time and spatial scales as the wakefield oscillations in the plasma. In principle, wakefield driving sources working on solid-state plasma scales are now experimentally realisable. Attosecond X-ray lasers are possible thanks to the pulse compression [49, 50]. In the case of beam-driven wakefields, the experimental facility FACET-II at SLAC [62] could deliver 'quasi-solid' electron beams in the near future. Therefore, an experimental proof-of-concept of solid-state PWFA could possibly become a reality within the next 10 years.

It is also worth mentioning that nanostructures and metamaterials, due to their special and flexible optoelectronic properties, could also provide an excellent medium to create compact X-ray sources, e.g., X-ray light sources based on CNT arrays [72].

In conclusion, the different advanced acceleration techniques described in this chapter have the potential to transform the current paradigm in accelerator physics. They offer novel pathways to multi-GV/m and multi-TV/m field regimes. This will open new horizons to the physics of extreme fields, particularly in collider physics, light sources, and in many other areas of applied sciences, medicine and industry.

Acknowledgements

Abbreviations

AWAKE	Advance Wakefield Experiment
CERN	European Organisation for Nuclear Research
CLIC	Compact Linear Collider

CNT	Carbon Nanotube
DLA	Dielectric Laser-driven Wakefield Acceleration
DWA	Dielectric Wakefield Acceleration
ERL	Energy Recovery Linac
EuPRAXIA	European Plasma Research Accelerator with Excellence in Applications
FACET-II	Facility for Advanced Accelerator Experimental Test II
FCC	Future Circular Collider
HEP	High Energy Physics
HERA	Hadron-Electron Ring Accelerator
ILC	International Linear Collider
LEP	Electron-Positron Collider
LHC	Large Hadron Collider
LWFA	Laser Wakefield Acceleration
PIC	Particle-In-Cell
PWFA	Plasma Wakefield Acceleration
R&D	Research and Development
RF	Radiofrequency
SLAC	Stanford Linear Accelerator Center
SLC	Stanford Linear Collider
SPS	Super Proton Synchrotron
TNSA	Target Normal Sheath Acceleration

Author details

Javier Resta López
Institute of Materials Science (ICMUV), University of Valencia, Valencia, Spain

*Address all correspondence to: javier2.resta@uv.es

IntechOpen

References

[1] Sessler A, Wilson E. Engines of Discovery. A Century of Particle Accelerators. Revised and Expanded Edition. Singapore: World Scientific; 2014. 280 p. DOI: 10.1142/8552

[2] Zimmermann F, Shiltsev VD. Modern and future colliders. Reviews of Modern Physics. 2021;**93**(1):015006. DOI: 10.1103/RevModPhys.93.015006

[3] Bruning O, Collier P. Building a behemoth. Nature. 2007;**448**:285-289. DOI: 10.1038/nature06077

[4] Collaboration ATLAS. Observation of a new particle in the search of the standard model Higgs boson with the ATLAS detector at the LHC. Physics Letters B. 2012;**716**:1-29. DOI: 10.1016/j.physletb.2012.08.020

[5] Collaboration CMS. Observation of a new boson at the mass of 125 GeV with the CMS experiment at the LHC. Physics Letters B. 2012;**716**:30-61. DOI: 10.1016/j.physletb.2012.08.021

[6] Benedikt M et al. FCC-ee: The Lepton collider. The European Physical Journal Special Topics. 2019;**228**:261-623. DOI: 10.1140/epjst/e2019-900045-4

[7] Benedikt M et al. FCC-hh: The hadron collider. The European Physical Journal Special Topics. 2019;**228**:755-1107. DOI: 10.1140/epjst/e2019-900087-0

[8] Michizono S. The international linear collider. Nature Reviews Physics. 2019;**1**: 244-245. DOI: 10.1038/s42254-019-0044-4

[9] Stapnes S. The compact linear collider. Nature Reviews Physics. 2019;**1**: 235-237. DOI: 10.1038/s42254-019-0051-5

[10] Long KR et al. Muon colliders to expand frontiers of particle physics. Nature Physics. 2021;**17**:289-292. DOI: 10.1038/s41567-020-01130-x

[11] Cai J, Syratchev I. KlyC: 1.5-D large-signal simulation code for klystrons. IEEE Transactions on Plasma Science. 2019;**47**(4):1734-1741. DOI: 10.1109/TPS.2019.2904125

[12] Litvinenko VN, Roser T, Chamizo-Llatas M. High-energy high-luminosity e^+e^- collider using energy-recovery linacs. Physics Letters B. 2020;**804**: 135394. DOI: 10.1016/j.physletb.2020.135394

[13] Shiltsev VD. High energy particle colliders: Past 20 years, next 20 years and beyond. Physics-Uspekhi. 2012; **55**(10):965-976. DOI: 10.3367/UFNe.0182.201210d.1033

[14] Ferrario M. Present and future accelerator options beyond the LHC. Annalen der Physik. 2016;**528**(1–2): 151-160. DOI: 10.1002/andp.201500240

[15] Abe T et al. Breakdown study based on direct in situ observation of inner surfaces of an rf accelerating cavity during a high-gradient test. Physical Review Accelerators and Beams. 2016; **19**:102001. DOI: 10.1103/PhysRevAccelBeams.19.102001

[16] Tajima T, Dawson JM. Laser Electron Accelerator. Physical Review Letters. 1979;**43**:267-270. DOI: 10.1103/PhysRevLett.43.267

[17] Joshi C. Plasma accelerators. Scientific American. 2006;**294**(2):40-47

[18] Chen P, Dawson JM, Huff RW, Katsouleas T. Acceleration of electrons by the interaction of a bunched Electron

beam with a plasma. Physical Review Letters. 1985;**54**(7):693-696. DOI: 10.1103/PhysRevLett.54.693

[19] Gordon D et al. Observation of Electron energies beyond the linear dephasing limit from a laser-excited relativistic plasma wave. Physical Review Letters. 1998;**80**:2133-2136. DOI: 10.1103/PhysRevLett.80.2133

[20] Leemans WP et al. Multi-GeV Electron beams from capillary-discharge-guided Subpetawatt laser pulses in the self-trapping regime. Physical Review Letters. 2014;**113**(24): 245002. DOI: 10.1103/ PhysRevLett.113.245002

[21] Litos M et al. High-efficiency acceleration of an electron beam in a plasma wakefield accelerator. Nature. 2015;**515**:92-95. DOI: 10.1038/ nature13882

[22] Blue BE et al. Plasma-Wakefield acceleration of an intense positron beam. Physical Review Letters. 2003;**90**: 214801. DOI: 10.1103/ PhysRevLett.90.214801

[23] Corde S et al. Multi-gigaelectronvolt acceleration of positrons in a self-loaded plasma wakefield. Nature. 2015;**524**: 442-445. DOI: 10.1038/nature14890

[24] Doche A et al. Acceleration of a trailing positron bunch in a plasma wakefield accelerator. Scientific Reports. 2017;**7**:14180. DOI: 10.1038/s41598-017-14524-4

[25] Adli E, et al. (AWAKE Collaboration). Acceleration of electrons in the plasma wakefield of a proton bunch. Nature 2018;561:363–367. DOI: 10.1038/s41586-018-0485-4.

[26] Geddes CGR et al. High-quality Electron beams from a laser wakefield accelerator using Plasma-Channel guiding. Nature. 2004;**431**(7008): 538-541. DOI: 10.1038/nature02900

[27] Mangles SPD et al. Monoenergetic beams of relativistic electrons from intense-laser plasma interactions. Nature. 2004;**431**(7008):535-538. DOI: 10.1038/nature02939

[28] Faure J et al. A laser-plasma accelerator producing Monoenergetic Electron beams. Nature. 2004;**431**(7008): 541-544. DOI: 10.1038/nature02963

[29] Esarey E, Schroeder CB, Leemans WP. Physics of laser-driven plasma-based electron accelerators. Reviews of Modern Physics. 2009;**81**(3): 1229-1285. DOI: 10.1103/ RevModPhys.81.1229

[30] Leemans WP, Esarey E. Laser-driven plasma-wave electron accelerators. Physics Today. 2009;**62**: 44-49. DOI: 10.1063/1.3099645

[31] Schroeder CB, Esarey E, Geddes C, Benedetti C, Leemans W. Physics considerations for laser-plasma linear colliders. Physical Review Special Topics-Accelerators and Beams. 2010;**13**:101301. DOI: 10.1103/PhysRevSTAB. 13.101301

[32] Leemans W. White paper of the ICFA-ICUIL, joint taks force: High power laser technology for accelerators. In: ICFA Beam Dyn. Newslett. Vol. 56. International Committee for Future Accelerators (ICFA). 2011. pp. 10-88. Available from: https://icfausa.jlab.org/archive/newsletter/icfa-bd-nl-56.pdf

[33] Walker PA et al. Facility considerations for a European plasma accelerator infrastructure (EuPRAXIA). In: Proceedings of the 10th International Particle Accelerator Conference (IPAC'19); 19-24 May 2019; Melbourne, Australia: Paper THPGW025.

[34] Joshi C, Corde S, Mori WB. Perspectives on the generation of electron beams from plasma-based accelerators and their near and long term applications. Physics of Plasmas. 2020;**27**:070602. DOI: 10.1063/5.0004039

[35] Scandale W, Taratin AM. Channeling and volume reflection of high-energy charged particles in short bent crystals. Crystal assisted collimation of the accelerator beam halo. Physics Reports. 2019;**815**:1-107. DOI: 10.1016/j.physrep.2019.04.003

[36] Thompson MC. Breakdown limits on Gigavolt-per-meter Electron-beam-driven Wakefields in dielectric structures. Physical Review Letters. 2008;**100**:214801. DOI: 10.1103/PhysRevLett.100.214801

[37] Breuer J, Hommelhoff P. Laser-based acceleration of nonrelativistic electrons at a dielectric structure. Physical Review Letters. 2013;**111**:134803. DOI: 10.1103/PhysRevLett.111.134803

[38] Peralta EA et al. Demonstration of electron acceleration in a laser driven dielectric microstructure. Nature. 2013;**503**:91-94. DOI: 10.1038/nature12664

[39] O'Shea BD et al. Observation of acceleration and deceleration in gigaelectron-volt-per-metre gradient dielectric wakefield accelerators. Nature Communications. 2016;**7**:12763. DOI: 10.1038/ncomms12763

[40] Blau SK. Particle acceleration on a chip. Physics Today. 2013;**66**(12):19. DOI: 10.1063/PT.3.2205

[41] England RJ, Hommelhoff P, Byer RL. Microchip accelerators. Physics Today. 2021;**74**(8):42-49. DOI: 10.1063/PT.3.4815

[42] Wei Y et al. Beam quality study for a grating-based dielectric laser-driven

accelerator. Physics of Plasmas. 2017;**24**: 023102. DOI: 10.1063/1.4975080

[43] Chen P, Noble RJ. A solid state accelerator. AIP Conf. Proc. 1987;**156**: 222. DOI: 10.1063/1.36458

[44] Östling D, Tománek RA. Electronic structure of single-wall, multiwall and filled carbon nanotubes. Physical Review B. 1997;**55**(20):13980-13988. DOI: 10.1103/PhysRevB.55.13980

[45] Tajima T, Cavenago M. Crystal X-ray accelerator. Physical Review Letters. 1987;**59**(13):1440-1443. DOI: 10.1103/PhysRevLett.59.1440

[46] Chen P, Noble RJ. Crystal channel collider: Ultra-high energy and luminosity in the next century. AIP Conf. Proc. 1997; **398**:273. DOI: 10.1063/1.53055

[47] Borrmann G. Die Absortion von Röntgenstrahlen im Fall der Interferenz. Zeitschrift für Physik. 1950;**127**:297-323. DOI: 10.1007/BF01329828

[48] Campbell HN. X-ray absorption in a crystal set at the Bragg angle. Journal of Applied Physics. 1951;**22**:1139. DOI: 10.1063/1.1700122

[49] Strickland D, Mourou G. Compression of amplified chirped optical pulses. Optics Communications. 1985;**56**(3):219-221. DOI: 10.1016/0030-4018(85)90120-8

[50] Mourou G, Mironov S, Khazanov E, Sergeev A. Single cycle thin film compressor opening the door to Zeptosecond-Exawatt physics. The European Physical Journal Special Topics. 2014;**223**:1181-1188. DOI: 10.1140/epjst/e2014-02171-5

[51] Li P et al. Recent advances in focused ion beam nanofabrication for nanostructures and devices:

Fundamentals and applications. Nanoscale. 2021;**13**:1529-1565. DOI: 10.1039/D0NR07539F

[52] Pint CL et al. Dry contact transfer printing of aligned carbon nanotube patterns and characterization of their optical properties for diameter distribution and alignment. ACS Nano. 2013;**4**(2):1131-1145. DOI: 10.1021/nn9013356

[53] Chen X et al. Atomic layer lithography of wafer-scale nanogap arrays for extreme confinement of electromagnetic waves. Nature Communications. 2013;**4**:2361. DOI: 10.1038/ncomms3361

[54] Pizzi A et al. Graphene metamaterials for intense, Tunable, and compact extreme ultraviolet and X-ray sources. Advancement of Science. 2020;**7**:1901609. DOI: 10.1002/advs.201901609

[55] Kong L-B, Chen Z. Plasmonic electron acceleration with the meta-surfaces. Physics of Plasmas. 2017;**24**:083111. DOI: 10.1063/1.4997481

[56] Bontoiu C et al. TV/M Laser-Driven Accelerating Gradients in Graphene. Proceedings of the 10th International Particle Accelerator Conference (IPAC'22); 12-17 June 2022; Bangkok, Thailand: Paper WEPOST043

[57] Sarid D, Challener W. Modern Introduction to Surface Plasmons: Theory, Mathematica Modeling, and Applications. Cambridge: Cambridge University Press; 2010. 371 p. DOI: 10.1017/CBO9781139194846

[58] Ukhtary MS, Saito R. Surface plasmon in graphene and carbon nanotubes. Carbon. 2020;**167**:455. DOI: 10.1016/j.carbon.2020.05.019

[59] Macchi A. Surface plasmons in superintense laser-solid interactions. Physics of Plasmas. 2018;**25**:031906. DOI: 10.1063/1.5013321

[60] Nejati M et al. The single wall carbon nanotube waveguides and excitations of their $\sigma + \pi$ plasmons by an electron beam. Physics of Plasmas. 2009;**16**: 022108. DOI: 10.1063/1.3077306

[61] Fedeli L et al. Electron acceleration by relativistic surface Plasmons in laser-grating interactions. Physical Review Letters. 2016;**116**:015001. DOI: 10.1103/PhysRevLett.116.015001

[62] Yakimenko V et al. FACET-II facility for advanced accelerator experimental tests. Physical Review Accelerators and Beams. 2019;**22**:101301. DOI: 10.1103/PhysRevAccelBeams.22.101301

[63] Rider AE, Ostrikov K, Furman SA. Plasmas meet plasmonics: Everything old is new again. European Physical Journal D: Atomic, Molecular, Optical and Plasma Physics. 2012;**66**:226. DOI: 10.1140/epjd/e2012-30273-3

[64] Que W. Theory of plasmons in carbon nanotube bundles. Journal of Physics: Condensed Matter. 2002;**14**: 5239-5253. DOI: 10.1088/0953-8984/14/20/319

[65] Lehe R, Kirchen M, Andriyash IA, Godfrey BB, Vay J-L. A spectral quasi-cylindrical and dispersion free particle-In-cell algorithm. Computer Communications. 2016;**203**:66-82. DOI: 10.1016/j.cpc.2016.02.00

[66] Sahai AA, Tajima T, Taborek P, Shiltsev VD. Solid-state tube wakefield accelerator using surface waves in crystals. International Journal of Modern Physics A. 2020;**34**:1943009-1943029. DOI: 10.1142/9789811217135-0009

[67] Sahai AA. Nanomaterials based Nanoplasmonic accelerators and light-sources driven by particle-beams. IEEE Access. 2021;**9**:54831-54839. DOI: 10.1109/ACCESS.2021.3070798

[68] Resta-Lopez J et al. Study of Ultra-High Gradient Acceleration in Carbon Nanotube Arrays. Proceedings of the 9th International Particle Accelerator Conference (IPAC'18); 29 April-4 May 2018; Vancouver, Canada: Paper TUXGBE2. DOI: 10.18429/JACoW-IPAC2018-TUXGBE2

[69] Zhang X et al. Particle-in-cell simulation of X-ray wakefield acceleration and betatron radiation in nanotubes. Physical Review Accelerators and Beams. 2016;**19**:101004. DOI: 10.1103/PhysRevAccelBeams.19.101004

[70] Roth M, Schollmeier M. Ion Acceleration–Target Normal Sheath Acceleration. Proceedings of the CAS-CERN Accelerator School: Plasma Wake Acceleration; 23-29 November; Geneva, Switzerland. DOI: 10.5170/CERN-2016-001.231

[71] Nicks BS et al. High-density dynamics of laser wakefield acceleration from gas plasmas to nanotubes. Photonics. 2021;**8**:216. DOI: 10.3390/photonics8060216

[72] Shin YM. Optically controlled coherent X-ray radiations from photo-excited nanotubes. Nuclear Instruments and Methods in Physics Research Section B: Beam Interactions with Materials and Atoms. 2017;**407**:276-281. DOI: 10.1016/j.nimb.2017.07.019

We are IntechOpen,
the world's leading publisher of
Open Access books
Built by scientists, for scientists

6,300
Open access books available

171,000
International authors and editors

190M
Downloads

154
Countries delivered to

Our authors are among the

TOP 1%
most cited scientists

12.2%
Contributors from top 500 universities

BOOK CITATION INDEX
CLARIVATE ANALYTICS
INDEXED

WEB OF SCIENCE™

Selection of our books indexed in the Book Citation Index
in Web of Science™ Core Collection (BKCI)

Interested in publishing with us?
Contact book.department@intechopen.com

Numbers displayed above are based on latest data collected.
For more information visit www.intechopen.com

Faster Fusion Power from Spherical Tokamaks with High-Temperature Superconductors

Colin Windsor and Gurdeep Kamal

Abstract

The use of spherical tokamaks and high-temperature superconductors (HTSs) offers the possibility of achieving faster fusion power by allowing plants of high-field, high plasma pressure, and good energy confinement thereby reducing the need for large plasma volumes. This spatially efficient energy-dense approach accesses quicker development and the possibility of modular construction. An overview of high-performance computational (HPC) capabilities at Tokamak Energy is given. We describe, at a highlevel and in practical terms, the use of theory, models, algorithms, and applications to develop spherical tokamak designs in an integrated fashion. A challenge of spherical tokamaks is that there is less room for the neutron and gamma shield necessary to prevent heating and radiation damage to the HTS core. Tungsten boride shield materials may be able to provide an optimal combination of inelastic (n, gamma) reactions and gamma attenuation. The neutron energy is reduced largely by inelastic reactions to energies where boron absorption occurs, while tungsten attenuates the resulting gammas rapidly. Although inelastic scattering is shown to be the key to tungsten boride shield performance, it is shown that the remaining neutrons generated in the plasma and transmitted without reaction through the shield dominate the heat deposition in the HTS core.

Keywords: fusion, spherical tokamaks, tungsten borides, shielding, neutrons, gammas

1. Introduction

Fusion power is one of the few options capable of supplying abundant safe baseline energy to the world [1]. In 1955, John Lawson, working at Harwell, defined a condition for fusion power depending on plasma density n and temperature T. It was later extended to include confinement time τ_{E}., to form what is now known as the "triple product" $nT\tau_{E}$ which must exceed 3.10^{21} keV m^{-3} s for fusion reactions to be self-sustaining [2]. Costley, Hugill, and Buxton [3] showed that this triple product is proportional to the equivalent triple product $\beta B_{T}^{2}\tau_{E}$ where β is the ratio of the plasma pressure, $p_{pla} = n.kT$, to the magnetic pressure $p_{mag} = B^{2}/2\,\mu_{0}$. B_{T} is the toroidal field and τ_{E} is the energy confinement time, related to the plasma volume, kT is the thermal energy, and μ_{0} is the vacuum permeability constant. They showed that the high
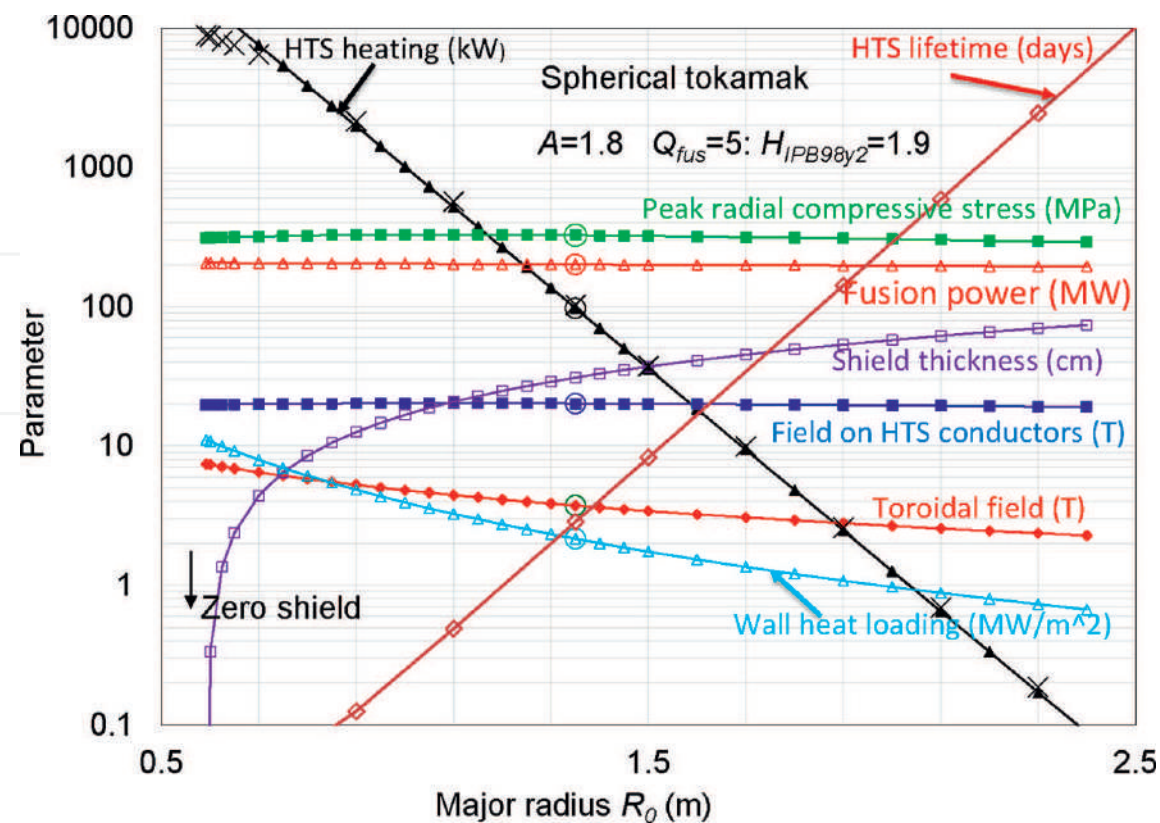
Figure 1.
Some example results from the 2017 Costley system code scanning as a function of major radius for a constant fusion gain Q_{fus} = 5, spherical tokamak aspect ratio A = 1.8, and confinement scaling H_{IPB9y2} = 1.9. In this series, the core diameter is increased by 8% for each change in major radius to keep the peak radial compressive stress (green squares) approximately constant. The fusion power P_{fus} (red open triangles) is seen to be roughly independent of major radius. The shield thickness (violet open squares) increases, initial rapidly from zero, with major radius. Also shown are the wall heat loading (sky blue open triangles) and the toroidal field B_T (blue closed squares). Incorporated into the code are the HTS core heating (black closed triangles, with individual calculations as crosses) and the estimated HTS lifetime from the fast neutron fluence (pink open diamonds).

β values possible with spherical tokamaks and the higher toroidal fields B_T possible with high-temperature superconductors (HTSs) were a viable alternative to ever-increasing tokamak size in the search for fusion power.

Their method in [3] was to write a "system code," in their case a simple spreadsheet, to incorporate the key input parameters and equations to calculate key output parameters. Innovations were to use the fusion gain Q_{fus} as an input parameter to their calculations and to introduce checks to ensure that the actual plasma density was never above 0.8 of the known Greenwald density limit and the plasma normalized pressure β value never above 0.9 of the Troyon β limit to plasma stability. Since high density and high plasma pressure are both desirable for high fusion gain, the best plasma conditions would be those that would approach these limits.

Some example results using their code are shown in **Figure 1**. The fusion power with these scan conditions is seen to be almost independent of tokamak size, while key engineering conditions, such as the radial compressive stress at the top of tokamak, the magnetic field at the HTS conductors, and the wall loading power are all satisfactory. The purple open squares show the thickness of the shield, rising rapidly from 0.55 m major radius.

2. The use of modeling codes to optimize spherical tokamak designs

Figure 1 describes how an integration of tokamak physics, HTS design, neutronics and computational fluid dynamics, and magnetohydrodynamic stress codes could help predict optimal tokamak design. To these, we must add codes for tritium breeding, heat transfer, design, construction, and decommissioning costs to produce a suite of codes that must be put together to predict a new spherical tokamak power plant design. It is with this aim that Tokamak Energy has invested in high-performance computational (HPC) capabilities.

The "system codes" which used to be implemented on Excel spreadsheets are greatly expanded and are verified by fitting experimental data from actual tokamaks like ST40. Future system codes are envisaged to use a single-design geometry to perform calculations automatically on a suite of tools involving physics, HTS magnet design, neutronics, heat flow, and engineering to obtain the parameters required to optimize a tokamak. The integration of system codes and tools used by multiple departments allows for an automated, iterative optimization of the tokamak design. HTS magnet codes need to consider quench protection and be compared to actual demo magnet experiments to verify their performance. The analytic stress equations, once commonly used, are now replaced by finite element codes whose performance can be judged by experimental data from the ST40 tokamak. The neutronics of HTS and biological shields is now rather straightforwardly assessed by activation foils under actual conditions and actual measurements of dose rates during shots. A major part of the successful operation of tokamak power plants depends on being able to breed tritium from the fusion neutrons interacting with lithium in a "blanket" within the biological shield. These are being designed using neutronics codes but to date have not been tested. "Process" codes have the particularly difficult job of computing the "cost of electricity" for given costs of capital borrowing and materials. They are not easy to check and can so easily be outdated by unforeseen world events. The integration of system codes and tools used by multiple departments allows for an automated, iterative, optimization of the tokamak design.

All these aspects of physics, engineering, heat flow, magnet design, neutronics, radiation damage, shielding, tritium breeding, and cost estimates are possible with separate codes, and the objective is to integrate them into a suite of codes using the same computer-aided design (CAD) geometry on the same hardware. For this purpose, a high-performance computer was purchased by Tokamak Energy. The Tokamak Energy HPC currently has over 600 cores and over 3 TB of RAM available to use and continuously uses thousands of CPU hours daily to resolve physics and neutronics problems. **Figure 2** illustrates some of the principal applications and their codes used, with illustrations of the results they have given in hours by the high-performance computer illustrated at the center.

Key technological advancements needed to complete integration of CAD geometry between the suite of codes is in mesh generators. Currently, all tools have their own meshing methods with outputs in various formats. Geometrical information required to build successful inputs to the system tools are envisaged to be integrated into the CAD data. For example, neutronics heat deposition calculations require material compositions and densities for input and can output maximum heat deposition per CAD part which can then be stored as part of the CAD data for input for heat flow tools. Upgrades to the system code will utilize this data and perform meshing to the required resolution for each CAD part which are required for the system tools.
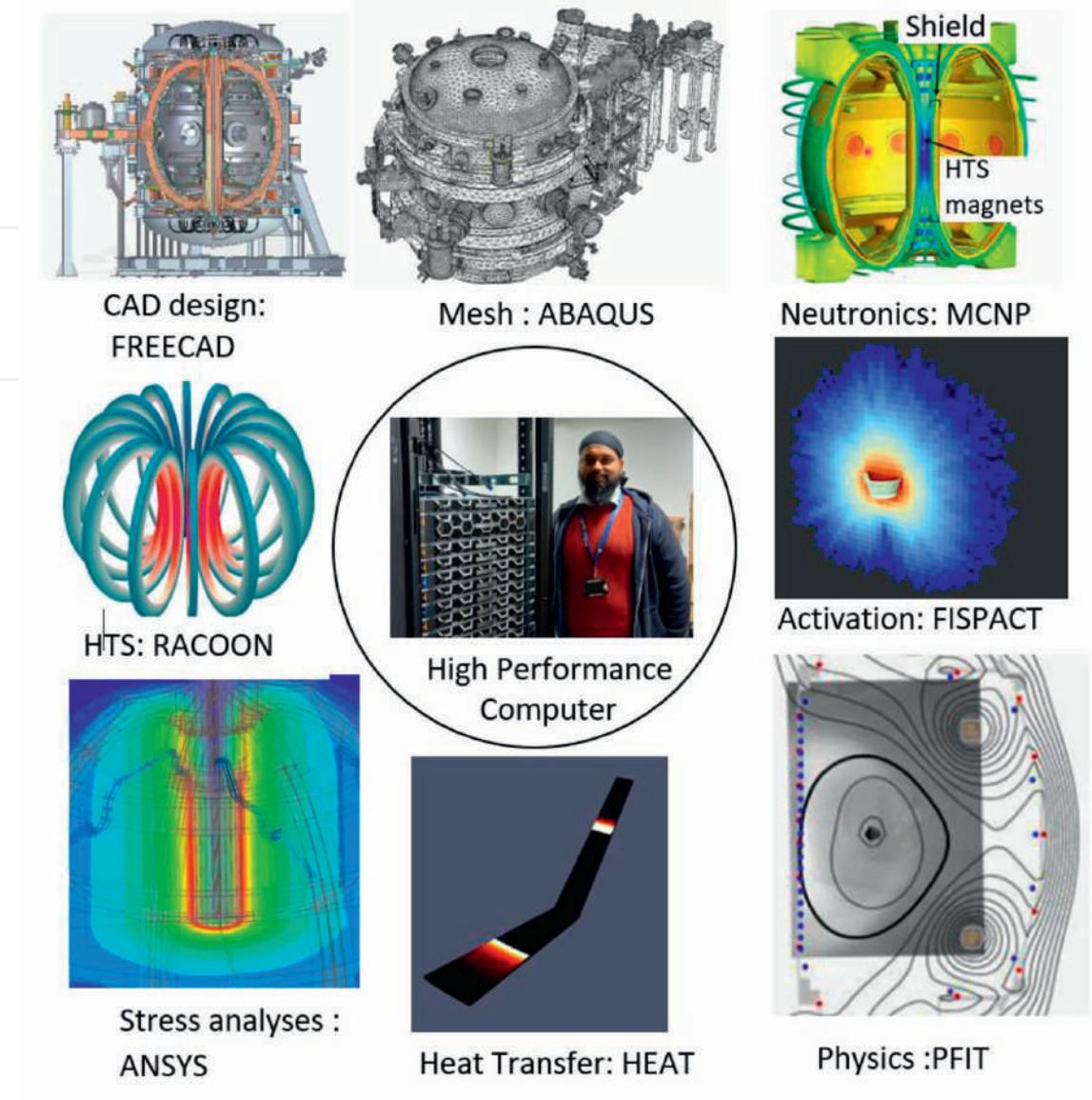
Figure 2.
The Tokamak Energy high-performance computer and examples of some of its applications and widely used code. Clockwise from the top left; the design "FREECAD" computer-aided design code of ST40, an "ABAQUS "code image of the mesh representation of the design, "MCNP" the Monte Carlo Neutral Particle code showing the neutronics fluence of a possible power plant, "FISPACT" the fusion activation code plot of the ST40 inner vacuum vessel, the in-house "PFIT" code plots of the ST40 field line fits to ST40 image, heat transfer in the ST40 divertor, the "HEAT" heat transfer code plots of the temperature in the HTS coils of a power plant, the "ANSYS" code plot of the mechanical stresses in the ST40 tokamak, and the "RACOON" in-house code for calculating HTS performance. In the center is the Tokamak Energy high-performance computer with author GK.

The following sections will shed some light on how we are effectively using the HPC for streamlining the design process, with an emphasis here on shield design. The use of "tally tagging" with the neutronics code MCNP is to answer key questions on the performance of shields, such as where the neutrons and gammas responsible for core heating originate, and from what reactions.

3. Spherical tokamaks

Costley [4] showed that the triple product $nT\tau_E$ could be expressed in terms of the H factor, the safety factor q, the major radius R_0, the toroidal field B_T, aspect ratio A,
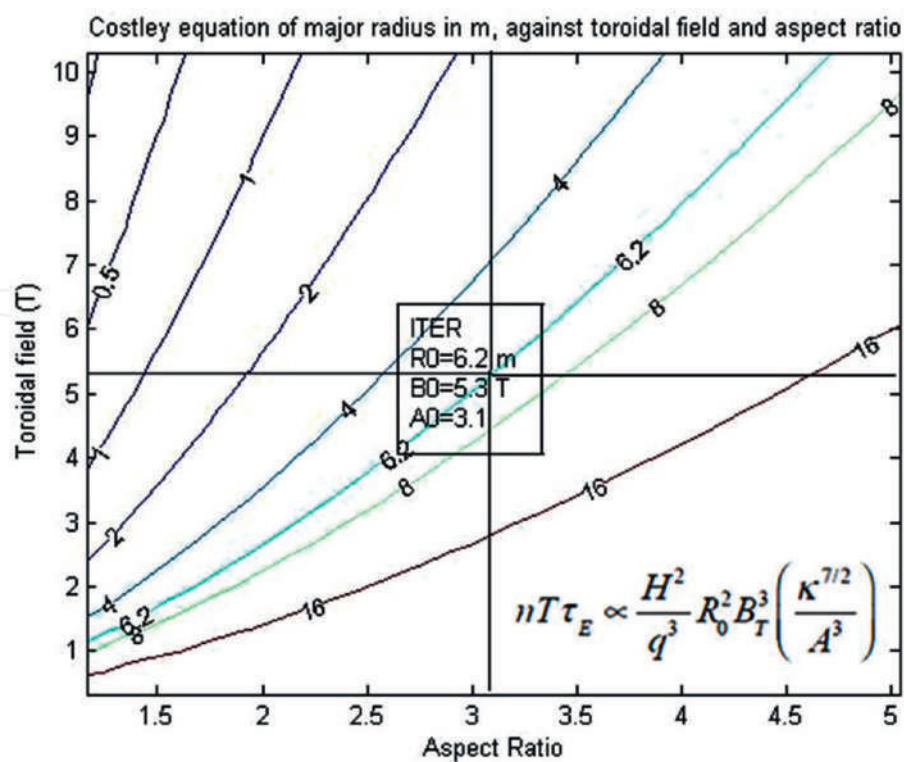
Figure 3.
The reduction in tokamak major radius (lines labeled in meters) which may be given by lower aspect ratios (X-axis) or by higher magnetic toroidal fields (Y-axis). The figure uses the equation shown from [4]. The data are scaled to the ITER operating point at major radius R_0 = 6.2 m, toroidal field B_0 = 5.3 T, and aspect ratio A = 3.1.

and the plasma elongation κ as $nT\tau_E = H^2.q^{-3}R_0^2B_T^3\kappa^{7/2}A^{-3}$. It is therefore possible to explore the dependence of the tokamak major radius R_0 as function of the tokamak aspect ratio and toroidal field at a constant value of the triple product, safety factor, and H factor. For example, those assumed for ITER are shown in **Figure 3**.

It is seen from **Figure 3** that going to lower aspect ratios (leftward) or to higher toroidal fields (upward) gives similar triple products from smaller tokamaks with lower major radii. This result is important because tokamaks of ITER size may be defined as "megaprojects" (technically project over $1B: ITER is over $20B). Historical studies of megaprojects show that cost and time overruns are the norm rather than the exception [5]. The reasons are obvious enough: megaprojects tend to be too big for one company, or even one country. They become difficult to manage as the layers of management between boss and worker become longer. With smaller tokamak power plants, agility becomes possible when projects can adapt quickly to any design optimization. A breakthrough would be achieved when modular construction becomes possible with centralized manufacture remote from the construction site.

In the following sections, these two opportunities, spherical tokamaks and high-temperature superconductor magnets, will be explored in more detail. **Figure 1** does also reveal the downside of spherical tokamaks. The purple open squares in **Figure 1** show that the space available for shielding diminishes slowly at large major radii but eventually rather rapidly to zero at some smaller major radius. Much of the remainder of this chapter will explore the materials and mechanisms most appropriate to a fusion tokamak shield. Tungsten boride shields have proved one possible option for a fusion power plant, and their performance is examined and compared with other possibilities.

In 1983, Sykes, Turner and Patel [6] and later Peng and Strickler [7] predicted the high plasma pressures β possible with low aspect ratio spherical tokamaks. The theory showed that β could indeed be raised by a combination of low aspect ratio and high elongation. In 1998, the START spherical tokamak team at Culham Laboratory in the UK achieved a breakthrough by reaching β values of order 40% [8], compared to the 6% or so achieved in JET or the 4% or so expected in ITER.

A simple-minded explanation for these increases in efficiency is suggested by **Figure 4** which shows the toroidal magnetic field B_T in Tesla around a center column carrying a constant current I as a function of radius r. The field is given by Ampere's law $B = 2\,\mu_0.I/4\pi r^2$ or $B\ (Tesla) = 0.2.I\ (MA)/r\ (m)^2$, so the smaller the radial distance the higher the field for a given center column current. For a current of 10 MA, the field is 2 Tesla at a radius of 1 m. A plasma with higher elongation κ and triangularity ε naturally squashes the plasma so that the orbiting electrons spend more time close the center column and make a more efficient use of the available field. Another advantage allowing the prospect of a power plant with reduced external current drive was the experimental observation of the bootstrap current, driven by plasma pressure gradients, which had been predicted theoretically by Bickerton, Connor, and Taylor in 1971 [9] and observed experimentally on the Princeton tokamak TFTR by Zarnstorff et al. [10] in 1988.

Bigger spherical tokamaks were soon built around the world, now upgraded to higher toroidal fields. These include MAST-UPRADE (0.55 Tesla) at Culham, UK [11], NSTX-U (1 Tesla) at Princeton, USA [12], and GLOBUS M2 (0.82 Tesla) at St. Petersberg, Russia [13]. Most recently constructed with the highest design toroidal field of 3 Tesla is the ST40 at Tokamak Energy Ltd., Milton Park, UK. This company was started in 2009 and
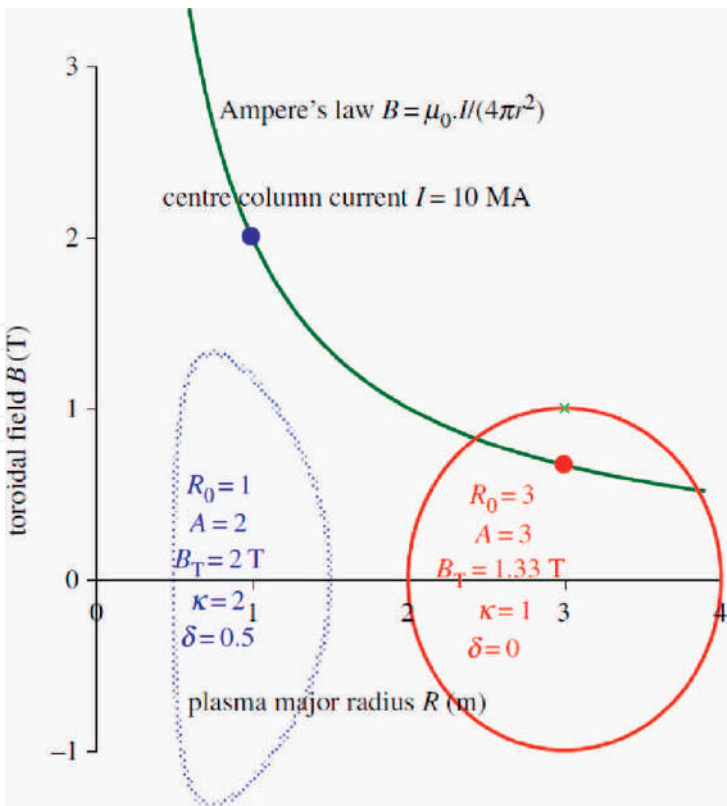
Figure 4.
In a low aspect ratio, high elongation plasma (left in blue), the orbiting electrons spend more time close to the current carrying center column than in a conventional tokamak (right in red) from [1]. Since the toroidal magnetic field drops off inversely with radius, this means that a given center column current gives a bigger field.
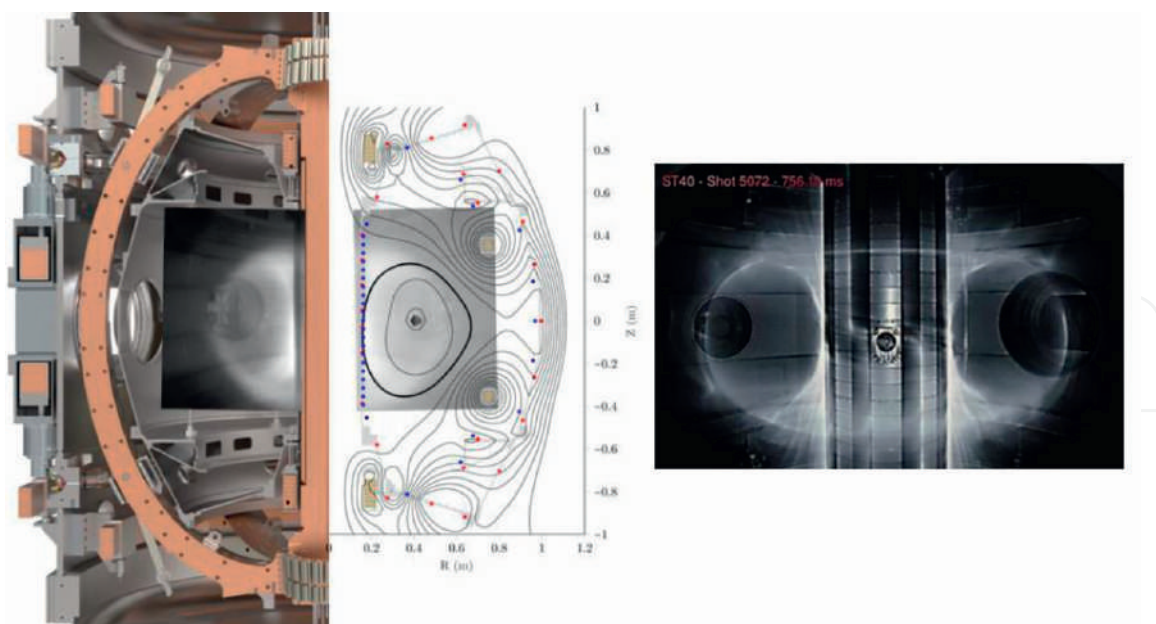
Figure 5.
The ST40 tokamak in May 2019 when the milestone plasma temperature of $15x10^6$ K was achieved. On the left is the engineering drawing along with the reconstruction of the plasma and optical image of the plasma.

its founders included START pioneers Alan Sykes and Mikhail Gryaznevich [14]. Its aim was to exploit the twin technologies of spherical tokamaks and high-temperature superconductors. The ST40 design team was chaired by Alan Sykes in 2014. Engineer and draftsman John Ross rapidly iterated designs with pencil and drawing board which hardly changed when the design moved to computer-aided design. **Figure 5** shows the design as of May 2019 when temperatures of $15x10^6$ K were first achieved.

Rapid development followed and ST40 moved to larger premises with space for a neutron shield and neutral beam injection to heat the plasma to the next milestone temperature of $100x10^6$ K which was successfully achieved in February 2022. In designing the next generation of spherical tokamaks, HPC facilities will be important particularly in solving the gyro-kinetics used to predict the plasma turbulence and plasma confinement time.

4. High-temperature superconductors

Bednorz and Müller discovered high-temperature superconductors (HTSs) back in 1986 [15]. The theory remains uncertain. The important fact is that by 2010 it was possible to buy kilometer lengths of HTS tape just 0.1 mm thick and 12 mm wide. Under the optimized manufacturing conditions, now readily achieved by commercial suppliers, $YBa_2Cu_3O_7$ (YBCO) has a superconducting critical temperature of ~90 K. State-of-the-art commercial tapes are now exhibiting engineering critical current densities >1000 A/mm^2 at 20 K and 20 Tesla field applied perpendicular to the tape which is the lowest performance configuration [16].

In 2015, Tokamak Energy demonstrated a simple 25 cm radius HTS tokamak operating continuously for 29 hours under a live demonstration during the Royal Society Summer Exhibition as illustrated in **Figure 6**.

The more difficult task was to create the HTS coils needed for an operational tokamak. A key problem is quench protection when any defect or heating anomaly
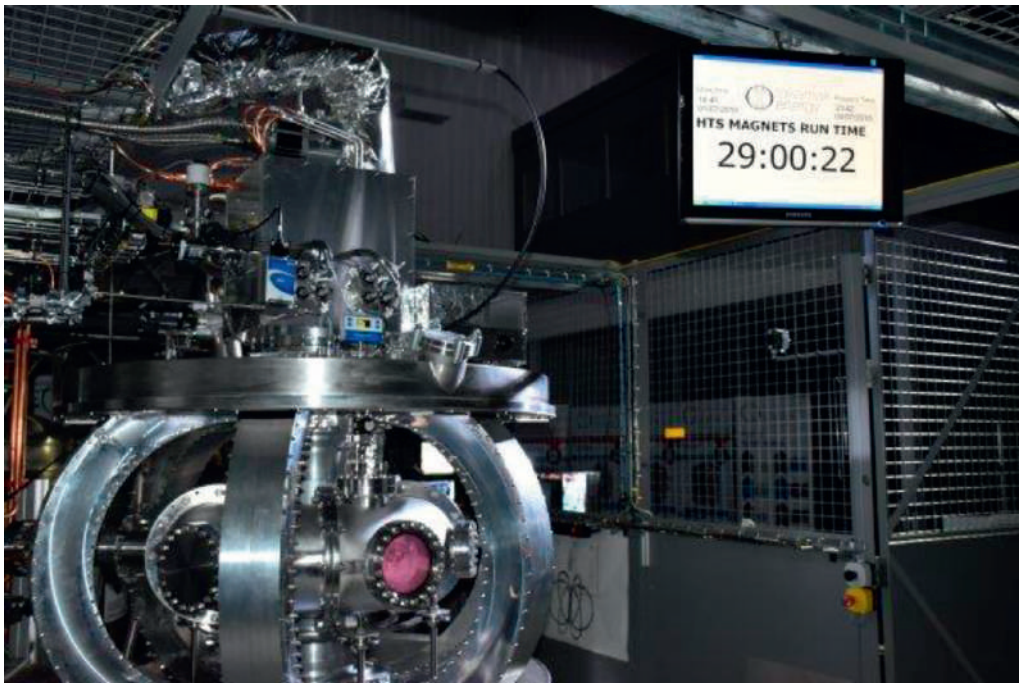
Figure 6.
The high-temperature superconducting tokamak ST25HTS in operation after for 29 hours.

can create a local temperature rise above the transition temperature. With an insulated conductor, the current has nowhere to go and so it heats up quickly. This can spread to nearby superconductors and so the magnet quenches and could be destroyed. The problem can be avoided by removing any insulation between the tapes. The current from any localized normal region of tape can then spread over to neighboring tapes and any
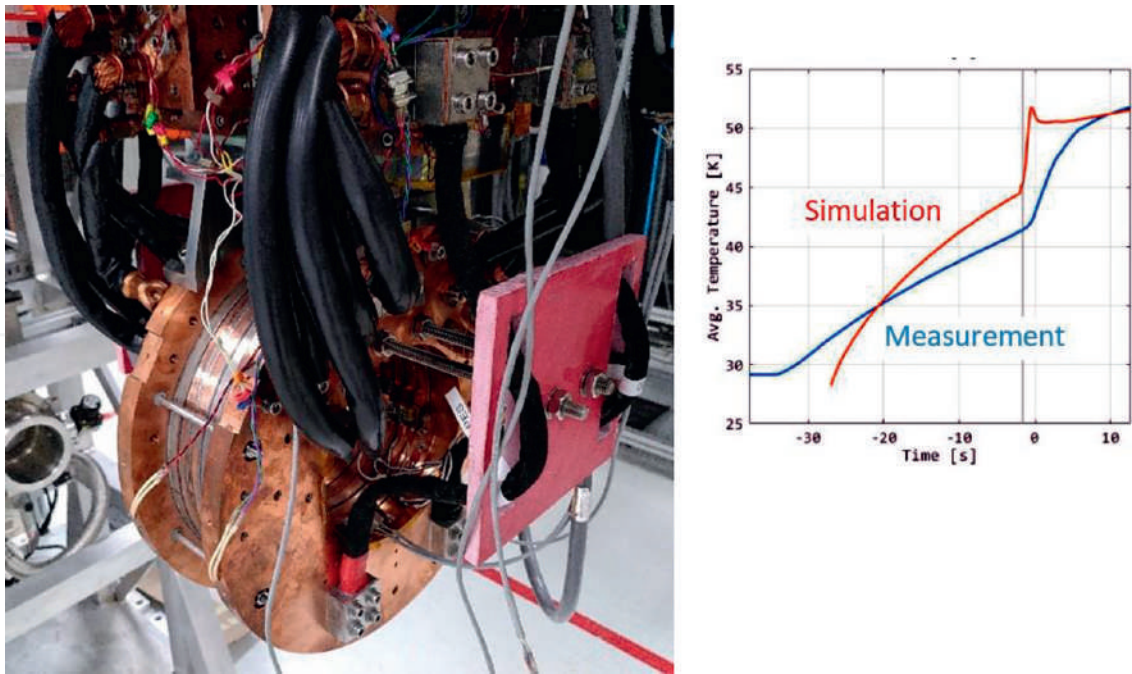

Figure 7.
The DEMO2 magnet constructed at Tokamak Energy [17]. The coil has a bore of 300 mm and contains six modular "pancake" coils wound with 738-m of 12-mm-wide tapes with variable inter-turn resistance between tapes and reached 10 Tesla. Inset is shown the RACOON code predictions of the coil temperature compared with the measurements during a quench at the vertical line position.

quench is avoided, but then the time constant for energizing the coil becomes impractically long. In research in the David Hawksworth HTS Magnet Laboratory at Tokamak Energy, a middle way of partial insulation has been developed with a precise inter-turn resistance between each tape layer to allow current transfer but avoid the time-constant problems. **Figure 7** shows "Demo2", a stack of six REBCO non-insulated pancakes with a diameter of 300 mm. Cooled to 20 K it is able to take a current of 3000 A and produce a peak field of over 10 Tesla. The magnet proved difficult to quench. It could be quenched by turning off the current, but the stored energy was dissipated within the magnet in the inter-turn resistance, and there was no system degradation [18].

Under construction at Tokamak Energy is a demonstration tokamak "Demo4" designed to operate at fields in the region of 20 Tesla with a full set of partially insulated HTS toroidal field coils.

5. Shield design explored using "tally tagging"

Figure 8 illustrates a well-known challenge of spherical tokamaks. For a given central HTS core radius R_{core}, (blue) and necessary vacuum *gap* (white) between the plasma (yellow) and the outer shield surface (brown), the available shield thickness drops rapidly with aspect ratio A. The HTS coils need to be actively cooled to around 20 K to remove the heat deposited from the incoming neutron and gamma irradiation. Also, the performance of the HTS material can be degraded by radiation.

A related dependence was shown by the open purple squares in **Figure 1** as a function of major radius for constant aspect ratio A = 1.8. **Figure 1** illustrates the balance that tokamak design must take between the HTS design constraints limiting the fields possible with a given core radius, the physics constraints of fusion power, wall heat load, the neutronics constraints of heat deposition into the HTS core, radiation damage limitation, and limiting the engineering stresses to acceptable levels. Most of these improve with larger major radius, but not all. The stored energy of the plasma increases as the cube of the size, but the surface area as the square, so that the energy
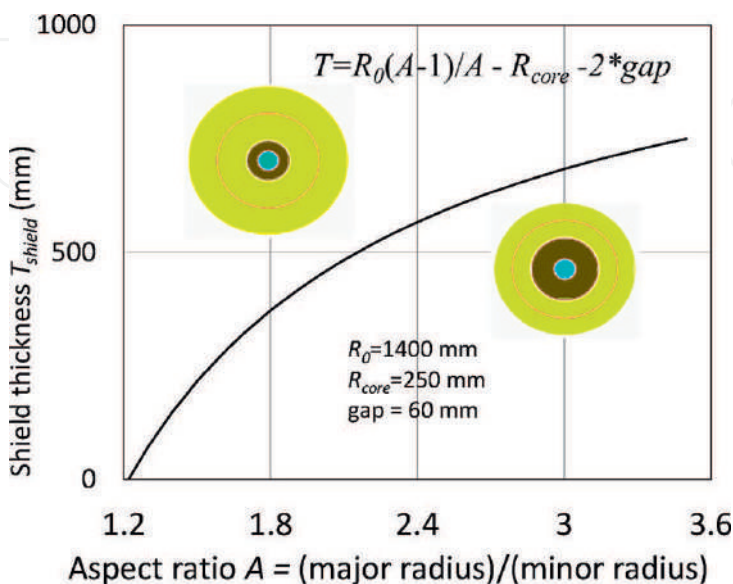

Figure 8.
The increase of shield thickness T with aspect ratio A for tokamaks of fixed major radius R_0 = 1400 mm (red line) and fixed HTS core radius R_{core} = 250 mm (blue).

per surface area increases with size [19]. This makes plasma disruptions, where some instability makes the plasma touch the wall and release its energy, a serious problem with large tokamaks and less serious with more compact tokamaks.

The main disadvantages of large size are cost and construction time, which did not appear in **Figure 1**. In practice, deciding the optimal size of a spherical tokamak power plant will be an optimization including these as well as outputs from plasma physics, HTS core construction, neutronics calculations, heat flow calculations, and structural engineering constraints.

The fusion power plants envisaged to use the D-T reaction when a deuterium and tritium ions collide to produce an alpha particle and a neutron $^2D + {}^3T = {}^4He + n + 17.6$ MeV. The helium alphas, being charged, tend to stay within the plasma and sustain its temperature. The neutrons, with 14.1 MeV energy, interact little with the plasma and escape to the inner and outer shields where their energy can be used to generate electricity and also to replenish the tritium ions by reactions with lithium in "blanket" layers within the shields. There are fewer size limitations to the outer shield, so this discussion will center on the optimization of the inner shield.

14.1 MeV neutrons are not easy to shield. They can be slowed down by multiple elastic collisions, moderation, or more quickly by inelastic (e.g. n, gamma) collisions. The moderation method is only practical for hydrogen moderators as the average value of the decrease in the natural logarithm of the neutron energy per collision is unity for natural hydrogen, but only 0.158 for carbon. The shield studies made for the Costley system code [3] results of **Figure 1** supposed a layered shield with thick layers of cemented tungsten carbide and thinner layers of water. The fast neutron flux through such a shield is shown in **Figure 9** taken from [20]. The half-attenuation
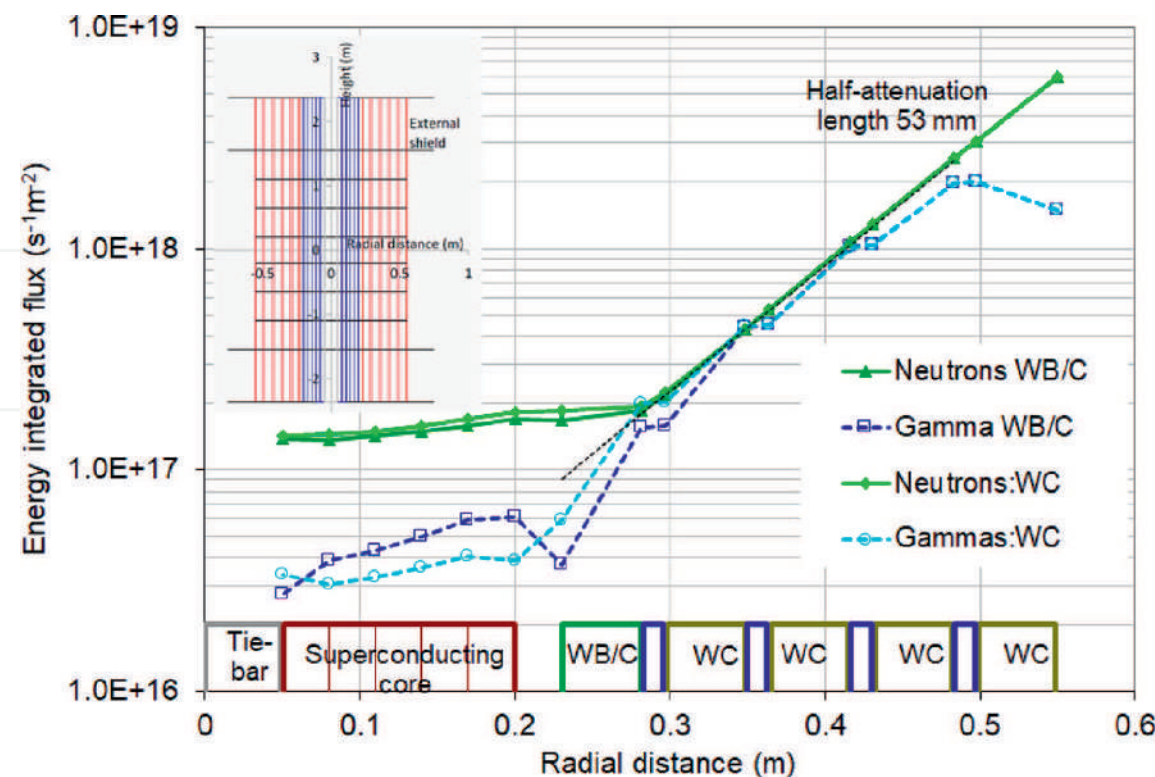

Figure 9.
The attenuation of fast neutrons (E > 0.1 MeV) though a layered shield of tungsten carbide (including with a tungsten boride inner layer) with intervening water channels for coolant and neutron moderation. The inset shows a vertical section [20].
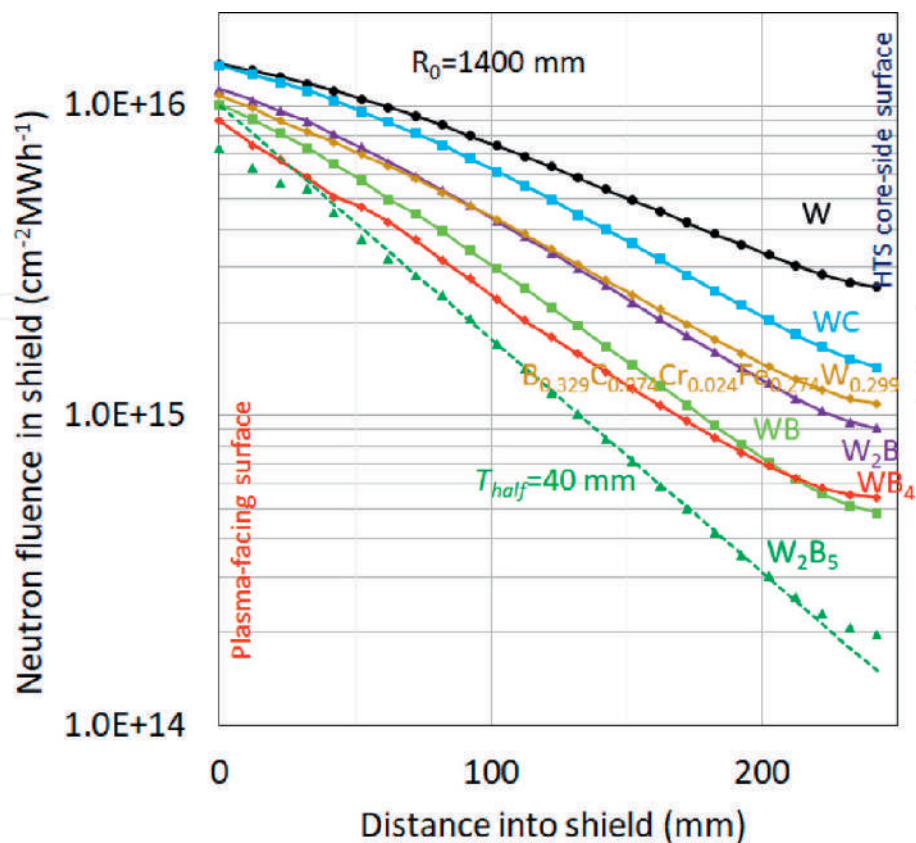
Figure 10.
The attenuation of neutrons though monolithic shields at 1400 mm major radii of boron carbides of varying composition, including a cemented borocarbide, pure tungsten, and tungsten carbide.

shield distance is 53 mm. This relatively poor attenuation is possibly because of the relatively high atomic fractions of carbon and oxygen which give little attenuation to either neutrons or gammas.

Water coolant is now seen to have serious problems in a fusion power plant. The activation of ^{16}O to ^{16}N which decays with a 7.1-s half-life is one issue, and another is the desire for heat production at higher temperatures where the water vapor pressure becomes serious. Helium gas cooling has none of these problems.

Monolithic shields with varying fractions of tungsten and boron were examined [21, 22] and shown to give half-attenuation coefficients as low as 40 mm as seen in **Figure 10**. The neutron cross sections of tungsten and boron are shown as a function of energy in **Figure 11**. Tungsten is a key element as its neutron cross section has significant inelastic neutron (n, 2n) and (n, n' gamma) reactions around the 1 to 10 MeV energies which reduce the 14.1 MeV neutrons to around 0.1 MeV energy. The ^{10}B isotope has an absorption cross section which rises inversely with neutron velocity giving a highly significant absorption below 0.1 MeV, not far above the energies where they are captured by ^{10}B which makes up around 20% of natural boron. The principal reactions occurring in a tungsten boride shield are illustrated in **Figure 12**. Let us consider each of the numbered processes.

Elastic scattering (i) of neutrons. Tungsten makes a good reflector as its cross section of ~3 barns of elastic cross section per atom at 14 MeV and its high mass compared to a neutron ensures little recoil energy. Most neutrons are not reflected but continue forward with slightly reduced energy. Moderation (ii) occurs when incident neutrons collide with lighter atoms, like boron. The collisions exchange, or moderate, the neutron energy, therby reducing the transmitted power. The best moderator is
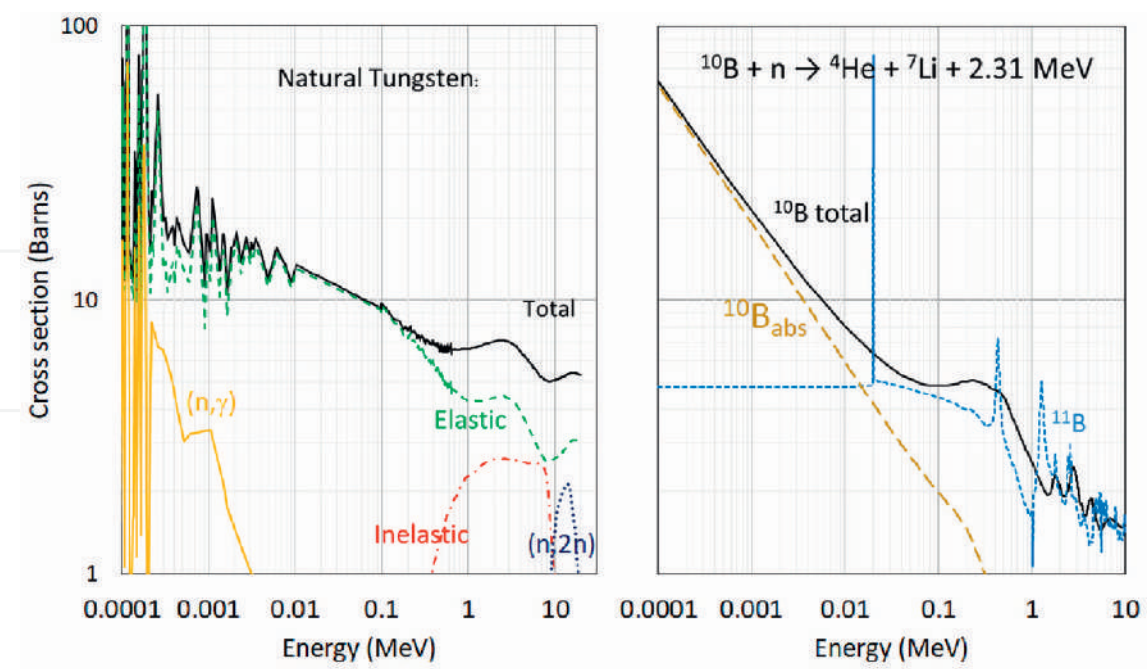
Figure 11.
The neutron cross sections for tungsten (left) and for boron (right). For tungsten, the total (black), elastic (green, dashed), inelastic (red, dash-dot), (n,2n) (blue, dotted), and (n, gamma) (yellow) cross sections are shown. For boron, the minority (20%) ^{10}B isotope (black) and the majority ^{11}B isotope cross section (blue dashed) are shown. Below 10 keV, the ^{10}B cross section follows an inverse velocity increase with decreasing neutron energy as show in the curve labeled $^{10}B_{abs}$. The cross sections are from the Brookhaven National Nuclear Data Centre [23].
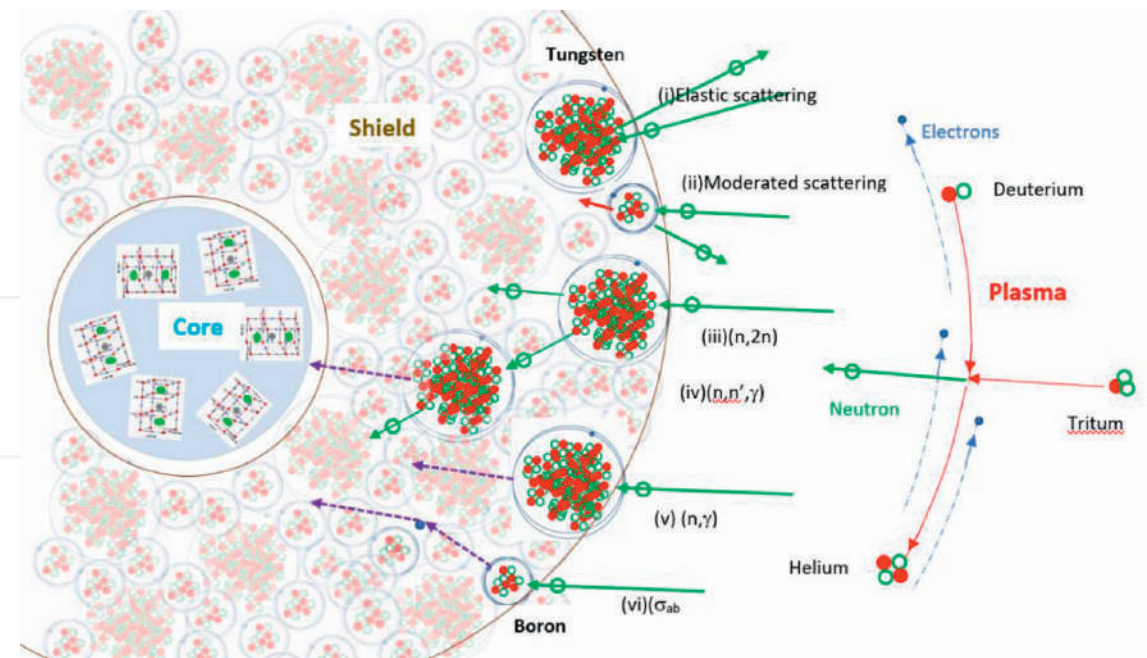

Figure 12.
Some of the processes involved in a tungsten boride shield protecting a high-temperature superconducting core from fusion neutrons generated by a plasma. Tungsten atoms are large, while boron atoms are small. Protons are red, neutrons green, electrons blue, and gammas violet. Fusion is fueled continuously by injecting tritium ions usually by pellet injection. These hit deuterium ions to produce helium ions and fast neutrons. The six scattering processes indicated are discussed in the text.

hydrogen since its mass is almost the same as the neutron and the maximum energy is lost on collision. Inelastic (n,2n) (iii) reactions produce a different isotope of the same element. A typical reaction would be ^{183}W + n = ^{182}W + 2n + γ, which is highly beneficial transforming each high energy neutron into two lower-energy neutrons of a few MeV which are easier to shield.

Inelastic (n, n' gamma) neutron scattering (iv) means that the incident neutron forms a new compound nucleus which quickly decays to release the neutron with an appreciably lower energy and with the emission of the excess energy in the form of a gamma. These gammas must then be shielded. (n, gamma) capture (v) is common at lower neutron energies. The neutron is absorbed to form a tungsten isotope with one higher atomic weight with the emission of gammas of significant energy (vi). The lower-energy neutrons produced by moderation or inelastic scattering become increasingly likely to be absorbed by isotopes such as ^{10}B with a high neutron absorption cross section. Gammas are shielded by scattering from electrons in the shield atoms and thus need high atomic number (number of electrons per atom) and high number density (atoms/m^3). Tungsten is a comparatively good element for a gamma shield, while boron is not.

More detailed information on the shield scattering process may be found by using the "tally tagging" feature of the MCNP code [24]. Fluence or energy deposition tallies generally total up all particles from all sources, reactions, atoms, and isotopes. Using tally tagging, the results can be broken down into any chosen set of these options. In order to limit the output file length, it is usually best to ask specific questions: "Did a neutron start in the plasma and survive all the way through the shield?" "Did a photon heating the HTS core get born in the core itself, or did it get born in the shield?" Each output contains a tally code of form CCCCCZZAAA.RRRRR where CCCCC optionally represents the origin tally cell number, ZZ the atom number, AAA the isotope number, and RRRRR the reaction type.

Another important refinement in fluence tallies is to separate them according to the angle the particle path makes with the normal to the tally surface. In the following examples, the angles were divided into six ranges 0° to 30°, 30° to 60°, 60° to 90°, 90° to 120°, 120° to 150°, and 150° to 180°. These subtend different solid angles, so these need to be corrected to give fluences per steradian.

Some results answering the question of where the neutrons originate from are given in **Figure 13** which shows the fluences at angles <30^0 to the shield layers. The tally tagging distinguishes the tally volumes where each neutron originated. The red triangles show those neutrons originating in the plasma, although some elastic moderation will have occurred. The direct neutron energy spectrum at 100 mm into the shield shown inset in red at the bottom left of **Figure 13** shows that this is a minor effect with elastic moderation caused by the tungsten and boron atoms giving the rapid half-attenuations of 0.24 and 0.8 MeV, respectively. The corresponding indirect neutron spectrum shown inset in blue at the bottom left of **Figure 13** is from the tungsten (n, gamma) and (n, n' gamma) reactions and is very broad and centered around 0.2 MeV. The corresponding gamma rays are seen to have a less broad distribution with some peaks centered around 1 MeV. The tally tagging feature can also identify the origin of the indirect fluence in more detail. It shows that most of the indirect neutrons come back from tungsten atoms further into the shield. The indirect gammas came equally from tungsten and boron atoms within a few centimeters of the fluence position.
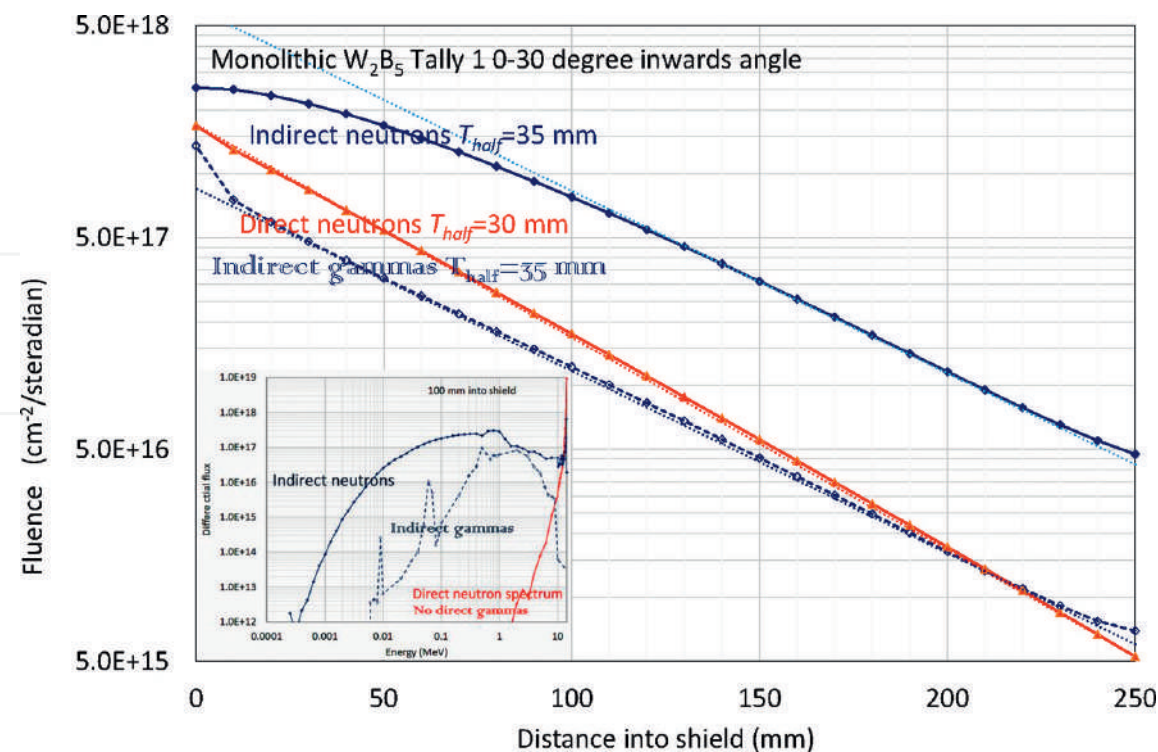
Figure 13.
The attenuation of fluence through a W$_2$B$_5$ shield for neutrons created in the plasma (red direct) and neutrons and gammas created inelastically in the shield (blue). There are no direct gammas. Inset are shown the energy spectrum of the direct neutrons (red upper right) and the indirect neutrons and gammas (blue lower left).

An illustration of the energy dependence of the neutrons as they pass through a W$_2$B$_5$ shield is given in **Figure 14**. Neutrons incident on the shield make up a "pool" of 14 MeV neutrons which extends with decreasing fluence through the shield. At any shield position, a fraction "falls down the waterfall" to energies around 0.2 MeV. At the base of the "waterfall," the neutrons lose further energy by moderation down a gently sloping riverbed. In W$_2$B$_5$ as their energy reaches 0.001 MeV energies, they soon become almost completely absorbed by ^{10}B as in a porous sandy riverbed.

A simple model of the W$_2$B$_5$ shield is that the fluence of direct neutrons of around 14 MeV energy exists across the shield with around 30-mm half-attenuation distance. Inelastic (n, n' gamma) reactions lower the neutron energy to around 0.2 MeV, but the resulting gamma rays are attenuated in only a few centimeters. Further moderation reduces the neutron energy to the level where they are absorbed by ^{10}B. In a pure tungsten shield, the waterfall from 14 to 0.2 MeV is again present, but there is no ^{10}B absorption, so once again low-energy neutrons build up steadily through the shield leading to an ever-increasing pool of low-energy neutrons.

W$_2$B$_5$ is exceptional in that its ^{10}B absorption removes most neutrons within a localized region of the shield so that the energy spectrum is almost identical through the bulk of the shield.

The HTS core of a tokamak power plant needs to be kept at temperatures of order 20 K. The heat deposition into the core determines the cryogenic power necessary to maintain this low temperature. The power deposition is also a determinant of the HTS radiation damage. The neutron and gamma power depositions into the core have been evaluated previously, but here the tally tagging option of MCNP has been used to investigate the processes by which this heat arrives at the HTS material. **Figure 15** shows the neutron and gamma contributions to the heat deposition into a fully cooled
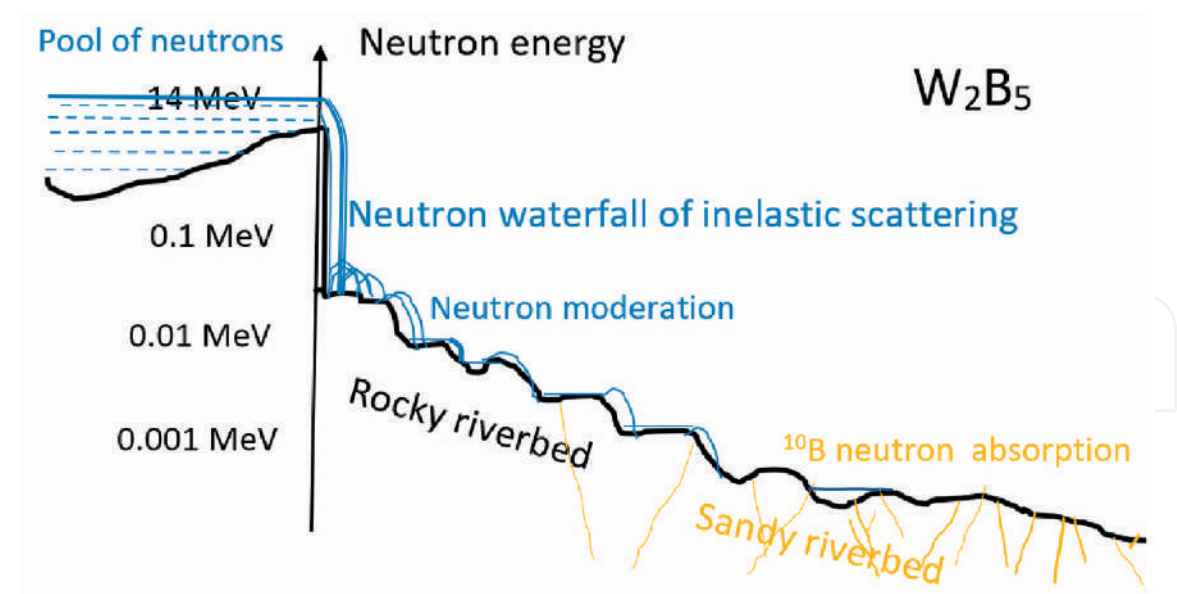
Figure 14.
An illustration of the energy dependence of the neutrons passing through A W_2B_5 shield. Neutrons incident on the shield come from a "pool" at 14 MeV. This pool decreases in width through the shield as (n, n' gamma) inelastic reactions produces an energy "waterfall" reducing the neutron energy to around 0.2 MeV. At the bottom of the waterfall, moderation reduces the energy gradually (the rocky riverbed) until energies are almost wholly absorbed by ^{10}B (the sandy riverbed). The gammas produced by the inelastic scattering are absorbed in a few centimeters so that the diagram is valid throughout the bulk of the shield.
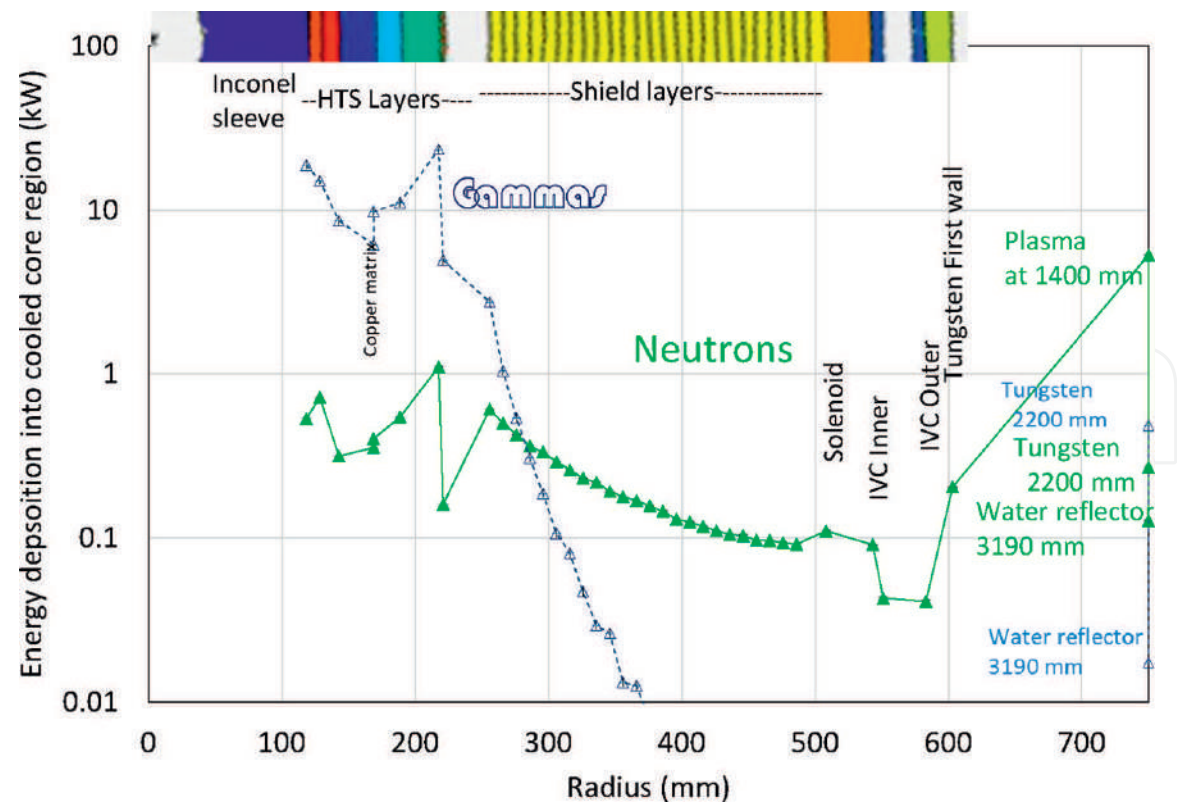

Figure 15.
The origins of the heat deposition into the cooled core of the tokamak including the inconel sleeve, HTS coils, copper cladding, and stainless inner vacuum vessel and shield layers as shown inset at the top of the figure. The major gamma component arises from the core components with the shield component decreasing rapidly. The neutron component is dominated by the direct contribution from the plasma itself and the outer wall reflector.

core region which includes the central inconel sleeve, the copper cladding surrounding the HTS, and the 316 L stainless inner vacuum vessel. It was established that the total HTS gamma heating was some four times larger than the total neutron heating [21]. It is clear from the figure that the largest gamma contributions arise around the HTS tape layers and the surrounding materials, copper cladding, and the inner vacuum vessel. Contributions from the shield layers are around an order of magnitude less and fall of rapidly into the shield. Direct gammas from the plasma and outer wall are very low.

In contrast, the major contribution to the neutron heat deposition is from the plasma itself out at 1400 mm radius (way off the scale of the figure!). As described earlier at each shield layer, some of these neutrons are inelastically scattered to give much lower-energy neutrons which are soon absorbed, and gammas which are rapidly attenuated within the shield. Some 14 MeV neutrons do persist all through the shield and provide the bulk of the heat deposition. Neutrons inelastically scattered by the HTS core volume, and the shield give contributions which are significant but around an order of magnitude lower.

Again, the tally tagging feature of MCNP can be used to explore in more detail the elements, isotopes, and reactions which give rise to the heat deposition. **Figure 16** shows the neutron (left) and gamma (right) contributions to the heat deposition in the actual HTS materials within the core (excluding heat into the cold inconel center rod and the 316 L stainless steel inner pressure vessel included in **Figure 16**). The figure shows that the direct neutron energy deposition is still dominated by the "direct" contributions, principally from neutrons generated within the plasma itself, but also from neutrons scattered from the tungsten and water reflector layers beyond the plasma. The next highest contribution is around 20 times lower and come from n (n', gamma) interactions in the HTS material itself. In contrast, the principal gamma heating arises from (n, gamma), (n, n' gamma), (n,2n), and fluorescence reactions.
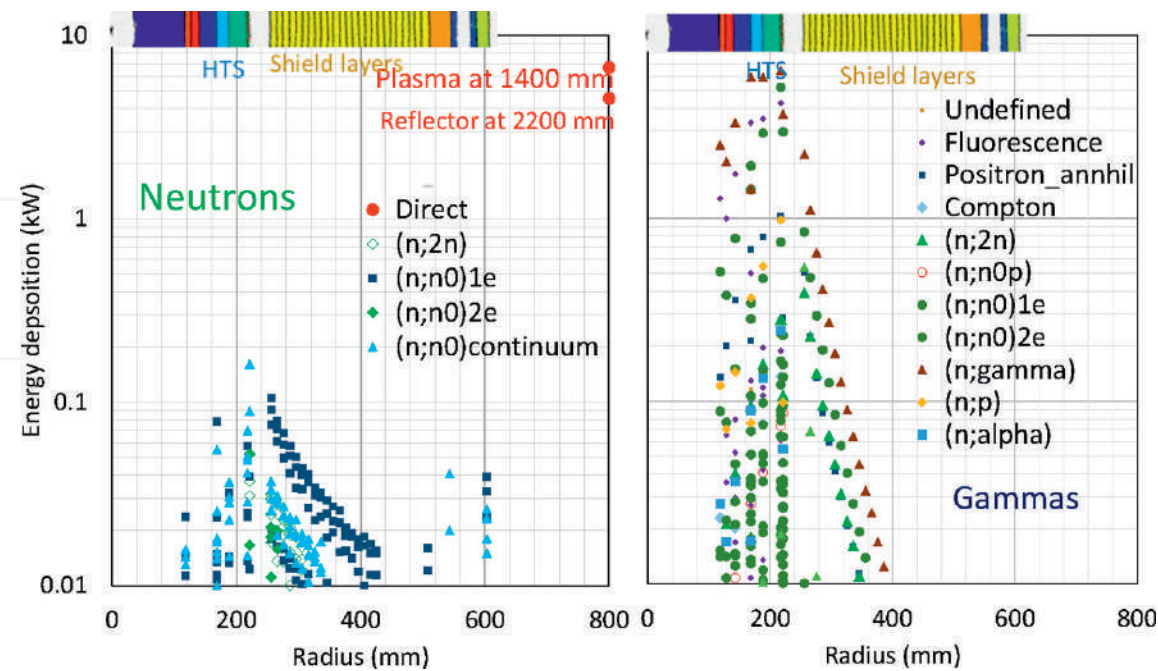

Figure 16.
The originating positions and reactions responsible for the neutron energy deposition into the HTS core volumes of a spherical tokamak power plant. The colored upper band and labels record the various tally volumes contributing to the energy deposition. The different symbols record the reaction method. "Direct" refers to neutrons originating in the plasma core itself, most from the plasma, some from the outer reflector, both off the scale of the neutron graph.

These tend to be largest close to and fall off quite rapidly into the shield layers. Direct gamma heating is negligible.

The effects of these results on radiation damage are clear. Fast neutron damage will arise from the 14-MeV neutron fluence component which penetrates the shield. Gamma damage in contrast can be identified as coming from (n, n' gamma) reactions in ^{63}Cu from the heat-sink material surrounding the HTS tapes and from ^{56}Fe and ^{58}Ni in the Hastalloy of the HTS tapes. (n, gamma) reactions from ^{184}W and ^{182}W in the shield are significant but reduce rapidly into the shield.

6. Conclusions

Spherical tokamaks with HTS magnets are one of few options for safe, abundant energy on a small footprint. This chapter addresses a key issue: finding a material that can shield the HTS core while maintaining small major radius and low aspect ratio. It explores the operational performance of tungsten boride tokamak shields particularly using the tally tagging option of MCNP to detail the locations, atoms, and reactions contributing to neutron and gamma fluence and energy depositions. These studies have revealed that the W_2B_5 shield operation is dominated by the slightly moderated near 14 MeV neutrons produced in the plasma. At all positions well within the shield, this fluence of neutrons is attenuated by inelastic (n, n' gamma) reactions to produce lower-energy neutrons which can be absorbed by ^{10}B and gammas which are absorbed by tungsten in a few centimeters. Our HPC capability has been instrumental in our design process. It will be increasingly used in our quest for faster fusion.

Acknowledgements

Author details

Colin Windsor* and Gurdeep Kamal
Tokamak Energy Ltd., Milton Park, Oxon, UK

*Address all correspondence to: colin.windsor@tokamakenergy.co.uk

IntechOpen

References

[1] Windsor C. Can the development of fusion energy be accelerated? 2019. DOI: 10.1098/rsta.2017.0446

[2] Lawson J. Harwell report A.E.R.E GP/R 1807. 1955. Available from: https://www.euro-fusion.org/fileadmin/user_upload/Archive/wp-content/uploads/2012/10/dec05-aere-gpr 1807.pdf

[3] Costley AE, Hugill J, Buxton PF. On the power and size of tokamak fusion pilot plants and reactors. Nuclear Fusion. 2015;**55**:033001

[4] Costley AE. Towards a compact spherical tokamak fusion pilot plant. Philosophical Transactions of the Royal Society A. 2019;**377**:20170439. DOI: 10.1098/rsta.2017.0439

[5] Flyvbjerg B. What you should know about megaprojects and why: An overview. Project Management Journal. 2014;**45**(2):6-19,

[6] Sykes A, Turner MF, Patel S. Proceedings of the 11th European Conf. on Controlled Fusion and Plasma Physics. Vol. 2. Aachen, Germany; 1983. p. 363

[7] Peng Y-KM, Strickler DJ. Features of spherical torus plasmas. Nuclear Fusion. 1986;**26**:769

[8] Gryaznevich M et al. Achievement of record β in the START spherical tokamak. Physics Review Letters. 1998;**80**:3973-3975

[9] Bickerton RJ, Connor JW, Taylor JB. Diffusion driven plasma currents and bootstrap tokamak. Nature Physical Science. 1971;**229**:110

[10] Zarnstorff MC et al. Bootstrap current in TFTR. Physical Review Letters. 1968;**60**:1306

[11] Stork D. The upgrade to the Mega Amp Spherical Tokamak, International Atomic Energy Agency, Vienna (Austria); 637 p; Oct 2010; p. 473; FEC 2010: 23. IAEA Fusion Energy Conference; Daejeon (Korea, Republic of); 11-16 Oct 2010; ICC--P5-06

[12] National Spherical Torus Upgrade, Princeton plasma physics laboratory, USA. 2022. Available from: https://www.pppl.gov/research/nstx-u

[13] Globus M2 tokamak, Ioffe Institute, St. Petersberg, Russia. 2020. Available from: https://www.nature.com/articles/d42473-021-00131-5

[14] Tokamak Energy, Milton Park, Didcot, UK. 2022. Available from: https://www.tokamakenergy.co.uk/technology/st40/

[15] Bednorz JG, Müller KAZ. Possible high Tc superconductivity in the Ba-La-Cu-O system. Zeitschrift für Physik B Condensed Matter. 1986;**64**:189-193. DOI: 10.1007/BF01303701

[16] Molodyk A et al. Development and large volume production of extremely high current density YBa2Cu3O7 superconducting wires for fusion. Scientific Reports. 2021;**11**:11. DOI: 10.1038/s41598-021-81559-z

[17] Nuclear Engineering International News 23/09/2021 Tokamak Energy demonstrates new magnet technology for fusion power

[18] Tokamak Energy. Tests patented partial insulation technology. Superconductor Week. 2021;**35**(9)

[19] Hender JC, Wesley C, Bialek J, et al. Chapter 3: MHD stability, operational limits and disruptions.

Nuclear Fusion. 2007;**47**(6):S128.
DOI: 10.1088/0029-5515/47/6/S03

[20] Windsor CG, Morgan JG. Neutron
and gamma flux distributions and their
implications for radiation damage in
the shielded superconducting core of
a fusion power plant. Nuclear Fusion.
2017;**57**:116032. DOI: 10.1088/1741-4326/
aa7e3e

[21] Windsor CG, Astbury JO,
Davidson JJ, McFadzean CJR, Morgan JG,
Wilson C, et al. Tungsten boride shields
in a spherical tokamak fusion power
plant. Nuclear Fusion. 2021;**61**:086018.
DOI: 10.1088/1741-4326/ac09ce

[22] Windsor CG, Astbury JO, Morgan JG,
Wilson C, Humphry-Baker SA.
Activation and transmutation of tungsten
boride shields in a spherical tokamak.
Nuclear Fusion. 2022;**62**:036009.
DOI: 10.1088/1741-4326/ac4866

[23] Brookhaven National Nuclear Data
Center, Evaluated nuclear data file

[24] McKinney GW. Tally tagging feature
in MCNPX 2.7.A, Los Alamos report
999LA-UR-08-06930. 2008. Available
from: https: //mcnp. lanl.gov/pdf_files/
la-ur-08-6930.pdf